

Code calibration for coupled, effective stress FEM-assessments of the primary flood defenses at Eemshaven-Delfzijl

Final report

28 February 2017

Authors:

Ruben Jongejan	(RMC)
Jacob Chacko	(Fugro)
Amalia Giannakou	(Fugro)
Vasileios Drosos	(Fugro)
Panagiota Tasiopoulou	(Fugro)

Table of contents

1	Introduction	1
2	Flood protection standards and code calibration	2
3	Proposed code calibration procedure and action items	5
4	Action item 1: characterize uncertainties	7
4.1	Spectral acceleration (T=0.85s) at Top of Bedrock NSUB (SA_{NSUB})	7
4.2	Spectral acceleration (T=0.85s) at Base of 2D Numerical Models (SA_{model_base})	9
4.3	$CRR_{M=7.5}$ in sand deposits	11
4.4	$CRR_{M=5.0}$ in laminated deposits	11
4.5	Uncertainty related to residual strength ($\epsilon_{Su/p}$)	12
4.6	Model Uncertainty (ϵ_M)	13
4.7	Uncertainties related to motion characteristics	14
4.8	Overview of stochastic variables	15
5	Action item 2: FORM analyses using the simplified liquefaction procedure	17
5.1	Limit state function	17
5.2	Input of probabilistic analyses	18
5.3	Results of FORM-analyses	18
5.4	Discussion	19
6	Action item 3: FORM analyses using the 2D effective stress model	20
6.1	Limit state function	20
6.2	Input of probabilistic analyses	20
6.3	Results of FORM-analyses	21
6.4	Discussion	23
7	Action item 4: Revisiting the length effect	24
7.1	Introduction: cross-sectional and system-level reliability assessments	24
7.2	The length effect and cross-sectional target reliabilities	27
7.3	Characterizing the length effect: the parameter a	29
7.4	Characterizing the length effect: the parameter b	29
7.4.1	Theory	29
7.4.2	Sensitivity analyses	30
7.4.3	Comparison with earthquake damage observations to embankments	32
7.4.4	Proposed b-value	35
7.5	Updated cross-sectional target reliabilities	36
8	Action item 5: Synthesis	37
8.1	From calculated FORM-influence coefficients and target reliabilities to design values	37
8.2	Uncertainty related to motions	39
8.3	Uncertainty related to stratigraphy	39
8.4	Sea level (load combination)	39
	References	40

Appendix A	First Order Reliability Method (FORM)	42
Appendix B	Design point values	45
Appendix C	Uncertainty in site response analysis up to the model base.....	46
Appendix D	Cyclic Resistance of Laminated Deposits	50
Appendix E	Residual strength	66
Appendix F	Model uncertainty.....	68
Appendix G	Volume effects	71
Appendix H	Uncertainty related to motions	79
Appendix I	Results of FORM-analyses for the 2D finite elements model	84
Appendix J	Sensitivity analyses on design sea water level	90

1 Introduction

This document concerns the derivation of design values for use with the assessment method developed by Fugro for the primary flood defenses at Eemshaven-Delfzijl (Fugro 2016a; Fugro 2016b). This method involves:

1. A fully coupled, dynamic, effective stress co-seismic analysis, in which displacements are calculated with dynamic FEM-calculations while excess pore pressures are being generated.
2. A static post-seismic analysis, in which residual displacements are calculated with the excess pore pressures and deformations at the end of shaking as a starting point.

This document presents the results of a code calibration study for the abovementioned numerical analyses. It also provides background information about the Dutch flood protection standards and code calibration studies in general. The code calibrated assessment procedure is summarized in chapter 8.

The code calibration assessment procedure has been developed for assessing the seismic stability of the Eemshaven-Delfzijl sea dikes. For other applications, such as for regional flood defenses, it is recommended to verify the applicability of the design values presented herein with probabilistic analyses.

2 Flood protection standards and code calibration

The Dutch flood protection standards are defined in terms of maximum allowable probabilities of flooding. The maximum allowable probabilities of flooding range from 1/100 per year to 1/100,000 per year. The Eemshaven-Delfzijl project covers parts of two different segments: segment 6-6 with a standard of 1/1,000 per year and segment 6-7 with a standard of 1/3,000 per year (Figure 1).



Figure 1. Overview of segments in the Flood Protection Act (in Dutch: Waterwet).

There are essentially two approaches for assessing whether a flood defense complies with a flood protection standard:

1. Probabilistic (using e.g. Monte Carlo, FORM)
2. Semi-probabilistic (design value or partial factor approach)

While the outcomes of probabilistic analyses can be compared directly to reliability requirements, most engineers are unfamiliar with probabilistic methods. Probabilistic analyses can also be prohibitively time consuming, which is the case for the model considered herein. A semi-probabilistic procedure is essentially an approximate procedure for evaluating whether a probability of flooding is smaller than required by law.

Probabilistic and semi-probabilistic safety assessments are closely related. Both rely on the same reliability requirements, the same limit state functions and the same probability distributions of stochastic variables. The only difference concerns the fact that a semi-probabilistic approach rests on a number of simplifications and approximations, giving it the appearance of a deterministic procedure.

In probabilistic safety assessments, analysts consider the probability that the ultimate limit state is exceeded, i.e. that load (S) exceeds resistance (R). The failure probability, $P(S > R)$, should not exceed some maximum allowable or target probability of failure (P_T).

In semi-probabilistic assessments, analysts consider the difference between the design values of load (S_d) and strength (R_d): S_d should not exceed R_d . Design values are representative values such as 5th or 95th quantile values or 1/10.000 yr⁻¹ water levels, factored with partial safety factors, see equations (1) and (2). Note that the

definitions from the Eurocode have been adopted here, similar terms may have different meanings in other codes.

$$S_d = S_{rep} \cdot \gamma_S \quad (1)$$

$$R_d = R_{rep} / \gamma_R \quad (2)$$

Where:

- S_d Design value of uncertain load variable
- R_d Design value of uncertain resistance variable
- γ_S, γ_R Partial factors

Design values, and hence (partial) safety factors, should be defined in such a manner that $S_d \leq R_d$ implies that the probability of failure meets the reliability requirement: $P(S > R) \leq P_T$. The relationship between probabilistic and semi-probability safety assessments is illustrated in Figure 2.

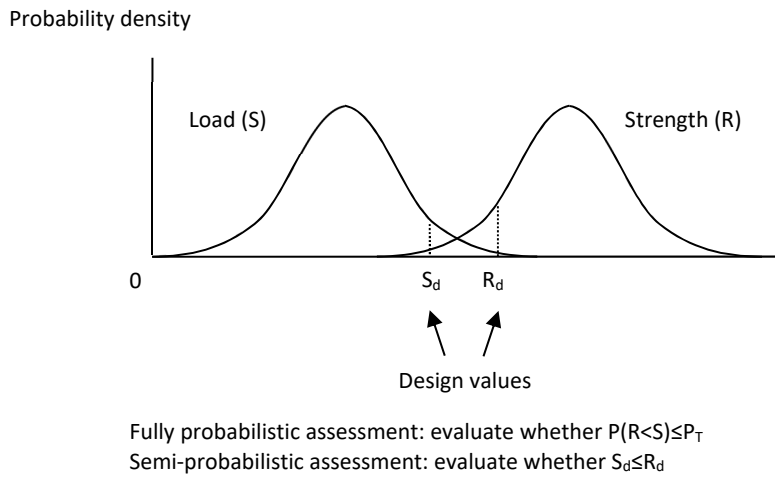


Figure 2. The probability density functions of load (S) and strength (R), and the design values of load and strength (S_d) and (R_d).

A close link between probabilistic and semi-probabilistic assessments can be achieved by equating the design values of the different stochastic variables to their design point values (see Figure 3 for a graphical representation):

$$X_d = F_X^{-1}(\Phi(-\alpha_X \cdot \beta_T)) \quad (3)$$

Where:

- $F_X^{-1}(\cdot)$ Inverse of the cumulative distribution function of stochastic variable X
- X_d Design value of stochastic variable X
- β_T Target reliability index, which equals $\Phi(1 - P_T)$
- α_X Influence coefficient for stochastic variable X

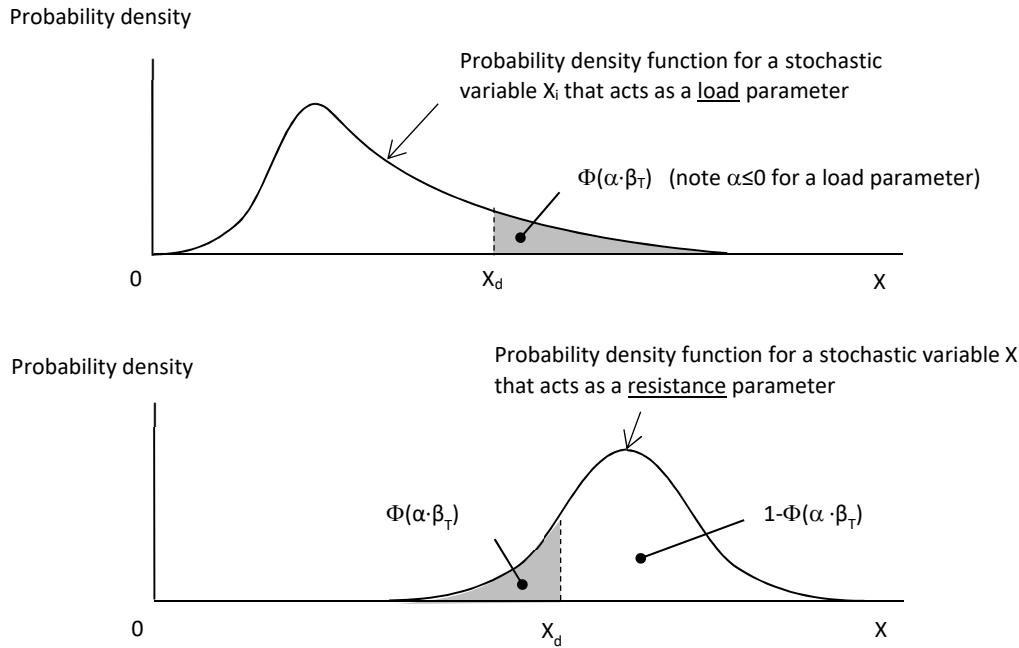


Figure 3. The design point values of stochastic load and resistance variables and their probabilities of exceedance.

For a normally distributed stochastic variable, equation (3) yields:

$$X_d = \mu_X - \alpha_X \cdot \beta_T \cdot \sigma_X \quad (4)$$

Where:

- μ_X Mean value of the normally distributed variable X
- σ_X Standard deviation of the normally distributed variable X

The above shows that a code calibration essentially revolves around:

1. the specification of appropriate target reliabilities and
2. the specification of appropriate influence coefficients.

NB1

In principle, there is no objection to extending the fully probabilistic PSHA to a fully probabilistic system-level reliability analysis. The reason for not doing so and opting for a semi-probabilistic approach is purely pragmatic.

NB2

The Dutch flood protection standards (2017 onwards) say nothing about the loads that primary flood defenses should be able to withstand. Without code calibration, appropriate design loads would remain unspecified. The same goes for resistance.

NB3

The terms “load” and “demand” are used as synonyms throughout this document. The same goes for “resistance” and “capacity”. While the terms “load” and “resistance” are commonly used in hydraulic engineering, the terms “demand” and “capacity” appear to be more common in earthquake engineering.

NB4

The fact that PSHAs are fully probabilistic and the fact that e.g. Boulanger & Idriss (2014) and Green et al. (2016) have characterized the uncertainties related to liquefaction triggering relationships by probability distributions shows that probabilistic concepts and techniques are already quite common in earthquake engineering. This has made it easier to relate earthquake models (for demand and capacity) to probabilistic standards.

3 Proposed code calibration procedure and action items

An overview of the steps taken to arrive at a calibrated semi-probabilistic assessment rule is given below.

Action item	Description	Objective
1	Characterize the uncertainties related to the input and output of the Fugro model (i.e. coupled, effective stress FEM)	<p>Define the input of subsequent analyses</p> <p>Give an early impression of the level of conservatism in previous analyses</p>
2	Derive (preliminary) estimates of design values from a probabilistic analysis using the simplified liquefaction procedure and the uncertainties specified by e.g. Green et al. (2016)	Get a feel for influence coefficients
3	FORM analysis using the Fugro model	Get a feel for influence coefficients
4	Revisit previous assumptions concerning the length effect	Define cross-sectional target reliabilities

5	Make an informed decision about design values	On the basis of the results of the abovementioned actions: decide on appropriate design values.	Establish design values on the basis of influence coefficients and target reliabilities (decision informed by results from action items above)
---	---	---	---

4 Action item 1: characterize uncertainties

The following stochastic variables were considered in the FORM-analyses with the FE-model:

1. The seismic demand at the base of the 2D numerical models ($SA_{\text{model_base}}$). The distribution of this stochastic variable rests on a convolution of the uncertainty related to the acceleration at the North Sea Upper Base and the uncertainty in the site response up to the base of the model.
2. The cyclic resistance ratio (CRR) of sand deposits
3. The cyclic resistance ratio of laminated deposits
4. The uncertainty related to residual strength ($\epsilon_{Su/\rho'}$)
5. Model uncertainty (ϵ_M)

Two other important sources of uncertainty are:

1. The uncertainty related to stratification in the top 30 meters.
2. The uncertainty related to the characteristics of spectrally matched motions.

Each probabilistic analyses has been carried out for a given stratigraphy and a given motion. The uncertainty related to stratification can be dealt with by carrying out sensitivity analyses and (if needed) by combining the results of the assessments for the different stratifications with their probabilities (see ENW 2012). The same applies to the uncertainty related to motions, see section 4.7.

The five stochastic variables mentioned above are believed to be the most important ones in a probabilistic analysis for a given stratigraphy (top 30m) and a given motion. The fact that all other variables have been treated as deterministic is conservative within the present context. This is because this leads to a (slight) overestimation of the relative importance of the uncertainty related to the abovementioned stochastic variables, leading to more conservative design values for these variables.

4.1 Spectral acceleration (T=0.85s) at Top of Bedrock NSUB (SA_{NSUB})

The spectral period of 0.85 s has been selected as being representative of seismic demand in the FORM analyses with the FE model FE since:

- a. it is near the fundamental period of the 1D soil column that extends from top of bedrock (at about - 350 m depth) to the ground surface; and
- b. it is near the fundamental period of the 2D numerical models.

The hazard curve of the spectral acceleration at the top of bedrock (NSUB) for a spectral period $T=0.85s$ provided by KNMI has been approximated with a lognormal distribution (Figure 4 and Figure 5). Since the hazard curves at Eemshaven and Delfzijl locations are different, different lognormal distributions are used to approximate the hazard curves at top of bedrock for these locations.

Care was taken so that the fitted lognormal distribution is closest to the target curve around the design point. FORM analyses results indicate that the exceedance probability of the design point value of $SA(0.85)$ is smaller than 1/1000 per year (i.e.: >1000 year return period). The difference of between the lognormal fit and the target curve at exceedance probabilities greater than 1/1000 per year (i.e. <1000 year return periods) does not influence results of the FORM-analysis.

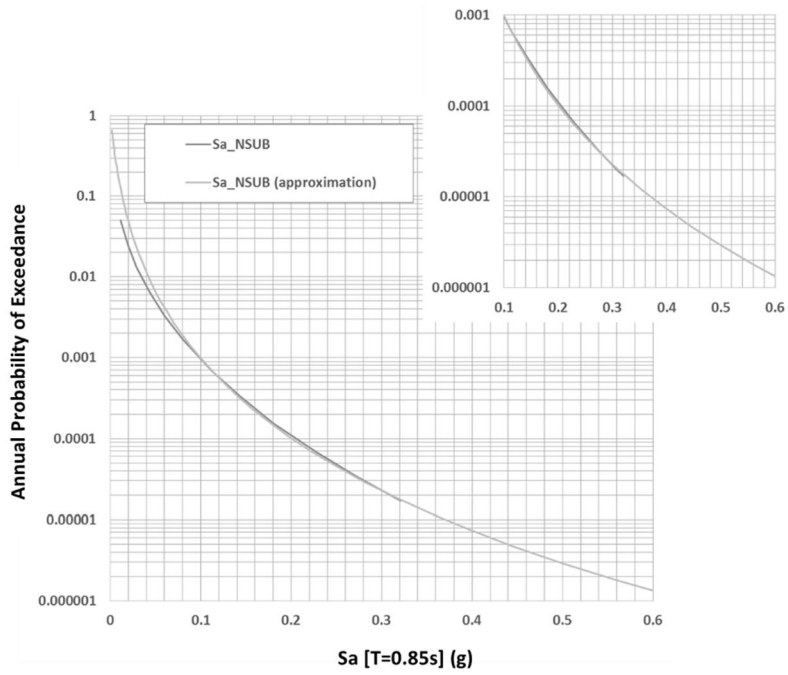


Figure 4. Spectral acceleration ($T=0.85s$) hazard curve at the top of bedrock at Eemshaven and approximation with a lognormal distribution [hazard curve provided by KNMI]. Lognormal distribution with $\mu_{ln(SA)} = -5.77$ and $\sigma_{ln(SA)} = 1.12$.

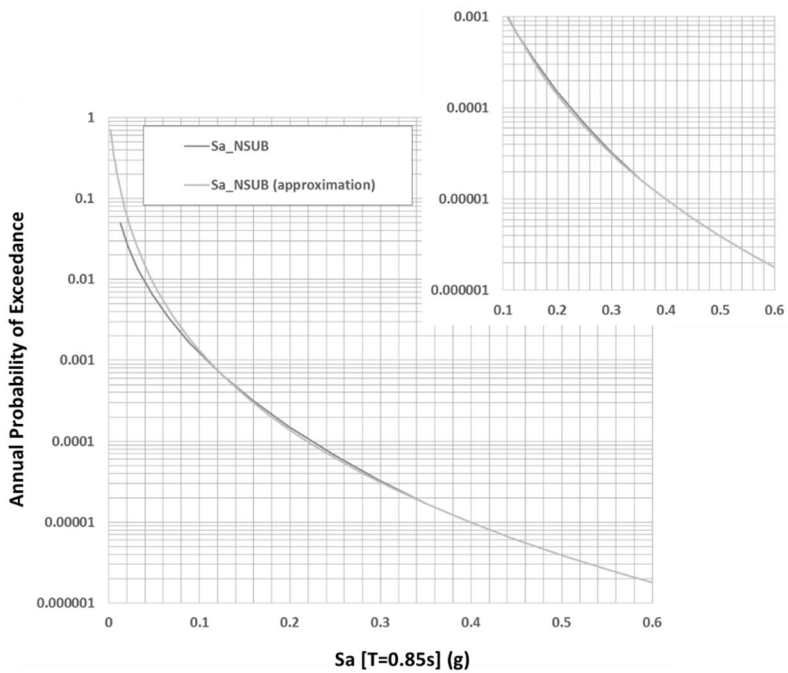


Figure 5. Spectral acceleration ($T=0.85s$) hazard curve at the top of bedrock at Delfzijl and approximation with a lognormal distribution [hazard curve provided by KNMI]. Lognormal distribution with $\mu_{ln(SA)} = -5.61$ and $\sigma_{ln(SA)} = 1.10$.

The mean and standard deviations of the lognormal distributions used to approximate the hazard curves at the top of bedrock are summarized in Table 1.

4.2 Spectral acceleration (T=0.85s) at Base of 2D Numerical Models ($SA_{\text{model_base}}$)

The hazard curve of the spectral acceleration at base of the numerical model for a spectral period $T=0.85\text{s}$ (i.e. NAP -30 m for Eemshaven and NAP-20m for Delfzijl, see Appendix C) is estimated following the procedure by Bazzurro and Cornell (2004) and Stewart et al. (2014) by a convolution of the hazard curve at top of bedrock (SA_{NSUB}) with the probability distribution of the site amplification factor described in Appendix C (Figure 6). Monte Carlo simulations were also performed for the convolution of the bedrock hazard curve and the site amplification probability distribution and similar results were obtained. The hazard curves of the spectral acceleration at the base of the numerical models ($SA_{\text{model_base}}$) for a spectral period $T=0.85\text{s}$ was approximated with a lognormal distribution (Figure 7 and Figure 8). The mean and standard deviations of the lognormal distributions used to approximate the hazard curves at the base of the numerical models are summarized in Table 1.

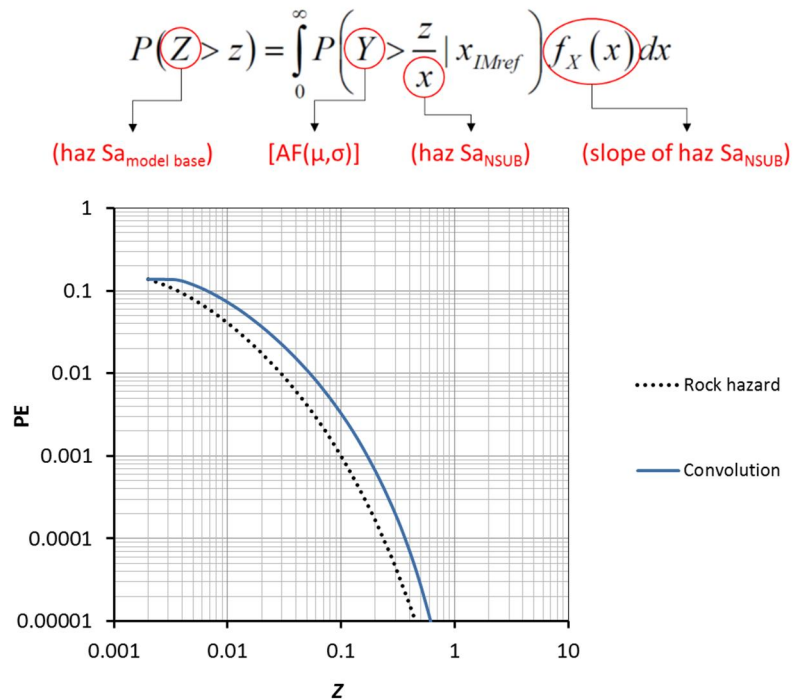


Figure 6. Example convolution results of rock hazard curve and probability distribution of site amplification factors (Stewart et al. 2014).

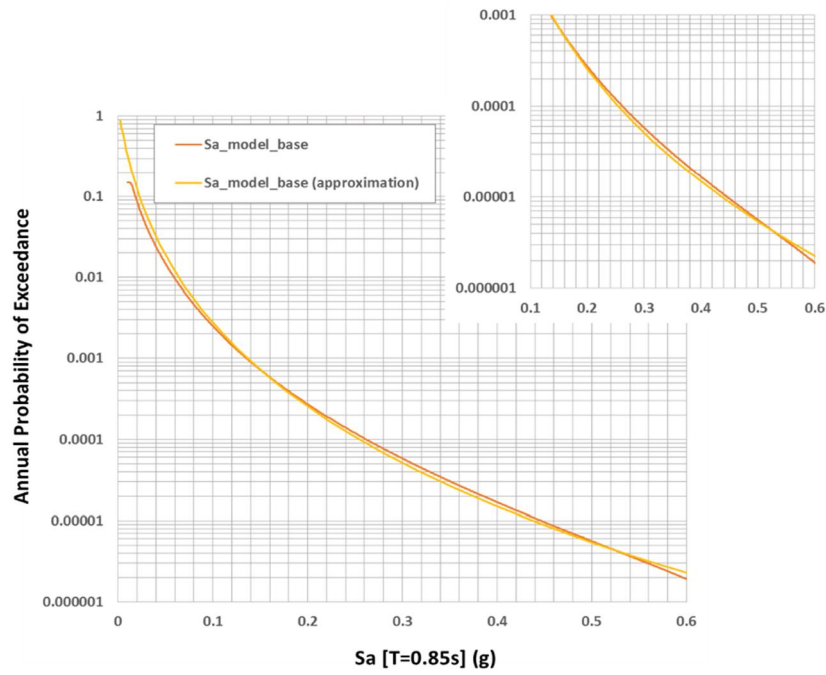


Figure 7. Convolved spectral acceleration ($T=0.85s$) hazard curve at the base of 2D model at Eemshaven and approximation with a lognormal distribution. Lognormal distribution with $\mu_{ln(SA)} = -5.05$ and $\sigma_{ln(SA)} = 0.99$.

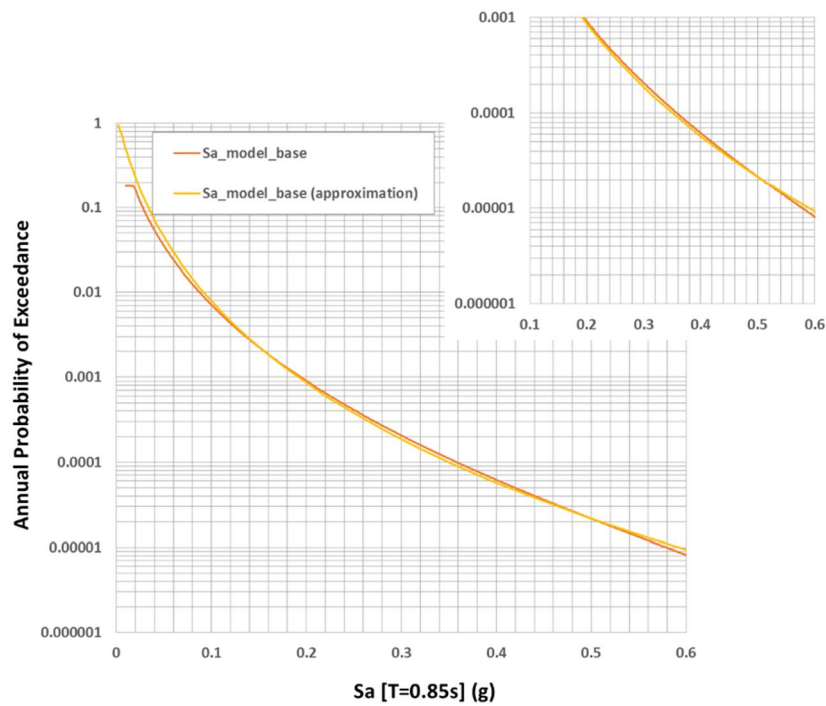


Figure 8. Convolved spectral acceleration ($T=0.85s$) hazard curve at the base of 2D model at Delfzijl and approximation with a lognormal distribution. Lognormal distribution with $\mu_{ln(SA)} = -4.62$ and $\sigma_{ln(SA)} = 0.96$.

4.3 $CRR_{M=7.5}$ in sand deposits

The probability distribution of the cyclic resistance at a reference magnitude $M=7.5$ (or 15 cycles) of sand layers with no clay laminations present at the Eemshaven area was estimated from the equation below proposed by Boulanger and Idriss (2014) using:

- the probability distribution of local q_{c1Ncs} values from CPT data that classified as Soil Behavior Type 6 per Robertson (1990) classification (Fugro 2016c). These q_{c1Ncs} values include thin layer correction and fines content correction (Fugro 2016c). In a uniform model, soil properties are assumed to be constant within an entire layer. This may lead to a significant overestimation of probabilities of failure when composite behavior is more accurately described by the spatial averages of individual data points (e.g. Vanmarcke 2011). A sensitivity study into such volume effects indicates that the use of spatially distributed resistance values gives a result that is similar to the use of median resistance values in a uniform model, see Appendix G for further details. This is why the median of local q_{c1Ncs} values was selected for use with the Boulanger and Idriss (2014) relationship between q_{c1Ncs} and CRR.
- the model uncertainty term $\varepsilon_{\ln(R)}$ proposed by Boulanger and Idriss (2014) has a normal distribution with a mean value of 0 and a standard deviation of 0.2:

$$CRR_{M=7.5, \sigma'_v=1atm} = \exp \left(\frac{q_{c1Ncs}}{113} + \left(\frac{q_{c1Ncs}}{1000} \right)^2 - \left(\frac{q_{c1Ncs}}{140} \right)^3 + \left(\frac{q_{c1Ncs}}{137} \right)^4 - 2.60 + \varepsilon_{\ln(R)} \right)$$

On the basis of the above, a probability distribution of the $CRR_{M=7.5}$ has been derived, using the local median q_{c1Ncs} value and the $CRR_{M=7.5}$ curve of Boulanger and Idriss (2014).

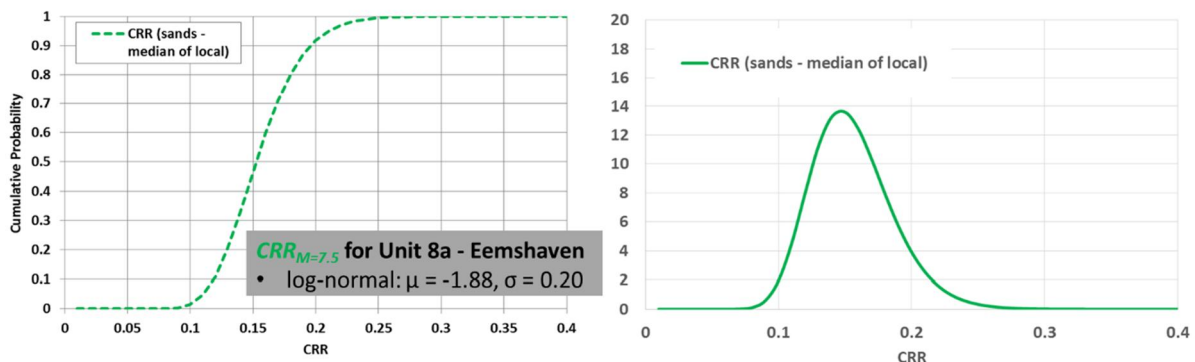


Figure 9. Probability distribution (left) and probability density function (right) of $CRR_{M=7.5}$ for sands at Eemshaven based on the median of local q_{c1Ncs} values.

4.4 $CRR_{M=5.0}$ in laminated deposits

The liquefaction triggering resistance from CPT measurements in laminated deposits appears to underestimate the triggering resistance of these deposits when compared to results from cyclic laboratory tests on laminated “undisturbed” samples (Fugro 2016c). This is most likely due to the significant influence of the clay layers on the CPT tip resistance measured within the thin “sandwiched” sand layers whose thickness is less than 10 to 20 cm.

Interpreted advanced cyclic laboratory tests on “undisturbed” laminated samples and numerical simulation results were used to develop a probability distribution of the cyclic resistance of laminated deposits at the Delfzijl side of the levee for locations where Unit 8 is present for use in FORM analyses as discussed in detail in Appendix D.

Cyclic resistance was defined at a reference magnitude $M=5.0$ (or 4 cycles) using the Boulanger and Idriss (2014) Magnitude Scaling Factor. It is noted that CRR for layered sands defined at 4 cycles (or for $M=5.0$) is used only as a reference to identify which triggering curve is used in the numerical analyses, since in the

constitutive models used in the numerical evaluations to simulate sand behavior, the complete liquefaction triggering curve is used rather than one value.

The probability distributions of the $CRR_{M=5}$ for laminated deposits after accounting for volume effects (spatial averaging, see Appendix G) are shown in Figure 10. Note: the means and standard deviations in Figure 10 concern the natural logarithms of the CRRs.

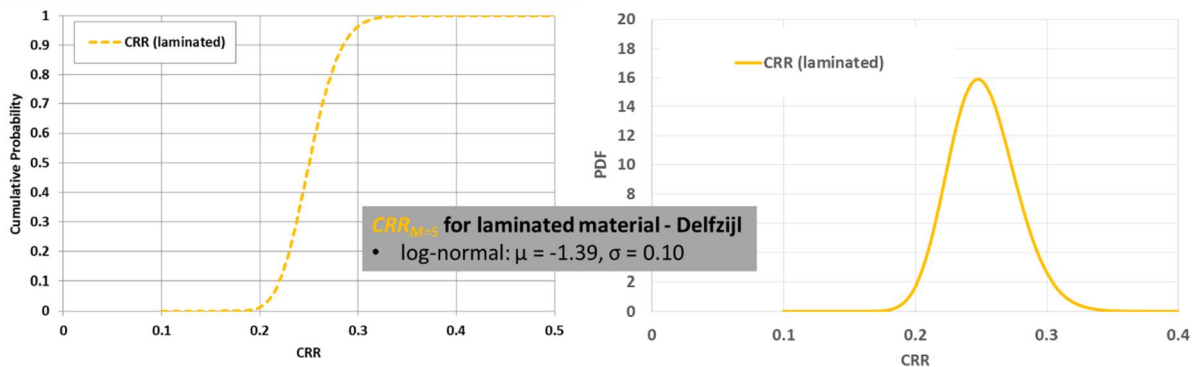


Figure 10. Probability distribution (left) and probability density function (right) of $CRR_{M=5}$ for laminated deposits at Delfzijl before and after accounting for volume effects.

The probability distribution of the CRR for laminated deposits shown above has been specified for a different magnitude than the non-laminated wadzand deposits encountered at Eemshaven. For the non-laminated wadzand deposits encountered at Eemshaven, the Boulanger and Idriss (2014) empirical correlation of $CRR_{M=7.5}$ (defined as CRR at 15 cycles) with q_{c1Ncs} was used for the estimation of liquefaction triggering resistance. For the laminated sand and clay layers within the wadzand deposits interpreted lab results were used to estimate liquefaction triggering resistance at 4 cycles ($CRR_{M=5,0}$), which is the estimated equivalent number of cycles for an $M=5$ earthquake (the primary contributor to the ground motion hazard for the return periods of interest) using the Boulanger and Idriss (2014) Magnitude Scaling Factor.

4.5 Uncertainty related to residual strength ($\epsilon_{su/p'}$)

Post-earthquake stability analyses were performed by assigning residual strength (i.e. defined as the ratio of residual undrained shear strength and in situ initial vertical effective stress, S_r/σ_{vc}') for areas where the maximum excess pore pressure during shaking exceeded a specified threshold indicative of liquefaction. The following distributions were considered:

- mean residual strength and standard deviation as proposed by Kramer and Wang (2015), which is about 0.37 for the range of conditions applicable (green lines in Figure 11 below). This is considered to be the preferred basis for probabilistic analyses since it includes an empirically based uncertainty term, without bias. The proposed relationship for mean residual strength by Kramer and Wang (2015) is a function of normalized SPT blowcounts (N_{160}). We have used Idriss and Boulanger (2008) correlation to convert N_{160} to q_{c1Ncs} . In order to account for the uncertainty in the conversion factor we have also considered a higher value for the standard deviation of 0.45 (red lines in Figure 11 below). We note that FORM analyses were performed considering both standard deviation values and results were found to be largely similar.
- residual strength proposed by Idriss and Boulanger (2008) assuming void redistribution effects are significant. A clear definition of the uncertainty in residual strength estimates is not available. An estimate of the uncertainty on residual shear strength was developed assuming that the proposed curve represents median values (despite a likely safe bias) and using engineering judgment to develop an estimate of the standard deviation on the assumed median residual strength curve. More details are provided in Appendix E. This residual strength distribution has been used to evaluate the sensitivity of the calculated FORM influence coefficients to different assumptions concerning residual strength.

A comparison of the two residual strength distributions considered is shown in Figure 11.

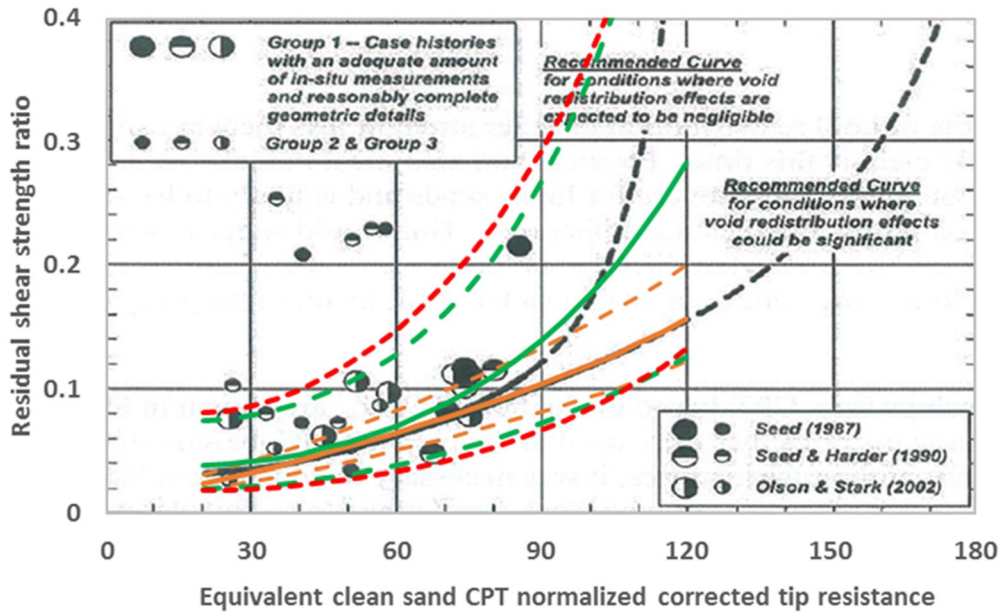


Figure 11. Uncertainty related to residual strength (95%-confidence interval) based on Kramer and Wang (2015) using the standard deviation proposed by the authors (green dashed curves) and an increased standard deviation of 0.45 (red dashed curves) to account for uncertainty in the conversion from $(N1)_{60}$ to q_{c1Ncs} , and Idriss and Boulanger (2008) assuming void redistribution and engineering judgment for the estimation of standard deviation (orange curves).

4.6 Model Uncertainty (ϵ_M)

This term accounts for the potential difference between numerical model prediction and observed levee response. The expert panel (2016) has recommended a comparison of constitutive models and their implementations for informing choices concerning model uncertainty. Various sensitivity studies have shown that the differences between the computed crest settlements with two different constitutive models (UBCsand and PM4sand) are relatively small (Fugro 2016a). A comparison of computed settlements with different computer codes (i.e. different implementations of these constitutive models) could not be carried out because of time constraints. In view of this the model uncertainty has conservatively been assumed to be considerable, even though the differences between different computer codes are expected to be significantly smaller than those between different constitutive models. A detailed discussion on the characterization of model uncertainty is included in Appendix F.

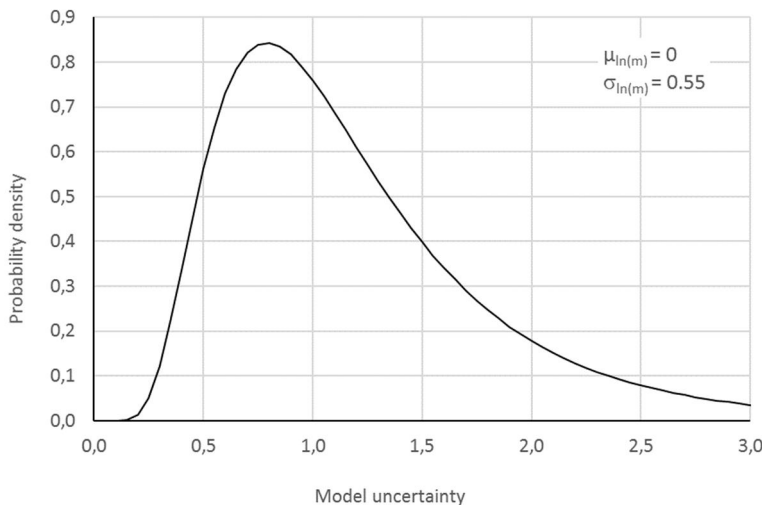


Figure 12. Model uncertainty.

4.7 Uncertainties related to motion characteristics

Ground motion characteristics mainly relate to amplitude, frequency content, and duration, but also to other characteristics of the ground motion that have to do with the details of the ground motion time history such as phasing, presence of velocity pulses that may create larger slope displacements, etc. The FE analyses have been conducted using motions that have been matched to a target spectral shape. Sensitivity analyses have been conducted to assess the variations in response for 7 different, two component motions (Fugro 2016a).

The effect of the uncertainties related to the characteristics of ground motion can be handled via scenarios. In that case, failure probabilities are first calculated for a set of motions and then combined, see Appendix H. For deriving design values for an assessment for an individual ground motion, FORM-analyses have been conducted using a single motion with a duration D_{5-75} that is greater than the expected durations for 3000-6000 year return period ground motions in Groningen. Sensitivity analyses were also conducted with a shorter duration motion because the spectral acceleration at the design point has a significantly longer return period. In Groningen, duration and spectral acceleration are inversely correlated (Bommer et al. 2015). Longer return periods are associated with higher spectral accelerations and smaller duration motions.

4.8 Overview of stochastic variables

An overview of the stochastic variables, their distributions, autocorrelations and representative values is given in Table 1.

Table 1. Overview of stochastic variables.

Variable	Unit	Distribution type	Distribution parameters*	Mean (m) and standard deviation (sd)*	Motivation	Spatial correlation (also see section 7.4)
Spectral acceleration (T=0.85s) at NSUB (SA _{NSUB})**	g	Lognormal	Eemshaven $\mu = -5.77$ $\sigma = 1.12$ Delfzijl $\mu = -5.61$ $\sigma = 1.10$	Eemshaven m = 0.0058 g sd = 0.0092 g Delfzijl m = 0.0067 g sd = 0.0103 g	From KNMI hazard curves for Groningen	Strongly correlated over distances of several km
Spectral acceleration (T=0.85s) at base of model (SA _{model_base})	g	Lognormal	Eemshaven $\mu = -5.05$ $\sigma = 0.99$ Delfzijl $\mu = -4.62$ $\sigma = 0.96$	Eemshaven m = 0.0105 g sd = 0.0135 g Delfzijl m = 0.0156 g sd = 0.0135 g	Convolution of amplification factor distribution at base of 2D FE model and hazard curve at NSUB following Stewart et al (2014) procedure. The estimation of the amplification factor at base of FE models is described in Appendix C.	Strongly correlated over distances of several km
CRR _{M=7.5} in sand deposits	-	Lognormal	$\mu = -1.88$ $\sigma = 0.20$ (distribution of point values in the regional data set: $\mu = -1.80$ $\sigma = 0.30$)	m = 0.16 sd = 0.03 (distribution of point values in the regional data set: m = 0.17 sd = 0.05)	Volume effects have been accounted for to obtain a distribution from a local data set of q _{c1Ncs} -values that can be used in a uniform model. For further details, see Appendix G. The distribution of point values rests on a convolution of the model uncertainty term in the CRR-relationship by Boulanger & Idriss (2014), with $\mu = 0$ and $\sigma = 0.2$, and the distribution of q _{c1Ncs} values in sand from a regional data set. This distribution has only been used for sensitivity analyses.	Strongly correlated over distances of several km for a given geological unit. Motivation: The CRR _{M=7.5} -values are derived from an empirical relationship that rests on back-calculations of historic events. Length effects are reflected in the individual historic observations. The above means that the uncertainty related to CRR _{M=7.5} could be thought of as a model uncertainty which is typically assumed to be strongly spatially correlated.
CRR _{M=5.0} in laminated deposits (from lab data)	-	Lognormal	$\mu = -1.39$ $\sigma = 0.10$ (without spatial averaging: $\mu = -1.40$ $\sigma = 0.20$)	m = 0.25 sd = 0.03 (without spatial averaging: m = 0.25 sd = 0.05)	Based on regressions of lab test results and numerical simulations (see Appendix D). Volume effects have been accounted for. For a discussion on volume effects, see Appendix G.	$\rho_0 = 0 - 0.5$ k = 100-150m (+ sensitivity analyses) A correlation distance (k) that is in line with the value used for material properties in slope stability analyses in the Netherlands seems justified. The variance is largely related to the variations in clay content (void ratio). For a given void ratio, the resistances are spatially correlated. A review of CPT-

Variable	Unit	Distribution type	Distribution parameters*	Mean (m) and standard deviation (sd)*	Motivation	Spatial correlation (also see section 7.4)
						data indicate that similar clay contents extend over distances of tens to hundreds of meters. A lower limit of the autocorrelation function (ρ_0) greater than zero seems reasonable because there is also an element of (spatially correlated) knowledge uncertainty related to the $CRR_{M=5.0}$ in layered deposits.
$\epsilon_{Su/p'}$ (uncertainty related to Su/p' given median value of q_{c1Ncs})	-	Lognormal	$\mu = 0$ $\sigma = 0.45$ $\mu = 0$ $\sigma = 0.15$	$m = 1.11$ $sd = 0.52$ $m = 1.01$ $sd = 0.15$	Su/p' from Kramer and Wang (2015). $Su/p' = f(q_{c1Ncs,50\%}) \cdot \epsilon_{Su/p'}$ With $f(q_{c1Ncs,50\%})$ from Idriss & Boulanger (2008) with void ratio distribution. For further details, see Appendix E.	Strongly correlated over distances of several km (essentially model uncertainty)
Geometric parameters (crest height, width etc.)	m	Deterministic	-	-	Dimensions are well known	-
Model Uncertainty	-	Lognormal	$\mu = 0$ $\sigma = 0.55$	$m = 1.16$ $sd = 0.69$	Distribution based on engineering judgement, see Appendix F. The distribution corresponds to a probability of an error of at least a factor 2 of 10%.	Strongly correlated over distances of several km

* The values of μ and σ in this table are the means and standard deviations of the natural logarithms of the lognormally distributed variables. They are not the means and standard deviations of the lognormally distributed variables themselves, which have been indicated by m and sd respectively.

** This distribution will not play a role in the FORM-analyses. It is only mentioned here to be able to calculate the difference between the design value of the Spectral acceleration ($T=0.85s$) with and without a design value for the uncertainty in the response analysis.

5 Action item 2: FORM analyses using the simplified liquefaction procedure

The objective of this action item is to “get a feel” for the relative importance of the various uncertainties from probabilistic analyses with the simplified liquefaction procedure. The usefulness of this action item rests on the premise that the relative importance of stochastic variables that determine liquefaction triggering is broadly similar within a simplified liquefaction triggering analysis (the basis of the screening method) and more advanced FEM deformation analyses. The results presented below have been used for selecting the start values for the FORM-analyses with the FEM model, to reduce the required number of iterations. They have also been used for quality assurance, to make it easier to spot errors.

5.1 Limit state function

The simplified liquefaction procedure involves an evaluation of a “factor of safety” (FS_{liq}) against liquefaction (see Idriss & Boulanger 2008; Boulanger & Idriss 2014; Green et al. 2016). Note that FS_{liq} is a stochastic variable and not a partial factor.

$$FS_{liq} = CRR_{7,5,1atm} / CSR_{7,5,1atm} \quad (5)$$

$$CSR_{7,5,1atm} = 0,65 \cdot \sigma_v / \sigma'_v \cdot PGA/g \cdot r_d \cdot 1/MSF \cdot 1/K_\sigma \quad (6)$$

$$CSR_{7,5,1atm} = c \cdot PGA \quad (7)$$

$$CRR_{7,5,1atm} = \exp[q_{c1Ncs}/113 + (q_{c1Ncs}/1000)^2 - (q_{c1Ncs}/140)^3 + (q_{c1Ncs}/137)^4 - C_o + \varepsilon_{ln(CRR)}] \quad (8)$$

Since $FS_{liq} < 1$ implies liquefaction, the limit state function for liquefaction triggering can be written as follows:

$$Z = 1 - CRR_{7,5,1atm} / CSR_{7,5,1atm} \quad (9)$$

or (similar to Boulanger & Idriss 2014):

$$Z = \ln(CRR_{7,5,1atm}) - \ln(CSR_{7,5,1atm}) \quad (10)$$

or:

$$Z = \ln(CRR_{7,5,1atm}) - \ln(c \cdot PGA) \quad (11)$$

Where:

$CRR_{7,5,1atm}$	Cyclic resistance ratio (-)
$CSR_{7,5,1atm}$	Cyclic stress ratio (-)
PGA	Peak ground acceleration at the surface of the soil profile (m/s^2)
g	Gravitational acceleration (m/s^2)
σ_v	Total effective stress (kPa)
σ'_v	Effective vertical stress (kPa)
r_d	Depth reduction factor (-)
$\varepsilon_{ln(CRR)}$	Uncertainty term
MSF	Magnitude scaling factor (-)
K_σ	Overburden correction factor (-)
c	Constant (-)
q_{c1Ncs}	Equivalent, normalized cone resistance for clean sand (-)
C_o	Constant (-)

A PSHA has been carried out to estimate the seismic hazard at the top of North Sea Upper Base (NSUB) at a depth of about 350m by KNMI. For the estimation of PGA at the ground surface, amplification factors or functions (AF) have been estimated as a function of the spectral acceleration at NSUB by Bommer et al. (2015).

For every location and period, the parameter values of the following equation can be found in “V2_Site Response Zonations_date.xlsx”:

$$\ln(AF) = f_1 + f_2 (PGA_{NSUB} + f_3) / f_3 + u \cdot \sigma_{\ln AF} \quad (12)$$

Where:

AF Amplification factor (-)

f_1, f_2, f_3 Constants (-)

PGA_{NSUB} Peak ground acceleration at North Sea Upper Base (g)

u Standard normal variable (-)

$\sigma_{\ln AF}$ Standard deviation of the natural logarithm of the uncertainty related to the amplification function (-)

5.2 Input of probabilistic analyses

An overview of the stochastic variables and their distributions is given in Table 2.

Table 2. Overview of stochastic variables.

Variable	Unit	Distribution type	Distribution parameters	Mean (m) and standard deviation (sd)*	Motivation
PGA	g	Lognormal	$\mu = -3.95$ $\sigma = 0.61$	$m = 0.0232$ g $sd = 0.0156$ g	The PGA hazard curve was estimated following the procedure by Bazzurro and Cornell (2004) and Stewart et al. (2014) by a convolution of the hazard curve at top of bedrock (PGA_{NSUB}) with the probability distribution of the site amplification factor by Bommer et al (2015) for Eemshaven (i.e. zone number 1035). Monte Carlo simulations were also performed for the convolution of the bedrock hazard curve and the site amplification probability distribution and similar results were obtained. The hazard curve of PGA at the ground surface was approximated with a lognormal distribution.
$CRR_{M=7.5}$ in sand deposits	-	Lognormal	$\mu = -1.88$ $\sigma = 0.20$	$m = 0.16$ $sd = 0.03$	Based on a convolution of the model uncertainty term in the CRR-relationship by Boulanger & Idriss (2014), with $\mu = 0$ and $\sigma = 0.2$, and the median of local q_{c1Ncs} -values in sand, see Appendix G for further details.

5.3 Results of FORM-analyses

The squared influence coefficients per stochastic variable are shown in Figure 13 below. The influence coefficients are identical for different values of the constant c (see equation (7)), and thus the same for different (target) reliabilities. For more information about FORM, see Appendix A.

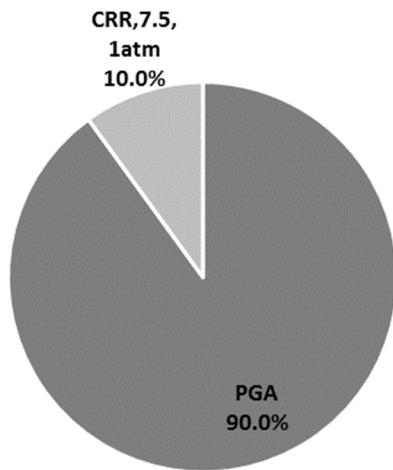


Figure 13. FORM-results for a simplified liquefaction triggering analysis.

For a range of c -values (see equation (7)) that seem reasonable for Eemshaven, the calculated reliability indices range from about 2.2 to 3.2.

5.4 Discussion

The results shown above are in line with:

1. the fact that the return period of the earthquake load is widely regarded as an all-important parameter,
2. the fact that a widely used “deterministic” triggering relationship corresponds to merely a 16%-quantile for model uncertainty (Boulangier & Idriss 2014).

6 Action item 3: FORM analyses using the 2D effective stress model

The objective of this action item is to “get a feel” for the relative importance of the various uncertainties from probabilistic analyses with the Fugro model. For more information about FORM, see Appendix A.

6.1 Limit state function

The limit state function is:

$$Z = c_{crit} - m \cdot C \quad (13)$$

Where

- c_{crit} Critical crest settlement (m); $c_{crit} = 3$ m
- C Computed crest settlement (m)
- m Model uncertainty factor (-)

Crest settlements are calculated with dynamic effective stress FEM-analyses. For further details on the calculation procedure, the reader is referred to the guideline prepared by Fugro (2016b).

6.2 Input of probabilistic analyses

For an overview of the stochastic variables and their distributions, the reader is referred to Table 1 in chapter 4. The stratigraphies for the Eemshaven and Delfzijl levees that have been considered in FORM-analyses are given in Figure 14 and Figure 15 below. Conservative stratigraphies have deliberately been selected to minimize the gap between reliability indices close to target reliability indices. Additional stratigraphies have been considered in Fugro (2016a) as a part of sensitivity analyses.

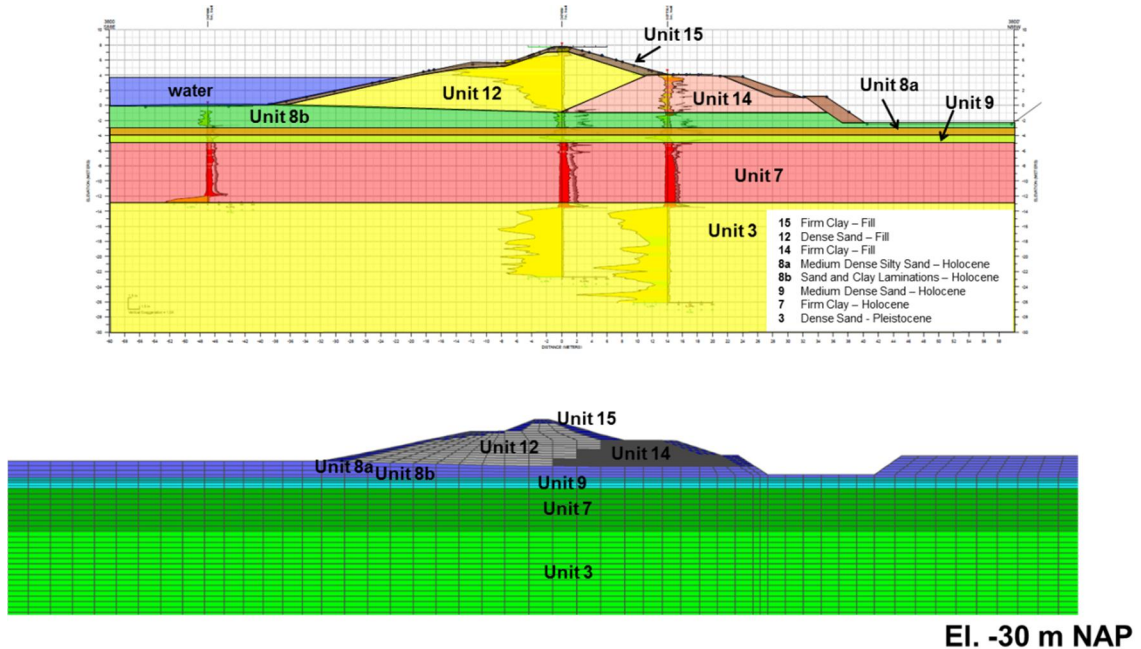


Figure 14. The stratigraphy for the Eemshaven cross-section considered in the FORM-analysis.

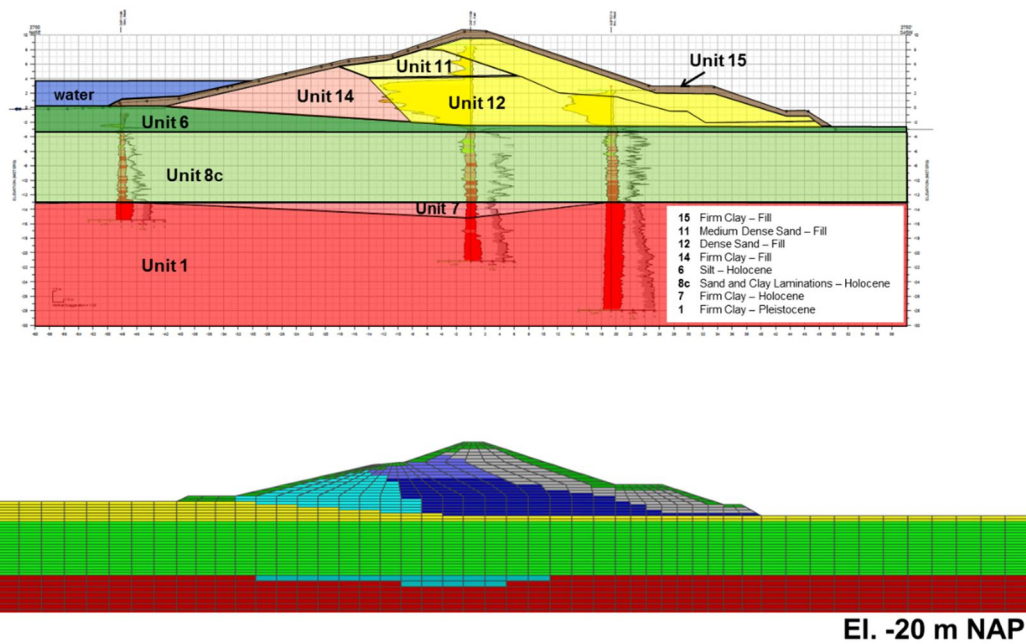


Figure 15. The stratigraphy for the Delfzijl cross-section considered in the FORM-analysis.

6.3 Results of FORM-analyses

The results of the FORM analyses using the 2D FEM results are presented in this section. The following cases were examined:

Base case

- Eemshaven cross-section; S_u/p' according to Kramer & Wang (2015); ground motion 4; using the median of local q_{c1Ncs} -values.
- Delfzijl cross-section; S_u/p' according to Kramer & Wang (2015); ground motion 4; using the median of local q_{c1Ncs} -values.

Sensitivity analyses

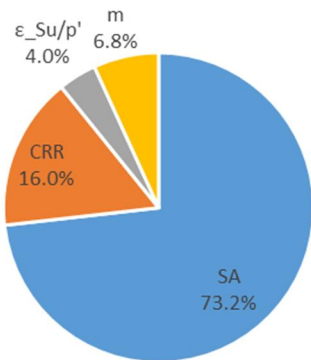
- Eemshaven cross-section; S_u/p' according to Kramer & Wang (2015); ground motion 6; using the median of local q_{c1Ncs} -values.
- Delfzijl cross-section; S_u/p' according to Kramer & Wang (2015); ground motion 6; using the median of local q_{c1Ncs} -values.
- Eemshaven cross-section; S_u/p' according to Idriss & Boulanger (2008); ground motion 4; using a regional data set of q_{c1Ncs} -values without spatial averaging.
- Delfzijl cross-section; S_u/p' according to Idriss & Boulanger (2008); ground motion 4; using a regional data set of q_{c1Ncs} -values without spatial averaging.

All FORM-analyses have been performed using a response surface. For both base cases, the design point (crest settlement and partial derivatives) has been verified using targeted FE-analyses (usually a set of 9 FE-analyses). The same applies to sensitivity analyses no. 3 and 4. For sensitivity analyses no. 1 and 2, only the crest settlement in the design point has been verified with a single, targeted FE-analysis.

The squared influence coefficients per stochastic variable are shown in Figure 16 to Figure 18 below for the cases examined. The calculated reliability indices are also shown on the figure for every case.

For a detailed overview of the results of the FORM-analyses, the reader is referred to Appendix I.

Eemshaven- KW Su/p' -motion 4
($\beta = 5.03$)



Delfzijl - KW Su/p' - motion 4
($\beta = 5.49$)

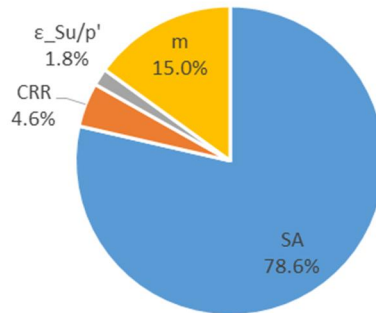
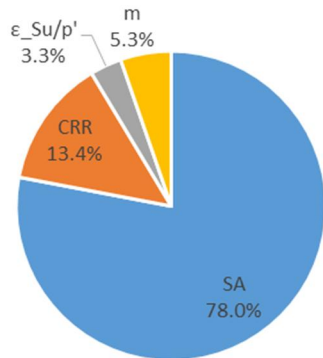


Figure 16. Base case A (left) and B (right): squared influence coefficients and reliability indices from FORM-analyses with the 2D FE model with Su/p' according to Kramer & Wang (2015) and the median of local $qc1Ncs$ -values, for ground motion 4.

Eemshaven - KW Su/p' -motion 6
($\beta = 5.28$)



Delfzijl - KW Su/p' - motion 6
($\beta = 5.32$)

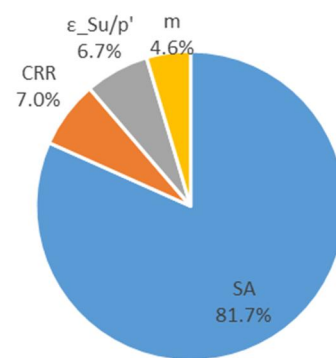
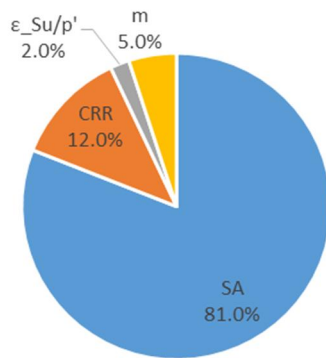


Figure 17. Sensitivity analyses 1 (left) and 2 (right): squared influence coefficients and reliability indices from FORM-analyses with the 2D FE model with Su/p' according to Kramer & Wang (2015) and the median of local $qc1Ncs$ -values, for ground motion 6.

Eemshaven - IB S_u/p' - motion 4
($\beta = 4.90$)



Delfzijl - IB S_u/p' - motion 4
($\beta = 5.01$)

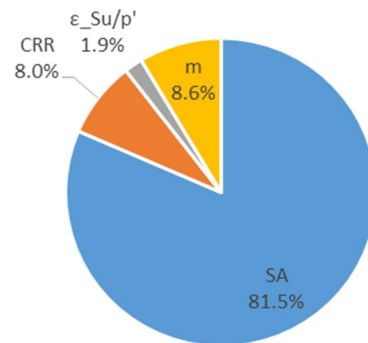


Figure 18. Sensitivity analyses 3 (left) and 4 (right): squared influence coefficients and reliability indices from FORM-analyses with the 2D FE model with S_u/p' according to Idriss & Boulanger (2008), using a regional data set of q_{c1NGS} -values without spatial averaging, for ground motion 4.

6.4 Discussion

The calculated influence coefficients for Eemshaven and Delfzijl appear broadly similar. The uncertainty related to the spectral acceleration is relatively important. This is in line with the results of the FORM-analyses for liquefaction triggering with the simplified liquefaction procedure (see chapter 5). It is also in line with the observation that the return period of the seismic action is widely considered to be an all-important parameter.

The calculated reliability indices are high, even though conservative assumptions have been made concerning stratigraphy: a reliability index of 5 corresponds to a probability of failure of about $1/3.500.000$ per year ($2,9 \cdot 10^{-7}$ per year). The calculated reliability indices are significantly greater than the ones calculated for liquefaction triggering in chapter 5. This is consistent with the fact that the FORM-analysis in chapter 5 concerns the probability that $FSI_{iq} < 1$ somewhere. This is not the same as actual failure.

Analyses were conducted for two different residual strength distributions. As was to be expected on the basis of the similarities between the relationships presented in Figure 11 for lower values of q_{c1NGS} , the calculated reliability indices and influence coefficients are broadly similar.

A sensitivity analysis with a shorter duration motion shows a higher reliability index. The influence coefficient of ground motion is somewhat reduced.

The calculated influence coefficients are broadly similar across all cases.

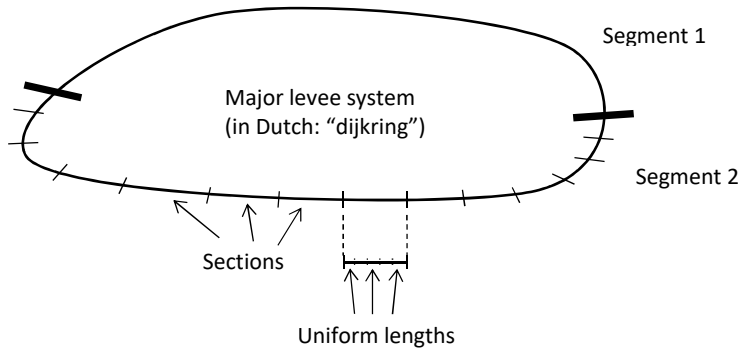


Figure 20. Major levee system, segments, sections and cross-sections.

The failure probability for a uniform length, $P(F_i)$, is the probability that the limit state function is smaller than zero in a 2-dimensional or cross-sectional analysis:

$$P(F_i) = P(Z_i < 0) \quad (14)$$

Where

Z_i Limit state function of uniform length i ($i=1..n$); $Z_i < 0$ indicates failure

A segment can be thought of as a series system consisting of numerous uniform lengths (grouped into sections). A segment's failure probability, $P(F_{\text{system}})$, follows from²:

$$P(F_{\text{system}}) = P(Z_1 < 0 \cup Z_2 < 0 \cup \dots \cup Z_n < 0) \quad (15)$$

The failure probability of a series system lies between the following bounds:

$$P(F_{\text{system}}) = \max(P(Z_i < 0)) \quad \text{Lower bound (perfectly correlated limit state functions)} \quad (16)$$

$$P(F_{\text{system}}) = 1 - \prod_{i=1..n} (1 - P(Z_i < 0)) \quad \text{Upper bound (independent limit state functions)} \quad (17)$$

For sufficiently small failure probabilities, the upper bound can be approximated by:

$$P(F_{\text{system}}) \approx \sum(P(Z_i < 0)) \quad (18)$$

When the limit state functions of the different uniform lengths are strongly correlated, the system failure probability tends to the lower bound. When the limit state functions are weakly correlated, the system failure probability tends to the upper bound. The difference between expressions (16) and (17) is also strongly influenced by variations in cross-sectional failure probabilities. A single weak spot may strongly influence a series-system reliability, regardless of spatial correlations.

The system failure probability for a particular failure mechanism can be calculated on the basis of:

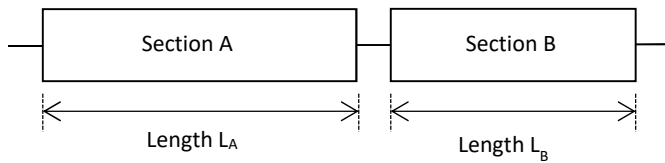
1. cross-sectional failure probabilities (identical throughout each section),
2. the effect of spatial correlations within each section and
3. the correlations between sections.

This is illustrated by Figure 21. Note that uniform lengths could be treated like sections when calculating a segment's failure probability. A distinction is made here because the homogeneity within sections allows for the use of relatively efficient computational techniques to calculate the failure probability of a section. A section is essentially a series system of uniform lengths, i.e. a system of correlated components. It can also be modelled as a series system of independent equivalent lengths. These independent equivalent lengths depend on the correlations between uniform lengths. With such an independent equivalent length, the failure

² For reasons of simplicity, only a single failure mechanism is considered here.

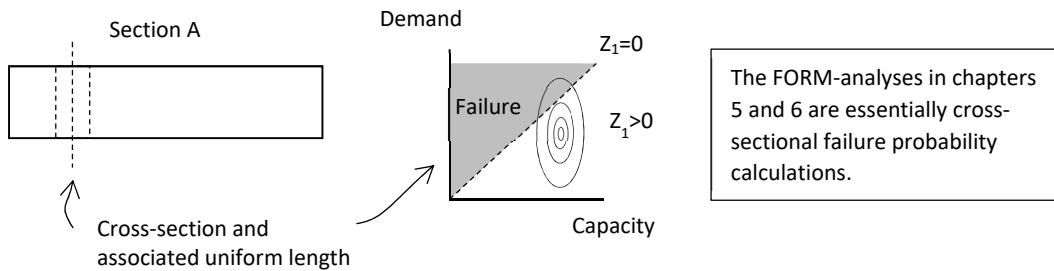
probability for a single uniform length can be scaled directly to the failure probability of an entire section (see e.g. Vrouwenvelder 2006).

Consider a series system (segment) that consists of two components (sections)

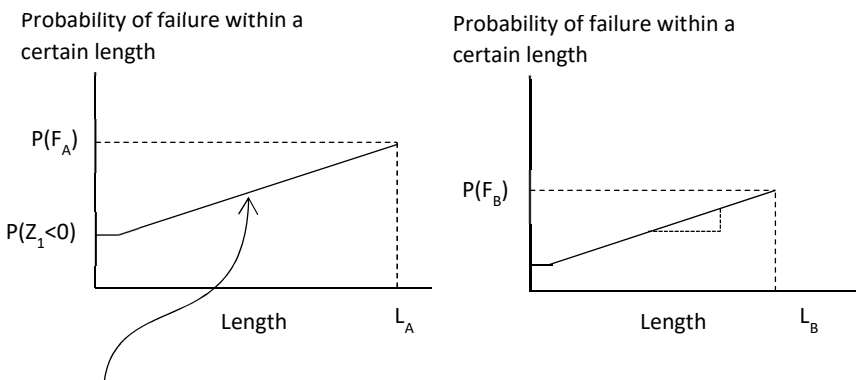


1. Calculate cross-sectional failure probabilities

(example for section A only)



2. Calculate each section's failure probability, based on spatial correlations and cross-sectional reliabilities

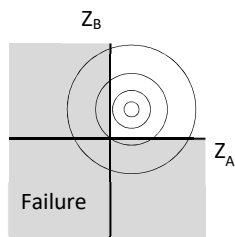


The steepness of this line depends on the (spatial) autocorrelation function of the limit state function Z_1

3. Combine the sections, taking their correlations and varying reliabilities into account

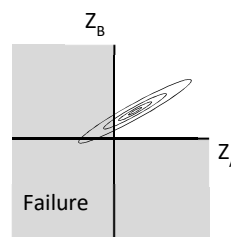
$$P(F_{\text{system}}) = P(F_A \cup F_B) = P(Z_A < 0 \cup Z_B < 0)$$

No correlation ($\rho_{Z_A Z_B} = 0$)



$$P(Z_A < 0 \cup Z_B < 0) \approx P(Z_A < 0) + P(Z_B < 0)$$

Strong correlation ($\rho_{Z_A Z_B} \approx 1$)



$$P(Z_A < 0 \cup Z_B < 0) \approx \max(P(Z_A < 0) , P(Z_B < 0))$$

Figure 21. Schematic overview of a system reliability analysis.

When engineers evaluate the reliability of e.g. a dike section using a semi-probabilistic or deterministic method, they carry out a 2-dimensional analysis. To be able to evaluate an individual cross-section without having to carry out a full system-level reliability analysis, the system-level reliability requirement has to be transformed into a cross-sectional reliability requirement.

7.2 The length effect and cross-sectional target reliabilities

When the limit state functions of different uniform lengths are not perfectly correlated, the system failure probability increases with the number of uniform lengths (Figure 22). This means that the system failure probability increases with length. This phenomenon is called the length effect.

The above can be understood as follows. When capacity is uncertain *and* spatially variable, it is uncertain (1) which spot is actually the weakest and (2) how weak this weakest spot actually is. This also explains why people that inspect levees during high waters do not stand still: the probability that they observe a sign of weakness increases with every step they take. Note that the spatial variability of demand can also lead to a length effect: the probability of observing a particular seismic demand *somewhere* in Groningen is higher than the probability that it is observed *at any specific location* in Groningen.

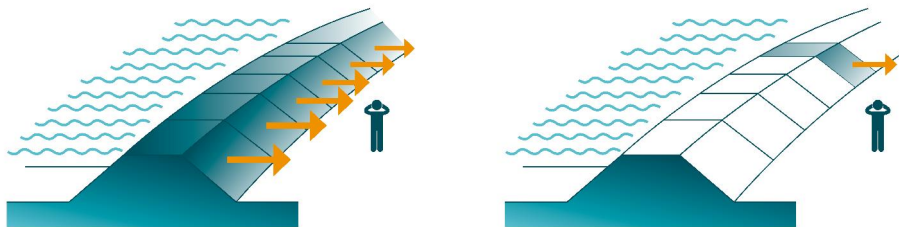


Figure 22. The length effect: the greater the number of uniform lengths that could fail independently, the greater the probability of flooding.

The Dutch flood protection standards are defined in terms of maximum allowable probabilities of flooding per segment (“dijktraject”). Cross-sectional target reliabilities for evaluating the probability of severe earthquake damage can be derived from these standards with the following expression:

$$P_T = P_{\max} \cdot f / P_{F|D} / N \quad (19)$$

with:

$$N = a \cdot L / b \quad (20)$$

Where

- P_T Cross-sectional target failure probability for a seismic stability assessment (per year)
- P_{\max} Maximum allowable probability of flooding (per year)
- f Maximum allowable contribution of instability to the probability of flooding (-)
- $P_{F|D}$ Probability of flooding given severe earthquake damage, defined as a crest settlement $\geq 3\text{m}$ (-)
- N Length effect factor for severe earthquake damage (-)
- L Length of segment (m)
- a Fraction of the total length of the segment that dominates the probability of failure of the segment for the failure mechanism under consideration (-)
- b Independent equivalent lengths within the abovementioned part of the segment (m)

The parameters a and b model a segment that consists of different sections with different characteristics in a simplified, equivalent manner, as shown in Figure 23. The failure probability of a segment is usually determined by a relatively short distance over which the probabilities of failure are relatively high, which is expressed by the a -value. Note that failure probabilities are usually plotted on a log-scale because they easily vary of orders

of magnitude; combining failure probabilities of e.g. 1/1000 and 1/100.000 gives a system failure probability close to 1/1000. Within the “critical length” (i.e. “ $a \cdot L$ ”), the effect of decay of spatial correlation can be modelled by means of “independent equivalent lengths”. This is reflected by the b-value.

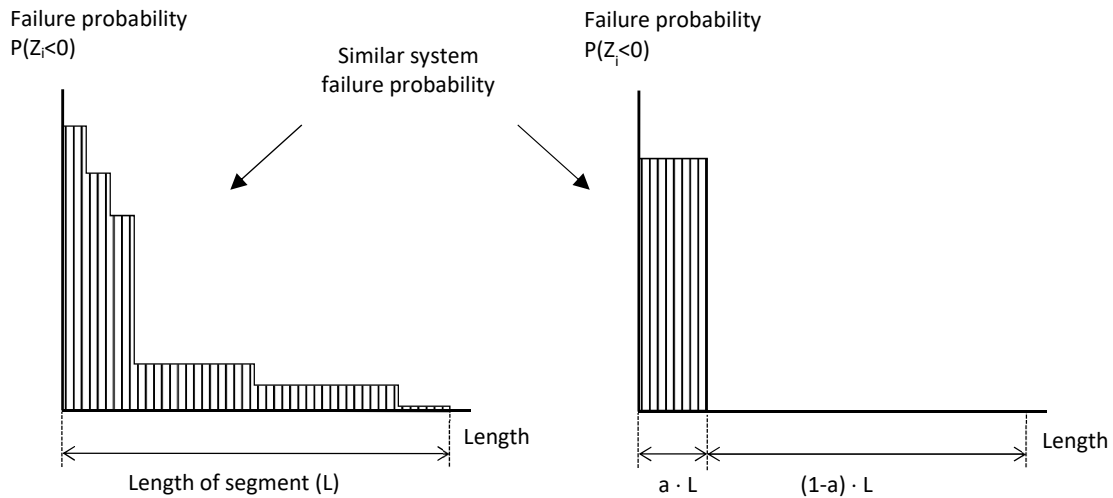


Figure 23. A simplified, equivalent way of describing a segment's reliability (the widths of the bars are independent equivalent lengths, or b-values).

The parameter values that have been assumed so far are shown in Table 3, together with the resulting target reliabilities.

Table 3. From standard of protection to cross-sectional target reliabilities for seismic stability assessments. Original values.

Variable	Unit	Segment	
		6_6 (includes Eemshaven)	6_7 (includes Delfzijl)
P_{max}	per year	1/1,000	1/3,000
f	-	0.24	0.24
$P_{F D}$	-	0.1	0.1
$P_{T,segment}$	per year	0.0024	0.0008
L	m	46100	38600
a	-	0.033	0.033
b	m	50	50
N	-	31.4	26.5
P_T	Per year	7.64E-05	3.02E-05
β_T	-	3.79	4.01

The values of parameters a and b in Table 3 were selected at a meeting held in December 2015. Back then, it was proposed to hold on to the values that are more commonly used in slope stability assessments in the Netherlands, i.e. $a=0.033$ ($=1/30$) and $b=50m$.³ This was expected to be somewhat conservative, but little was known at the time about the seismic stability of the Eemshaven-Delfzijl levees. It was therefore proposed to revisit the length effect when the results of the first seismic stability assessments would come available (Figure 24). This action item could be viewed as a follow-up on the abovementioned proposal. It draws upon the results of the LPI-screening (Deltares 2017) and the FORM-analyses presented in chapter Figure 24 to re-evaluate the length effect.

³ The value $a=0.033$ stems from an old study for the Alblasserwaard (one of the Dutch major levee systems) in which 10% of the levee system was found to be sensitive to slope instability. This value of 10% was divided in 3 following discussions over the effects of spatial correlations. The value has found its way into Dutch guidelines and is now widely used in slope stability assessments. The background of $b=50m$ will be discussed in section 7.4. It rests on probabilistic analyses and is in line with the lengths of slope failures.

<p>Aanwezig: Ton Vrouwenvelder (TNO), Ruben Jongejan (RMC), Matthijs Kok (TUD/HKV), Han Vrijling (Horvat), Ed Calle (Deltares), Marcel Visschedijk (Deltares, namens Noorderzijlvest), Bert de Wolff (namens Noorderzijlvest), Sjoerd de Wit (NAM), Geeralt van den Ham (notulist), Vincent Mures (NCG), Ate Wijnstra (Noorderzijlvest)</p>	(page 1)
<p><i>Met welk lengte-effect moet worden gerekend voor macrostabiliteit en hoogte, bij het bepalen van de maximaal toelaatbare faalkans in een doorsnede?</i></p> <p>De correlatielengte voor aardbevingsbelasting is kleiner dan voor waterstandsbelasting en de invloedsfactor van de aardbevingsbelasting groter (0.9). Gegeven bovenstaande wordt voorgesteld om bij macrostabiliteit vast te houden aan de vertaling van eis per traject naar eis per doorsnede voor de situatie zonder aardbeving (conform OI2014, met a=0.033 en b=50 m). Dit lijkt enigszins conservatief, maar de gegevens ontbreken voor een betere inschatting en verwacht wordt dat het effect gering zal zijn.</p>	(page 3)
<p>- Voorgesteld wordt een nieuwe sessie te plannen zodra ontwerpprotocol D-E klaar is, met nieuwe verdeling pga (versie 2) en daarop gebaseerde nieuwe $\alpha_{\text{aardbeving}}$. Ook als de eerste ontwerpervaringen zijn opgedaan, is het verstandig om nog een keer samen te komen omdat dan de consequenties van keuzes beter bekend zullen zijn.</p>	(page 7)

Figure 24. Quotes from the minutes of the meeting of December 2015 on the length effect (in Dutch).

7.3 Characterizing the length effect: the parameter a

The parameter a is defined as the fraction of the total length of the segment that dominates the probability of failure of a segment for the failure mechanism under consideration. Based on an LPI-screening for 11.5 km, 3 to 5 profiles have been selected for a detailed assessment to be able to give conclusions concerning the reliability of the entire stretch (Deltares 2017). These profiles are representative for a combined length of several hundred meters. Because of e.g. variations in stratigraphy, these four profiles are also unlikely to have identical failure probabilities. Considering this, there seems to be no obvious reason to move away from a=0.033.

7.4 Characterizing the length effect: the parameter b

7.4.1 Theory

The following theory forms the basis of the b=50m mentioned in section 7.2 that underlies the cross-sectional reliability requirements for slope stability assessments in the Netherlands (Calle & Barends 1990; Vrouwenvelder & Calle 2003). A levee could be thought of as a series system of statistically homogenous lengths. The failure probability of such a statistically homogeneous length L_{hom} can be approximated by (see e.g. Jongejan 2012 for a derivation):

$$P(F_{L_{\text{hom}}}) = 1 - (1 - P(F_{\text{cross}})) \cdot \exp(-L_{\text{hom}} / (2\pi) * \sqrt{-d^2 p_z(0) / d\Delta^2}) \cdot \exp(-\beta_{\text{cross}}^2 / 2) \quad (21)$$

Where:

$P(F_{L_{\text{hom}}})$ Failure probability of a statistically homogeneous length (per year)

$P(F_{\text{cross}})$ Cross-sectional probability of failure (per year)

β_{cross} Cross-sectional reliability index (-)

The statistically homogenous length (L_{hom}) could be thought of, approximately, as a series system of independent, characteristics lengths (b):

$$b = P(F_{\text{cross}}) \cdot 2\pi / \sqrt{-d^2 p_z(0) / d\Delta^2} \cdot \exp(\beta_{\text{cross}}^2 / 2) \quad (22)$$

which may be approximated as follows if β_{cross} , is positive and not very small, e.g. $\beta_{\text{cross}} > 2$ (Vrouwenvelder 2006):

$$b = \sqrt{2\pi} / (\sqrt{-d^2\rho_z(0)/d\Delta^2}) \cdot \beta_{\text{cross}} \quad (23)$$

The autocorrelation function of the limit state function can be approximated by the weighted sum of the autocorrelation functions for capacity and demand, with their weights being the squared influence coefficients:

$$\rho_z(\Delta) = \sum \alpha_x^2 \rho_x(\Delta) \quad (24)$$

Where

$\rho_z(\Delta)$ Value of the autocorrelation function of the limit state function, evaluated at lag Δ (-)

$\rho_x(\Delta)$ Value of the autocorrelation function of stochastic variable X, evaluated at lag Δ (-)

The different stochastic variables have different autocorrelation functions. The type of autocorrelation function that is widely used in stability analyses in the Netherlands has the following function form (Van Balen et al. 2016):

$$\rho_x(\Delta) = (1-\rho_0) \cdot \exp(-(\Delta/k)^2) + \rho_0 \quad (25)$$

Where:

ρ_0 Lower bound of the autocorrelation function (-)

k Spatial correlation length parameter (m)

Δ Distance/lag (m)

Examples of autocorrelation functions are given in Figure 25. A lower limit of the autocorrelation function greater than zero implies that part of the uncertainty related to a variable is (spatially correlated) epistemic uncertainty.

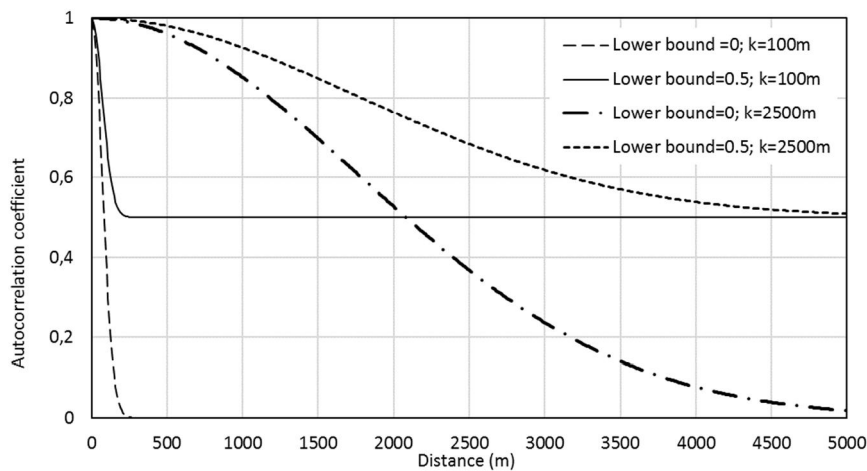


Figure 25. Examples of autocorrelation functions.

7.4.2 Sensitivity analyses

To inform a decision concerning the length effect, various sensitivity analyses have been performed. To simplify these analyses, the various stochastic variables from Table 1 have been grouped/combined into a stochastic variable that is strongly spatially correlated (named “demand” hereafter) and one that is not (named “capacity”). Treating the underlying variables separately does not change the results as long as each of these variables has the same autocorrelation function, see equation (24).

Not all variables are equally spatially variable. The ground motion, for instance, is strongly spatially correlated. The cyclic resistance ratio for layered deposits, on the other hand, is relatively weakly spatially correlated⁴. The influence coefficient from the FORM-analyses has been used as a reference for the influence coefficient of capacity, i.e. $\alpha_c^2 \approx 0.06$. The influence coefficient of capacity has also been increased to show the influence of e.g. treating the uncertainty related to $\varepsilon_{su/p'}$ as equally spatially variable as the uncertainty related to the CRR in layered deposits (doing so would lead to $\alpha_c^2 \approx 0.08$; a higher value of 0.1 has been used instead). Similarly, it has been decreased ($\alpha_c^2 \approx 0.2$), which could be a reasonable approximation for cases without layered deposits. This is because the CRR for sand is based on an empirical relationship that rests on back-calculations of case histories (see also section 7.4.3). The influence coefficient for demand has been calculated by adding the squared influence coefficients of the remaining stochastic variables.

The results of the sensitivity analyses are shown in Table 4. The reported b-values stem from equation (22).

Table 4. Sensitivity analyses related to the length effect.

Case no.	β_{cross}	Capacity			Demand			b (m)
		α_c^2	$\rho_{0,c}$	k_c (m)	α_D^2	$\rho_{0,D}$	k_D (m)	
1	3	0,06	0,5	100	0,94	0	5000	310
2	4	0,06	0,5	100	0,94	0	5000	240
3	4	0,06	0,5	100	0,94	1	-	242
4	4	0,06	0,5	100	0,94	0	5000	240
5	4	0,06	0	150	0,94	0	5000	255
6	4	0,06	0,5	150	0,94	0	5000	357
7	4	0,1	0,5	100	0,9	0	5000	187
8	4	0,02	0,5	150	0,98	0	5000	600
9	4	0,5	0	100	0,5	1	-	59
10	4	0,5	0,5	100	0,5	1	-	84
11	4	0,5	0	150	0,5	1	-	89

Table 4 illustrates the following:

1. As shown by cases 1 and 2, the length effect increases with increasing reliability indices (as it should). A reliability index of 4 is close to the target reliability (slightly conservative). This is why this reliability index has been considered in the remaining case studies.
2. As shown by cases 2 and 3, the precise autocorrelation function for demand is largely irrelevant to the length effect, as long as this variable is much more strongly spatially correlated than capacity. The length effect is most strongly influenced by (1) the relative importance of the uncertainty related to capacity and (2) the autocorrelation function of capacity.
3. As shown by cases 3, 4 and 5, the length-effect depends on the autocorrelation function of the most weakly spatially correlated variables.
4. As shown by cases 6 and 7, the length effect increases (i.e. b decreases) when the relative importance of the uncertainty related to the spatially variable stochastic variables increases (i.e. α_c^2 increases, α_D^2 decreases).
5. As shown by cases 7 and 8, the length effect decreases (i.e. b increases) when the relative importance of the uncertainty related to the strongly spatially correlated stochastic variables increases (e.i. α_D^2 increases, α_c^2 decreases).
6. Cases 9 to 11 (bottom rows) show that the same procedure leads to b=50m-100m for inputs that are more common in slope stability assessments with a dominant hydraulic load (no earthquake). These analyses illustrate why b=50m is used as a basis for cross-sectional stability assessments in the WBI (the WBI is the instrument provided by the Minister for safety assessments).

The b-values in Table 4 for seismic stability are high compared to the b-value of 50m that underlies the Dutch technical guidelines for slope stability assessments (TAW 2001). This stems from the fact that the uncertainties related to strongly spatially variable stochastic variables are more important in seismic stability analyses than in high water stability analyses, making the limit state function fluctuate more slowly along the length of the dike.

⁴ The CRR referred to here concerns a local average, see also Appendix G. Correlation distances for point values are considerably shorter.

7.4.3 Comparison with earthquake damage observations to embankments

Abstract

To verify whether the use of b-values of 200m to 350 m rather than 50m is justified for deriving cross-sectional reliability requirements for seismic stability assessments, the calculated b-values have been compared to damage observations from Japan and related academic research into spatial correlations. These comparisons show that embankment failures can indeed lead to significant damages that extend over hundreds of meters. The comparisons point to even higher b-values than those shown in Table 4. The conditions underlying the Japanese case histories and the conditions in Groningen differ markedly however. Hence, while the b-values in Table 4 still appear low in the light of damage observations, the use of higher values purely on the basis of damage observations is not considered prudent.

Interpreting independent, equivalent length as expected failure lengths

An independent equivalent length is often interpreted as the expected length of failures. This may not be correct, however, when the distributions of stochastic variables rest on back-analyses of case histories. Length effects are inherent to historical observations. When, for instance, liquefaction was not observed in a particular earthquake, it was not observed *anywhere* in the affected region. When distributions rest on back-calculations of case histories, the computed b-value should be interpreted as the length in which a levee is expected to fail somewhere (with a particular probability). In such cases, the computed b-value should be greater than the expected length of failures.

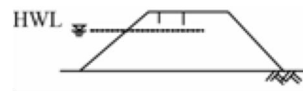
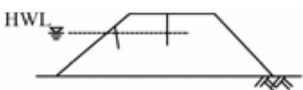

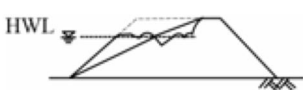
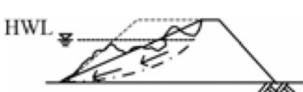
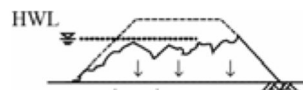
The distribution of the cyclic resistance ratio of sand deposits rests on an empirical relationship that originates from back-analyses of case histories. Hence, for Eemshaven, where sand deposits are critical, the computed b-value should be greater than the expected length of failures. This is different for Delfzijl. Here, laminated deposits are critical. The distribution of the cyclic resistance ratio of laminated deposits rests on laboratory tests, not back-analyses. Hence, at Delfzijl, the computed b-values should be interpretable as the expected lengths of slope failures.

The independent, equivalent length and damage observations

Sasaki and Tamura (2007) present an overview of earthquake damages to embankments in Japan from 1993 onwards (the original reports are in Japanese). Data from their publication has been summarized in Table 5 below.

The average damaged lengths in Table 5 have been calculated by dividing the total damaged lengths by the number of places where damages occurred. The severity of the damages associated with the total damaged lengths is often unclear. This is unfortunate since the length of damage depends on the (definition of the) damage state (see also Kwak et al. 2016). The average length of total collapse caused by liquefaction of the foundation in the Niigata-ken earthquake, which seems to be closest to the failure mechanism considered here, is 957 m. This clearly shows that liquefaction can lead to significant damage over considerable distances. Without accounting for the type/severity of damage, the average damaged lengths range from 317m to 1,732m.

Table 5. Overview of damages reported by Sasaki and Tamura (2007). Figures and quotes from Table 1 and Figure 2 in Sasaki and Tamura (2007).

Year	Earthquake	Severity of damage	Total damaged length (m)	No. of damaged stretches	Average damage length (m)
1993	Kushiro-oki (M=7.8)	Not clearly described (“liquefaction inside embankments, 3-d response of dike”); Kushiro river	10,100	28	361
		Not clearly described (“liquefaction inside embankments, 3-d response of dike”); Tokachi river	9,200	20	460
1993	Hokkaido Nansei-oki (M=7.8)	Not clearly described (“crest cave-in along diagonal slip plane”)	6,600	18	367
1995	Hyogo-ken Nanbu (M=7.2)	Not clearly described (“separation into blocks, submerged into liquefied subsoil layer”)	5,700	18	317
2000	Tottori-ken Seibu (M=7.3)	Not clearly described (“Bend of dike bottom, transverse cracks at a curvilinear part”)	20,700	32	647
2003	Miyagi-ken Hokubu (M=6.4)	Not clearly described (“flow-like deformation”)	Not available	66	Not available
2003	Tokachi-oki (M=8.0)	Not clearly described (“elongation of sluice gate length”)	16,000	26	615
2004	Niigata-ken Chuetsu (M=6.8)	“Longitudinal cracks (shallower than H.W.L.)” 	6,997	8	875
		“Longitudinal cracks (deeper than H.W.L.)” 	449	1	449
		“Transverse cracks (shallower than H.W.L.)” 	-	-	-
		“Transverse cracks (deeper than H.W.L.)” 	-	-	-
		“Slide of slope (failure of crest)” 	8,659	5	1,732
		“Total collapse of crest, no original shape remaining (liquefaction of foundation)” 	2,871	3	957

More details on the damages caused by the 1995 Hyogoken-Nanbu earthquake can be found in Matsuo (1996). According to Matsuo (1996), the Torishima dike along the Yodo-gawa was strongly impacted by the earthquake. A continuous crest settlements of 2-3 meters was observed over a distance of about 1.4 kilometers see Figure 26. This amount of crest settlement is broadly in line with the definition of the limit state considered here.

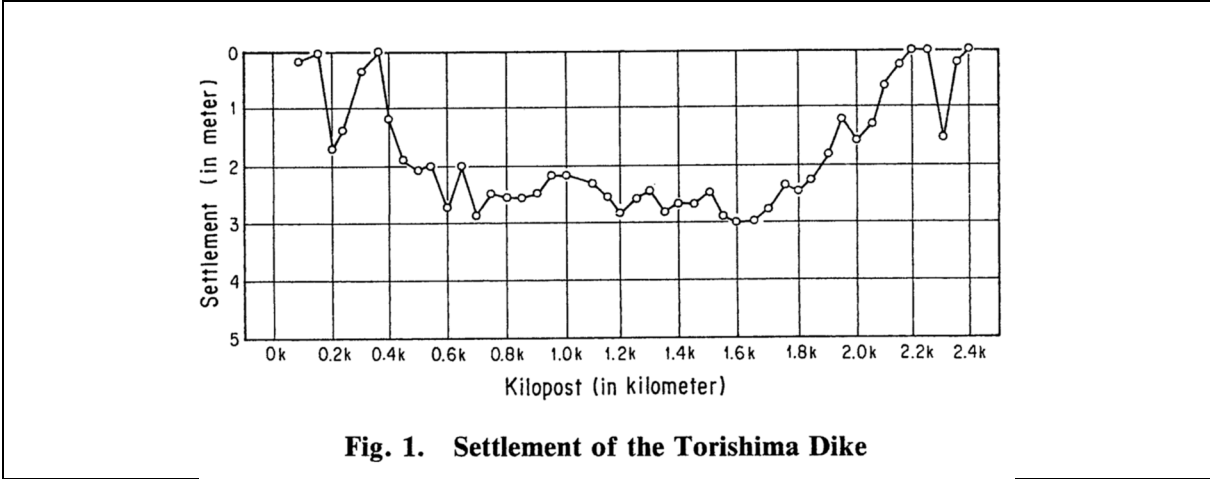


Figure 26. Damages caused by the 1995 Hyogoken-Nanbu earthquake and a profile of observed crest settlement of the Torishima dike along the Yodo-gawa (from: Matsuo 1996).

The Japanese damage records indicate that liquefaction can lead to significant damage or collapse over lengths of a kilometer or more. It also appears that damages, irrespective of their severity, can easily extend over hundreds of meters. All average damage lengths in Table 5 far exceed 50m.

Damage observations and empirical autocorrelation functions

Observed damage lengths are influenced by the difference between capacity and demand: when design loads are strongly exceeded, damaged lengths are likely to much higher than when design loads are barely or not at all exceeded. To correct for this effect, back-analyses of the spatial pattern of damage states were performed by Kwak et al. (2016) conditional on the seismic demands that led to these damages. Two different fragility curves were used in these back-analyses, conditional on ground water level. Empirical autocorrelations functions of capacity were derived from the damages observed in the 2004 Niigata-ken Chuetsu earthquake and the 2007 Niigata-ken Chuetsu-oki earthquakes.

The squared exponential autocorrelation functions for capacity and demand from Kwak et al. (forthcoming) are considered here. Using the distribution of capacity and the distribution of demand conditional on the M6.6 event, α_c^2 is around 0.75. Results of sensitivity analyses with these autocorrelation functions are shown in Table 6.

Table 6. The calculated b-values for a M=6.4 earthquake using the empirical autocorrelation function developed by Kwak et al. (2016).

Case no.	β_{cross}	Capacity			Demand			b (m)
		α^2	ρ_0	k (m)	α^2	ρ_0	k (m)	
1	3	0,75	0	2765	0,25	0	8000	1869
2	4	0,75	0	2765	0,25	0	8000	1402

The results shown in Table 6 are in reasonable agreement with the damage reports from Table 4: the b-values are broadly in line with the average length of severe damage/collapse.

The empirical autocorrelation function of capacity developed by Kwak et al. (2016) is a property of the capacity the levee system for which it has been derived. The autocorrelation function of demand could be different from earthquake to earthquake. Using the (modified) autocorrelation function for capacity by Kwak et al. (2016), the b-values have been recalculated for several cases from Table 4. Results are shown in Table 7.

Table 7. Sensitivity analysis using an empirical autocorrelation function developed by Kwak et al. (2016).

Case no.	β_{cross}	Capacity			Demand			b (m)
		α^2	ρ_0	k (m)	α^2	ρ_0	k (m)	
1	4	0,08	0	2765	0,92	0	5000	1780
2	4	0,1	0	2765	0,9	0	5000	1780
3	4	0,02	0	2765	0,98	0	5000	1990

The b-values from Table 7 are significantly greater than the ones from Table 4. This could be because the results shown in Table 4 are conservative. It could also be, however, that the variations in the reliability of the Japanese levee systems were underestimated in the back analyses with the use of only two different fragility curves. The empirical autocorrelation function then describes the combined effect of:

1. changes in the reliability of cross-sections along the entire length of levee due (not fully accounted for by the two fragility curves) and
2. variations in material properties within homogenous lengths.

If so, the empirical autocorrelation function should be used in combination with a relatively high a-value in equation (20), i.e. $a > 0.033$. After all, if the two fragility curves underestimate the variations in cross-sectional reliabilities, there could still be important variations within the "critical length" ($= a \cdot L$). Note that $a=0.033$ in combination with the b-values from Table 4 (about 200-400m) leads to broadly similar cross-sectional reliability requirements to $a=0.3$ with the b-values from Table 7. Taking the empirical autocorrelation by Kwak et al. (forthcoming) in combination with $a=0.033$ would lead to target failure probabilities that are about a factor 10 greater. This would translate into a significant reduction of return periods (amongst other). Given that this research is relatively recent and has not been previously applied in projects, such a reduction in demand is not considered prudent for an assessment of a critical infrastructure like the Eemshaven-Delfzijl sea dike.

Discussion

While it is difficult to base a decision on a particular b-value purely on Japanese damage records, these records do suggest that embankment failures can extend over hundreds of meters. It also seems that $b=200-350\text{m}$ is more realistic than $b=50\text{m}$.

It is important to note that the earthquakes covered by Sasaki and Tamura (2007), Matsuo (1996) and Kwak et al. (2016) had considerably greater magnitudes ($M > 6$) than the maximum magnitude of around 5 expected in Groningen (NAM 2016). Also, soil conditions and levee designs differ in Groningen and Japan. This means that damage observations from Japan may not be entirely representative for Groningen. This is also why damage observations have been used to put the results of the "bottom-up" sensitivity analyses (Table 4) into perspective rather than the other way round.

7.4.4 Proposed b-value

Based on the results of the sensitivity analyses in Table 4 and the discussion above, a b-value of 200-350 m seems justified. The use of the lowest value from this range is proposed, i.e. $b=200\text{m}$. Should this still turn out to be too optimistic, the assumed 3 month repair time seems too pessimistic. This is because this month repair rests on the premise that earthquake damages may occur over several kilometers (Figure 24).

Schade zal wellicht optreden over enkele km's. Noodreparatie
 kan ook bestaan uit alleen herstellen bekleding buitentalud. Groot deel dijk heeft kleikern
 aan buitenzijde. Een hersteltijd van 1 jaar wordt als lang beoordeeld: noodreparatie moet
 sneller kunnen. Een hersteltijd van 3 maanden is aannemelijker. (page 7)

Figure 27. Quotes from the minutes of the meeting of December 2015 on the length effect (in Dutch).

A repair time shorter than 3 months leads to a smaller probability of flooding in case of significant earthquake damage (i.e. $P_{F|D} < 1/10$). Taken together, $b=200\text{m}$ and $P_{F|D}=1/10$ seem to be a prudent basis for cross-sectional seismic stability assessments of the Eemshaven-Delfzijl sea dikes.

7.5 Updated cross-sectional target reliabilities

The following parameter values are proposed to characterize the length effect:

1. $a = 0.033$ (same as before)
2. $b = 200\text{m}$ (before: 50m)

The impact of increasing the b-value from 50 to 200m leads to changes in the cross-sectional target reliabilities for segments 6-6 and 6-7, as shown in Table 8.

Table 8. Updated cross-sectional target reliabilities for assessing seismic stability.

Segment	Standard of protection (per year)	Cross-sectional target reliability for $a=0.033$ and $b=50\text{m}$ (original, see Table 3)		Cross-sectional target reliability for $a=0.033$ and $b=200\text{m}$ (proposed)	
		P_T	β_T	P_T	β_T
6_6 (includes Eemshaven)	1/1,000	7.64-05	3.79	2.79E-04	3.45
6_7 (includes Delfzijl)	1/3,000	3.02-05	4.01	1.09E-04	3.70

The changes in cross-sectional target reliabilities lead to a reduction of the return periods of the design values of the spectral accelerations at NSUB by about a factor 3, see also chapter 8. The changes also affect the design values of the other stochastic variables, albeit to a lesser extent. This is because their influence coefficients are relatively small.

8 Action item 5: Synthesis

8.1 From calculated FORM-influence coefficients and target reliabilities to design values

Design values have been derived on the basis of:

1. the influence coefficients obtained from FORM-analyses with the FE-model and
2. the target reliabilities from Table 8 in section 7.5, i.e. $\beta_T = 3.45$ (segment 6-6, Eemshaven) and $\beta_T = 3.70$ (segment 6-7, Delfzijl).

Table 9 and Table 10 show the cumulative probabilities of the design values that seem reasonable on the basis of the calculated FORM-influence coefficients and target reliabilities. As discussed in chapter 2, a design value can be split into a representative value and a partial factor (last two columns).

The design values in Table 9 and Table 10 all rest on influence coefficients that are greater than those obtained from FORM-analyses. The sum of squared influence coefficients on which the design values are based is an indicator of the amount of conservatism in the semi-probabilistic rule. For Eemshaven and Delfzijl, these sums are about 1.1. Recommended design values, based on Table 9 and Table 10, are shown in Table 11.

Table 9. From calculated influence coefficients and target reliability to design values. Results for the Eemshaven base case (segment 6-6).

Stochastic variable	Calculated		Possible basis for assessment					
	α^2	α	α^2	α	β_T	Cumulative probability	Representative value, quantile	Partial factor
Spectral acceleration at model base	0.732	-0.856	-	-	-	-	-	-
Spectral acceleration at NSUB	0.725	-0.851	0.81	-0.9	3.45	9.991E-01 per year	1056 year return period	1.0
Uncertainty in site response	0.007	-0.086	0.01	-0.1	3.45	0.635	50%	1.04
CRRM=7.5 in sand deposits	0.160	0.400	0.18	0.42	3.45	0.074	15%	1.09
Uncertainty related to residual strength*	0.040	0.200	0.04	0.21	3.45	0.234	50%	1.39
Model Uncertainty	0.068	0.261	0.08	0.28	3.45	0.167	50%	1.70
Total	1	-	1.12	-	-	-	-	-

* For residual strengths according to Kramer and Wang (2015).

Table 10. From calculated influence coefficients and target reliability to design values. Results for the Delfzijl base case (segment 6-7).

Stochastic variable	Calculated		Possible basis for assessment					
	α^2	α	α^2	α	β_T	Cumulative probability	Representative value, quantile	Partial factor
Spectral acceleration at model base	0.786	-0.887	-	-	-	-	-	-
Spectral acceleration at NSUB	0.778	-0.882	0.81	-0.9	3.70	9.996E-01 per year	2290 year return period	-

Uncertainty in site response	0.008	-0.089	0.01	-0.1	3.70	0.644	50%	1.04
CRR _{M=5.0} of laminated deposit	0.046	0.214	0.09	0.3	3.70	0.133	15%	1.01
Uncertainty related to residual strength*	0.018	0.134	0.03	0.16	3.70	0.277	50%	1.31
Model Uncertainty	0.150	0.387	0.17	0.41	3.70	0.070	50%	2.30
Total	1	-	1.10	-	-	-	-	-

* For residual strengths according to Kramer and Wang (2015).

Recommended design values

The following design values are recommended for use with the Guideline for conducting dynamic effective stress analyses (Fugro 2016b).

Table 11. Recommended design values.

Stochastic variable	Representative value	Partial factor segment 6-6	Partial factor segment 6-7
Spectral acceleration at NSUB	Segment 6-6: 1100 year return period Segment 6-7: 2300 year return period	1.0	1.0
Uncertainty in site response	Median, i.e. time history amplitudes at model base, calculated on the basis of median properties ("best estimate")	1.05	1.05
CRR in sand deposits	16% quantile value of the CRR _{M=7.5} from the probabilistic Boulanger & Idriss (2014) relationship for the median of local q_{c1Ncs} -values Put differently: the CRR _{M=7.5} according to the "deterministic" relationship proposed by Boulanger & Idriss (2014) for the median of local q_{c1Ncs} -values.	1.10*	1.10
CRR in laminated deposits	16% quantile of the distribution of the spatial average at four cycles (regional data set)	1.0	1.0
Uncertainty related to residual strength in sand deposits **	Median, i.e. $(\epsilon_{lnSu/p'})_{rep} = 1$	1.4 on $(S_u/p')_{rep}$, see equation (26)	1.4 on $(S_u/p')_{rep}$, see equation (26)
Uncertainty related to residual strength in laminated deposits **	Median, i.e. $(\epsilon_{lnSu/p'})_{rep} = 1$	1.3 on $(S_u/p')_{rep}$, see equation (26)	1.3 on $(S_u/p')_{rep}$, see equation (26)
Model Uncertainty	Median, i.e. the computed crest settlement from an unbiased model	1.7	2.3

* This is broadly equivalent to the use of a 25% quantile of q_{c1Ncs} together with the deterministic Boulanger & Idriss (2014) relationship between q_{c1Ncs} and CRR, which is more conservative than the 33% quantile proposed by Boulanger & Montgomery (2016) for cases like these where the dimensions of relevant deformations far exceed the scale of fluctuation.

** For residual strengths according to Kramer and Wang (2015).

The design value of residual strength can be calculated using:

$$\left(\frac{Su}{p'}\right)_d = \frac{\exp(-8.444 + 0.109 (N_1)_{60} + 5.379 p'^{0.1})}{\gamma_{res} p'} \quad (26)$$

with $\gamma_{res}=1.4$ (sand deposit) or $\gamma_{res}=1.3$ (laminated deposit) and $(N_1)_{60}$ according to Idriss & Boulanger (2008):

$$(N_1)_{60} = 46 \cdot (0.478 q_{c1N}^{0.264} - 1.063)^2 \quad (27)$$

where:

- $(Su/p')_d$ Design value of normalized residual strength (-)
- p' Initial effective vertical stress (atm)
- $(N_1)_{60}$ Normalized SPT blow count (-), median value
- q_{c1N} Normalized cone tip resistance (-)

8.2 Uncertainty related to motions

The following procedure is recommended for dealing with the uncertainty related to motions (see also Appendix H):

1. Select 11 independent motions with appropriate seismological characteristics (e.g. amplitude, frequency content and duration).
2. Compute crest settlements for each motion using the design values from Table 11.
3. Analyze the results: outliers should be understood.
4. The (subjective) probability that the crest settlement for a randomly selected motion exceeds the limit state should be less than 25%. If, for instance, all 11 motions are considered to be equally likely, the limit state should not be exceeded for more than 2 motions.

Note that it might be incorrect to treat the 11 motions as equally likely or to assume that the 11 selected motions span the entire set of possible motions. In some cases, it might be reasonable to assign low subjective probabilities to particular motions or to treat the 11 motions as members of a subset of relatively pessimistic motions.

8.3 Uncertainty related to stratigraphy

The uncertainty related to stratigraphy can be dealt with as follows:

1. consider a conservative, realistic stratigraphy,
2. carry out sensitivity analyses,
3. make an informed judgment.

A more rigorous procedure for dealing with uncertainty related to stratigraphy is given by ENW (2012). It is summarized in Appendix H (for motions, not stratigraphies). This procedure is laborious, however, since it involves a large number of evaluations of the limit state function.

8.4 Sea level (load combination)

The combination of a severe earthquake and an extremely high or low sea level is unlikely because water levels and earthquakes are uncorrelated and because both types of events have relatively short durations. Note that a higher water level on the sea side need not be conservative. It is recommended to use as a design sea level, whichever of the following is the most conservative:

1. the water level that is expected to be exceeded once a year (1 year return period) or
2. the low tide.

References

- Van Balen, W. et al., 2016. *Hydra-Ring 2.0, Probabilistics toolbox for the WTI2017, Technical Reference Manual*, Deltares, report no. 1230088-DSC-0072.
- Bazzurro & Cornell, 2004. Nonlinear Soil-Site Effects in Probabilistic Seismic-Hazard Analysis. *Bulletin of the Seismological Society of America*, 94(6), pp.2110–2123.
- Bommer, J.J. et al., 2015. *Development of Version 2 GMPEs for Response Spectral Accelerations and Significant Durations from Induced Earthquakes in the Groningen Field* November 2. J. Van Elk & D. Doornhof, eds., NAM.
- Boulanger, R.W. & Idriss, I.M., 2014. *CPT and SPT based liquefaction triggering procedures*, Report No. UCD/CGM-14/01, Center for Geotechnical Modeling, Department of Civil & Environmental Engineering, College of Engineering, University of California at Davis.
- Boulanger, R.W. & Montgomery, J., 2016. Nonlinear deformation analyses of an embankment dam on a spatially variable liquefiable deposit. *Soil Dynamics and Earthquake Engineering*, 91, pp.222–233. Available at: <http://linkinghub.elsevier.com/retrieve/pii/S026772611630104X>.
- Boulanger, R.W. & Montgomery, J., 2015. Nonlinear Deformation Analyses of an Embankment Dam on a Spatially Variable Liquefiable Deposit. In *6th International Conference on Earthquake Geotechnical Engineering*. Christchurch, New Zealand.
- Calle, E.O.F., 2007. Statistiek bij Regionale Proevenverzamelingen deel 1. *Geotechniek*, July.
- Calle, E.O.F., 2008. Statistiek bij Regionale Proevenverzamelingen deel 2. *Geotechniek*, Januari.
- Calle, E.O.F. & Barends, F.B.J., 1990. *PROSTAB een computerprogramma voor probabilistische analyse van stabiliteit van taluds*, Grondmechanica Delft, CO-266484/32.
- Deltares, 2017. *LPI screening for the Eemshaven-Delfzijl levee*, Deltares report no. 1220173-024-GEO-0067, version 3.
- ENW, 2012. *Technisch Rapport Grondmechanisch Schematiseren bij Dijken*, Expertisenetwerk Waterveiligheid.
- Expert Panel, 2016. *Expert Panel Report*, 2 December 2016. Letter addressed to E. van Dijk by Chacko, J. Green, R.A. Kramer, S.L. Towhata, I.
- Fugro, 2016a. *Evaluation of dynamic stability Eemshaven-Delfzijl levee, The Netherlands*, Fugro, 2 December 2016, contract no. 1016-0459-000.
- Fugro, 2016b. *Guidelines for dynamic effective stress finite element analyses Eemshaven-Delfzijl levee Groningen, the Netherlands*, Fugro, 10 August 2016, 1st issue, Contract No. 1016-0459-000.
- Fugro, 2016c. *Interpretive report, Delfzijl / Eemshaven Levee Project in Groningen, the Netherlands, prepared for Nederlandse Aardolie Maatschappij B.V.* November.,
- Green, R. et al., 2016. *Unbiased Cyclic Resistance Ratio Relationships for Evaluating Liquefaction Potential in Groningen*,
- Idriss, I.M. & Boulanger, R.W., 2008. *Soil liquefaction during earthquakes*, EERI monograph MNO-12, Earthquake Engineering Research Institute.
- Itasca, 2011. *Fast Lagrangian Analysis of Continua (FLAC2D)*, Version 6.0.
- Jongejan, R.B., 2012. *Het lengte-effect in een statistisch homogeen vak*, Memorandum, 11 February 2012, Jongejan RMC.
- Jongejan, R.B. & Maaskant, B., 2015. Quantifying Flood Risks in the Netherlands. *Risk Analysis*, 35(2), pp.252–264. Available at: <http://doi.wiley.com/10.1111/risa.12285>.
- Kramer, S.L. & Wang, C.-H., 2015. Empirical Model for Estimation of the Residual Strength of Liquefied Soil. *Journal of Geotechnical and Geoenvironmental Engineering*, 141(9), p.4015038. Available at: <http://ascelibrary.org/doi/10.1061/%28ASCE%29GT.1943-5606.0001317>.
- Kwak, D.Y. et al., Methods for Probabilistic Seismic Levee System Reliability Analysis. In *Georisk 2017*.
- Kwak, D.Y. et al., 2016. Seismic Levee System Fragility Considering Spatial Correlation of Demands and Component Fragilities. *Earthquake Spectra*, 32(4), pp.2207–2228. Available at: <http://earthquakespectra.org/doi/10.1193/083115EQS132M>.
- Matsuo, O., 1996. Damage to river dikes. *Soils and Foundations*, (Special issue, January 1996), pp.235–240.
- Montgomery, J., 2015. *Issues in nonlinear deformation analysis of embankment dams affected by liquefaction*. University of California, Davis.
- NAM, 2016. Toelichting resultaten Mmax-workshop.
- Robertson, P.K., 1990. Soil classification using the cone penetration test. *Canadian Geotechnical Journal*, 27(1), pp.151–58.

- Sasaki, Y. & Tamura, K., 2007. Failure mode of embankments due to recent earthquakes in Japan. In *4th International Conference on Earthquake Geotechnical Engineering, June 25-28, 2007*. Thessaloniki, Greece: Paper No.1479.
- Stewart, J., Afshari, K. & Hashash, Y.M., 2014. *Guidelines for Performing Hazard-Consistent One-Dimensional Ground Response Analysis for Ground Motion*, Pacific Earthquake Engineering Research Center.
- TAW, 1989. *Leidraad voor het ontwerpen van rivierdijken deel 2 benedenrivierengebied*, Technische Adviescommissie voor de Waterkeringen.
- TAW, 2001. *Technisch Rapport Waterkerende Grondconstructies; Geotechnische aspecten van dijken, dammen en boezemkaden*, Technische Adviescommissie voor de Waterkeringen.
- USACE, 2013. *Engineering and design of I-Walls*, Washington, DC.
- Vanmarcke, E., 2011. Risk of Limit-Equilibrium Failure of Long Earth Slopes: How It Depends on Length. In *Georisk 2011*. Reston, VA: American Society of Civil Engineers, pp. 1–24.
- VanMarcke, E., 1977. Reliability of Earth Slopes. *Journal of the Geotechnical Engineering Division*, 103(11), pp.1247–1265.
- Vrouwenvelder, T., 2006. Spatial effects in reliability analysis of flood protection systems. In *Second IFED Forum*. Lake Louise, Canada.
- Vrouwenvelder, T. & Calle, E., 2003. Measuring Spatial Correlation of Soil Properties. *Heron*, 48(4).

Appendix A First Order Reliability Method (FORM)

FORM is an efficient, approximate technique for computing probabilities of failure. In this appendix, a brief overview is given of the steps in a FORM analysis, together with an example.

FORM step by step

FORM is an iterative procedure that requires only few evaluations of a limit state function compared to e.g. Monte Carlo simulation. FORM calculation involves the following steps:

Step 1: Select start values

Select values for the stochastic variables for the evaluation of the limit state function (Z). Note: $Z < 0$ implies failure, $Z > 0$ implies the opposite.

Step 2: Calculate partial derivatives

Calculate the partial derivatives of the limit state function with respect to the different stochastic variables. This can be done by perturbing input values or by looking at the results of sensitivity analyses that have already been carried out.

Step 3: Transform all non-normally distributed variables to normally distributed variables.

This can be done on the basis of the following equations:

$$\sigma_{X_{norm,i}} = \varphi\{ \Phi^{-1}(F_{X,i}(X_{i,0})) \} / f_{X,i}(X_{i,0}) \quad (28)$$

$$\mu_{X_{norm,i}} = X_{i,0} - \Phi^{-1}(F_{X,i}(X_{i,0})) \cdot \sigma_{X_{norm,i}} \quad (29)$$

Where:

$\sigma_{X_{norm,i}}$ Standard deviation

$\mu_{X_{norm,i}}$ Expected value

$\varphi(\cdot)$ Standard normal probability density function

$\Phi(\cdot)$ Standard normal distribution function

$F_{X,i}(X_{i,0})$ Cumulative distribution function of variable X_i , evaluated at $X_{i,0}$

$f_{X,i}(X_{i,0})$ Probability density function of variable X_i , evaluated at $X_{i,0}$

To check the end-result, the cumulative probabilities of $F_{X,i}(X_{i,0})$ and $\Phi(\sigma_{X_{norm,i}}/\mu_{X_{norm,i}})$ could be compared. These should be identical. The same should hold true for the probability densities.

Step 4: Calculate the standard deviation and expected value of the (normalized) limit state function

The standard deviation follows from:

$$\sigma_Z = (\sum (\partial Z / \partial X_i \cdot \sigma_{X_{norm,i}})^2)^{1/2} \quad (30)$$

Where:

$\partial Z / \partial X_i$ Partial derivative of the limit state function with respect to stochastic variable X_i , evaluated at $X_{i,0}$.

The expected value follows from:

$$\mu_Z = Z(\underline{X}_0) + \sum \{ \partial Z / \partial X_i \cdot (\mu_{X_{norm,i}} - X_{i,0}) \} \quad (31)$$

Where:

\underline{X}_0 Vector of the start values of all stochastic variables

Step 6: Calculate influence coefficients and reliability index

The influence coefficients follow from the product of the partial derivatives and the standard deviations from step 3.

$$\alpha_{x_i} = (\partial Z / \partial X_i \cdot \sigma_{x_{norm,i}}) / \sigma_Z \quad (32)$$

The reliability index follows from:

$$\beta = \sigma_Z / \mu_Z \quad (33)$$

Step 6: Repeat steps 2-5, starting from the expected design point

The previous steps should be repeated until convergence is obtained. This can be done through successive substitution, i.e. by using the quantile values corresponding to the computed β and α -values as the start values for the next FORM iteration. The resulting reliability index is related to the probability of failure as follows:

$$P(F) = \Phi(-\beta) \quad (34)$$

The accuracy of a FORM computation can be checked by e.g. a Monte Carlo simulation. For a linear limit state function with independent, normally distributed variables, FORM yields the exact same result as MC or numerical integration.

Example

The following code could be run in e.g. Matlab or Octave. It concerns a simple, hypothetical limit state function with two lognormally distributed variables: demand and capacity. Note: the lognormally distributed variables are given here by the normal distributions of their natural logarithms. This is why normalization does not play a role here.

```
function [ Z ] = Z(x1,x2)

Z = exp(x2) - exp(x1);

endfunction
```

```
function [ ] = FORM(n)
% n = Number of FORM iterations, e.g. n=50 (increase until convergence is reached)

fun = "Z";    % here: Z = C - D

%% Distributions of stochastic variables
median_D = 50;    % D = Demand
mu_InD = log(median_D);
sd_InD = 0.4;

median_C = 200;    % C = Capacity
mu_InC = log(median_C);
sd_InC = 0.40;

%% Rename
mu1 = mu_InD;
sd1 = sd_InD;
mu2 = mu_InC;
sd2 = sd_InC;

%% Select start values for FORM iterations
x1(1) = mu1;
x2(1) = mu2;
```

```

%% Select parameter values for FORM iterations
r = 0.8;           % relaxation factor: this factor helps to arrive at the design point in a more gentle manner
dx = 0.001;       % perturbation for computing partial derivatives

%% FORM iterations
for i = 2:n;
    dZ_dx1(i) = ( feval( "Z", x1(i-1)+dx , x2(i-1) ) - feval( "Z", x1(i-1) , x2(i-1)) ) / dx;
    dZ_dx2(i) = ( feval( "Z", x1(i-1) , x2(i-1)+dx ) - feval( "Z", x1(i-1) , x2(i-1)) ) / dx;

    mu_Z(i) = feval(fun,x1(i-1),x2(i-1)) + ( dZ_dx1(i)*(mu1-x1(i-1)) + dZ_dx2(i)*(mu2-x2(i-1)) );

    sd_Z(i) = sqrt( (dZ_dx1(i) * sd1)^2 + (dZ_dx2(i) * sd2)^2 );

    Beta(i) = mu_Z(i)/sd_Z(i);

    a1(i) = - dZ_dx1(i) * sd1 / sd_Z(i);
    a2(i) = - dZ_dx2(i) * sd2 / sd_Z(i);

    x1d(i) = mu1 + a1(i)*Beta(i)*sd1;
    x2d(i) = mu2 + a2(i)*Beta(i)*sd2;

    x1(i) = r*x1(i-1)+(1-r)*x1d(i);
    x2(i) = r*x2(i-1)+(1-r)*x2d(i);
endfor

Beta = Beta(n)
Pf = normcdf(-Beta)

alpha_D = a1(n)
alpha_C = a2(n)

%% Check FORM results
% The limit state function should be equal to zero in the design point:
Z = feval( "Z", x1(n),x2(n))

% The probability of failure can also be computed using Monte Carlo simulation:
Pf_MC = sum( exp(normrnd(mu1,sd1,1e7,1)) > exp(normrnd(mu2,sd2,1e7,1)) ) / 1e7

```

In this case, FORM gives a failure probability of 0.0071. Monte Carlo gives practically the same result. The number of evaluations of the limit state function is several orders of magnitude smaller when using FORM, however.

For normalizing a Weibull distributed variable:

```

pdf_x = wblpdf( x, scale , shape );
cdf_x = wblcdf( x, scale , shape );

sd = normpdf( norminv( cdf_x ) ) / pdf_x;
mu = x - norminv( cdf_x ) * sd;

```

Indices have to be added to the x-values when this piece of code is placed within the FORM-loop shown above.

Appendix B Design point values

An overview of the **cumulative probabilities** of the design point values of capacity variables ($\alpha > 0$) is given below, together with the *exceedance probabilities* of demand variables ($\alpha < 0$), for a range of reliability indices.

α	Reliability index β								
	3	3,2	3,4	3,6	3,8	4	4,2	4,4	4,6
1,00	1,35E-03	6,87E-04	3,37E-04	1,59E-04	7,23E-05	3,17E-05	1,33E-05	5,41E-06	2,11E-06
0,95	2,19E-03	1,18E-03	6,19E-04	3,13E-04	1,53E-04	7,23E-05	3,30E-05	1,46E-05	6,21E-06
0,90	3,47E-03	1,99E-03	1,11E-03	5,98E-04	3,13E-04	1,59E-04	7,84E-05	3,75E-05	1,74E-05
0,85	5,39E-03	3,26E-03	1,93E-03	1,11E-03	6,19E-04	3,37E-04	1,78E-04	9,20E-05	4,61E-05
0,80	8,20E-03	5,23E-03	3,26E-03	1,99E-03	1,18E-03	6,87E-04	3,90E-04	2,16E-04	1,17E-04
0,75	1,22E-02	8,20E-03	5,39E-03	3,47E-03	2,19E-03	1,35E-03	8,16E-04	4,83E-04	2,80E-04
0,70	1,79E-02	1,25E-02	8,66E-03	5,87E-03	3,91E-03	2,56E-03	1,64E-03	1,04E-03	6,41E-04
0,65	2,56E-02	1,88E-02	1,36E-02	9,64E-03	6,76E-03	4,66E-03	3,17E-03	2,12E-03	1,39E-03
0,60	3,59E-02	2,74E-02	2,07E-02	1,54E-02	1,13E-02	8,20E-03	5,87E-03	4,15E-03	2,89E-03
0,55	4,95E-02	3,92E-02	3,07E-02	2,39E-02	1,83E-02	1,39E-02	1,04E-02	7,76E-03	5,70E-03
0,50	6,68E-02	5,48E-02	4,46E-02	3,59E-02	2,87E-02	2,28E-02	1,79E-02	1,39E-02	1,07E-02
0,45	8,85E-02	7,49E-02	6,30E-02	5,26E-02	4,36E-02	3,59E-02	2,94E-02	2,39E-02	1,92E-02
0,40	1,15E-01	1,00E-01	8,69E-02	7,49E-02	6,43E-02	5,48E-02	4,65E-02	3,92E-02	3,29E-02
0,35	1,47E-01	1,31E-01	1,17E-01	1,04E-01	9,18E-02	8,08E-02	7,08E-02	6,18E-02	5,37E-02
0,30	1,84E-01	1,69E-01	1,54E-01	1,40E-01	1,27E-01	1,15E-01	1,04E-01	9,34E-02	8,38E-02
0,25	2,27E-01	2,12E-01	1,98E-01	1,84E-01	1,71E-01	1,59E-01	1,47E-01	1,36E-01	1,25E-01
0,20	2,74E-01	2,61E-01	2,48E-01	2,36E-01	2,24E-01	2,12E-01	2,00E-01	1,89E-01	1,79E-01
0,15	3,26E-01	3,16E-01	3,05E-01	2,95E-01	2,84E-01	2,74E-01	2,64E-01	2,55E-01	2,45E-01
0,10	3,82E-01	3,74E-01	3,67E-01	3,59E-01	3,52E-01	3,45E-01	3,37E-01	3,30E-01	3,23E-01
0,05	4,40E-01	4,36E-01	4,33E-01	4,29E-01	4,25E-01	4,21E-01	4,17E-01	4,13E-01	4,09E-01
0,00	5,00E-01	5,00E-01	5,00E-01	5,00E-01	5,00E-01	5,00E-01	5,00E-01	5,00E-01	5,00E-01
-0,05	4,40E-01	4,36E-01	4,33E-01	4,29E-01	4,25E-01	4,21E-01	4,17E-01	4,13E-01	4,09E-01
-0,10	3,82E-01	3,74E-01	3,67E-01	3,59E-01	3,52E-01	3,45E-01	3,37E-01	3,30E-01	3,23E-01
-0,15	3,26E-01	3,16E-01	3,05E-01	2,95E-01	2,84E-01	2,74E-01	2,64E-01	2,55E-01	2,45E-01
-0,20	2,74E-01	2,61E-01	2,48E-01	2,36E-01	2,24E-01	2,12E-01	2,00E-01	1,89E-01	1,79E-01
-0,25	2,27E-01	2,12E-01	1,98E-01	1,84E-01	1,71E-01	1,59E-01	1,47E-01	1,36E-01	1,25E-01
-0,30	1,84E-01	1,69E-01	1,54E-01	1,40E-01	1,27E-01	1,15E-01	1,04E-01	9,34E-02	8,38E-02
-0,35	1,47E-01	1,31E-01	1,17E-01	1,04E-01	9,18E-02	8,08E-02	7,08E-02	6,18E-02	5,37E-02
-0,40	1,15E-01	1,00E-01	8,69E-02	7,49E-02	6,43E-02	5,48E-02	4,65E-02	3,92E-02	3,29E-02
-0,45	8,85E-02	7,49E-02	6,30E-02	5,26E-02	4,36E-02	3,59E-02	2,94E-02	2,39E-02	1,92E-02
-0,50	6,68E-02	5,48E-02	4,46E-02	3,59E-02	2,87E-02	2,28E-02	1,79E-02	1,39E-02	1,07E-02
-0,55	4,95E-02	3,92E-02	3,07E-02	2,39E-02	1,83E-02	1,39E-02	1,04E-02	7,76E-03	5,70E-03
-0,60	3,59E-02	2,74E-02	2,07E-02	1,54E-02	1,13E-02	8,20E-03	5,87E-03	4,15E-03	2,89E-03
-0,65	2,56E-02	1,88E-02	1,36E-02	9,64E-03	6,76E-03	4,66E-03	3,17E-03	2,12E-03	1,39E-03
-0,70	1,79E-02	1,25E-02	8,66E-03	5,87E-03	3,91E-03	2,56E-03	1,64E-03	1,04E-03	6,41E-04
-0,75	1,22E-02	8,20E-03	5,39E-03	3,47E-03	2,19E-03	1,35E-03	8,16E-04	4,83E-04	2,80E-04
-0,80	8,20E-03	5,23E-03	3,26E-03	1,99E-03	1,18E-03	6,87E-04	3,90E-04	2,16E-04	1,17E-04
-0,85	5,39E-03	3,26E-03	1,93E-03	1,11E-03	6,19E-04	3,37E-04	1,78E-04	9,20E-05	4,61E-05
-0,90	3,47E-03	1,99E-03	1,11E-03	5,98E-04	3,13E-04	1,59E-04	7,84E-05	3,75E-05	1,74E-05
-0,95	2,19E-03	1,18E-03	6,19E-04	3,13E-04	1,53E-04	7,23E-05	3,30E-05	1,46E-05	6,21E-06
-1,00	1,35E-03	6,87E-04	3,37E-04	1,59E-04	7,23E-05	3,17E-05	1,33E-05	5,41E-06	2,11E-06

Appendix C Uncertainty in site response analysis up to the model base

The following memo has been reviewed by J. Bommer and A. Rodriguez Marek.

To: Julian Bommer and Adrian Rodriguez-Marek
Copy: Sjoerd de Wit, Jan Van Elk, Edith Van Dijk; NAM
From: Amalia Giannakou, Panagiotis Georgarakos and Jacob Chacko; Fugro
Subject: Estimation of Amplification Factor from top of Bedrock to Base of 2D Finite Element Models of Eemshaven-Delfzijl Levee, Groningen, The Netherlands

Introduction and Background

Gas-extraction-induced earthquakes occur in the Groningen area. Consequently earthquake effects are to be considered in the levee reconstruction program for the Eemshaven-Delfzijl levee. In particular the presence of potentially liquefiable Holocene tidal deposits (i.e. the so-called “wadzand” deposits) underlying parts of the Eemshaven-Delfzijl levee have raised the issue of liquefaction-induced instability. Since the effect of liquefaction on structures and liquefaction-induced deformations cannot easily be assessed using simplified techniques, the dynamic stability of the levee at two locations was evaluated by Fugro using advanced numerical procedures. The 2D dynamic analyses were conducted using nonlinear, fully coupled, effective stress models (Fugro 2016). The 2D FE models extend from the top of levee to El. -30 m NAP at the Eemshaven area and to El. -20m NAP at the Delfzijl area (Figure 1). The results of the analyses were presented at the Liquefaction Expert Panel during the Workshop in Amsterdam (November 17th-18th 2016).

An effort is currently underway to:

- Characterize the uncertainties related to the input and output of the 2D FE dynamic analyses model (i.e. coupled, effective stress FEM)
- Perform FORM analysis using the 2D FE dynamic analyses model; and
- Make an informed decision about design values including length effects that contribute to the design return period.

For Step 1 above it is necessary to specify distributions for the different stochastic variables that affect the problem. The main stochastic variables associated with the seismic demand that is used as input in the 2D FE model include:

- the spectral acceleration at NSUB and
- the Amplification Factor from top of rock (NSUB) to the base of the 2D FE models (currently at El. -30 m and -20 m NAP).

Design spectra provided by KNMI were used to define the seismic demand at the top of NSUB for the design return period. For the estimation of the distribution of spectral acceleration values at top of NSUB, the seismic hazard curve for $T=0.85\text{sec}$ at the top of NSUB is used. The seismic hazard curve is approximated with a logarithmic probability density function and this distribution is used in the FORM analyses.

In addition to the spectral acceleration at the top of bedrock (NSUB) the amplification of the ground motion from the top of bedrock to the base of the 2D FE models (i.e. NAP -30 m and -20 m) needs to also be considered. In the V2 Groningen report (Bommer et al 2015), only the Amplification Factor from top of rock to the ground surface is provided (Equations ES.15 and Es.16).

This project memorandum presents a methodology to derive estimates of amplification factor from top of rock (NSUB) to the base of the FE models (NAP -30 m and -20 m) following the procedure of Stewart et al (2014).

Proposed Approach

For the estimation of the amplification factor at the base of the 2D FE models we have followed the approach of Stewart et al (2014) for fitting ground response analysis results to a site amplification function.

1D equivalent linear site response analyses were performed at select locations along the levee to propagate the motion from the top of NSUB to the base of the 2D FE model. The deep shear wave velocity profiles provided by Professor Rodriguez-Marek in an email dated October 4th 2016 were used (Vs_profiles_levee_csv_mod_with corrected u0_20160902_GdL_ARM.xlsx).

Equivalent linear site response analyses were performed for different amplitudes of input motions. Results of the site response analyses were regressed using the following functional form:

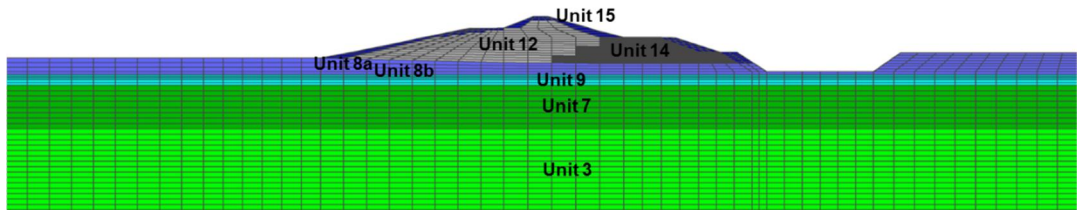
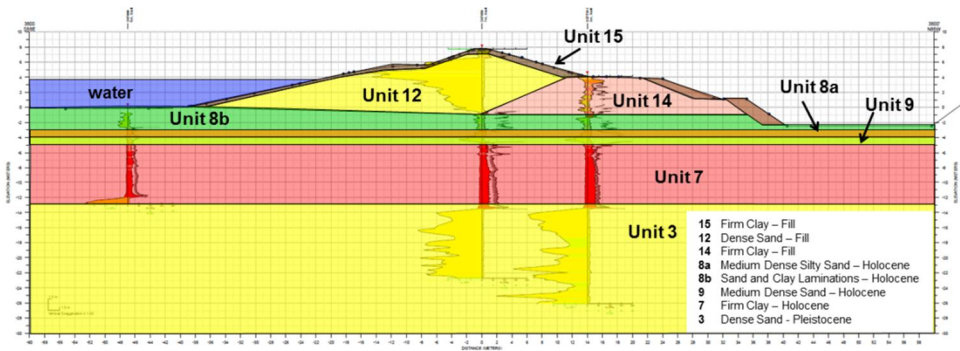
$$\ln \bar{Y}(f) = f_1 + f_2 \ln \left(\frac{x_{IMref} + f_3}{f_3} \right)$$

and constraining f_3 to a value of 0.5, the same value used in Bommer et al (2015). Regression of the site response analyses results was performed to estimate f_1 and f_2 factors. For the estimation of f_1 (which represents weak-motion (linear) amplification) site response analyses were performed for an input PGA amplitude of 0.01g. The amplification factor at the base of the FE models was defined as the ratio of the outcrop motion at NAP -20 m (or -30m) to the outcrop motion at the top of NSUB.

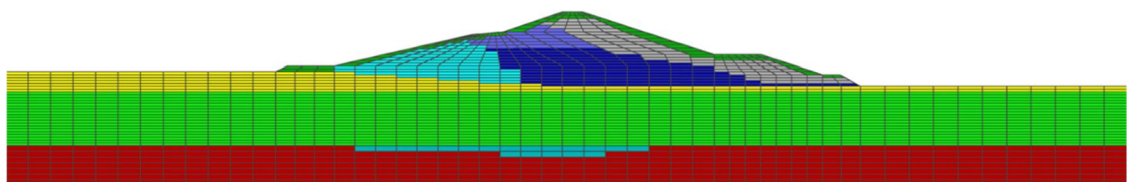
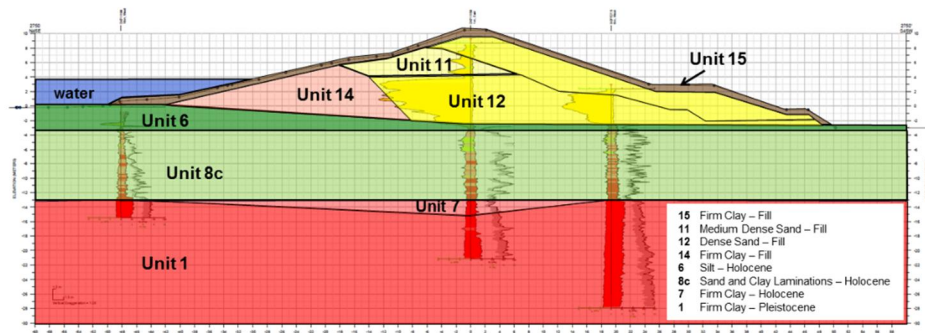
Estimation of Amplification Factor from NSUB to Base of 2D FE Model

This section presents example results for the Delfzijl area using the approach described above. Site response analyses were performed at the Delfzijl side of the levee using 7 ground motions with 2 horizontal components matched to the normalized target spectrum at top of NSUB. Ground motions were scaled to PGA values of 0.01g, 0.1g, 0.16g, 0.2g, 0.3g, 0.4g, and 0.5g to obtain amplification factors at multiple hazard levels. The estimated V_{s30} value below -20m NAP is 288 m/s. Figure 2 presents regression results of the amplification factor using $f_1 = 0.67$, $f_2 = -0.49$ and $f_3 = 0.5$.

Figure 2 presents the mean amplification factor between top of NSUB and El – 20 m. No site specific geotechnical data are available below NAP -20 m and the deep velocity profiles at the Delfzijl side (i.e. between NAP -20m to top of NSUB) are almost the same. Much of the site to site variability is thus expected to be related to the soils above NAP -20 meters. The minimum value of the standard deviation for site-to-site variability for amplification ratios between NSUB and the ground surface is constrained to 0.2 in Bommer et al (2015). When we compare the variation in amplification ratios between NSUB and the ground surface from 9 different profiles in the Delfzijl area, we estimate a standard deviation of 0.2, which is associated largely with variability above El. -20 meters. Therefore we propose to reduce the standard deviation for site-to-site variability in amplification ratios between top of NSUB and the base of the FE models to 0.1 (in natural log units).



El. -30 m NAP



El. -20 m NAP

Figure 1. FE models at Eemshaven (upper illustration) and Delfzijl (lower illustration) side of the levee.

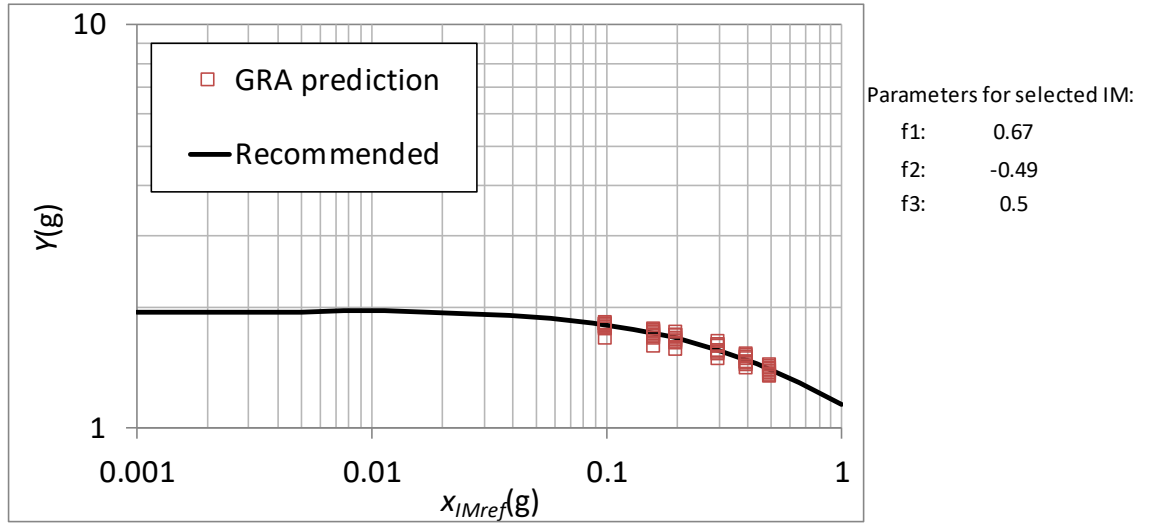


Figure 2. Mean amplification values for Sa (0.85 sec) from GRA and mean fit using equation above with f_3 fixed at 0.5.

The resulting equation for the mean amplification factor from top of NSUB to NAP-20 m is shown below:

$$\ln(AF) = 0.67 - 0.49 \ln[(SaNU_{B,g} + 0.5)/0.5]$$

The proposed standard deviation of the amplification function is 0.1 (ln units).

References

- Bommer, J.J., Dost B., Edwards B., Kruiver P.P., Meijers P., Ntinalexis M., Polidoro B., Rodriguez-Marek A. and Stafford P.J. (2015) "Development of Version 2 GMPEs for Response Spectral Accelerations and Significant Durations from Induced Earthquakes in the Groningen Field", Report Groningen Seismic Hazard and Risk Assessment Model.
- Fugro (2016) "Evaluation of Dynamic Stability Eemshaven-Delfzijl Levee, the Netherlands", prepared for NAM, December 2016
- Stewart J.P and Hashash, Y. M. A. (2014). "Guidelines for Performing Hazard-Consistent One-Dimensional Ground Response Analysis for Ground Motion Prediction," PEER Report 2014/16, October 2014.

Note: The coefficients for Eemshaven are $f_1 = 0.37$, $f_2 = -0.32$, $f_3 = 0.5$ and $\phi = 0.1$.

Appendix D Cyclic Resistance of Laminated Deposits

The following memo has been prepared by Fugro on January 31st 2017 and has been revised on February 10th to address comments by Professor S. Kramer

INTRODUCTION AND BACKGROUND

Gas-extraction-induced earthquakes occur in the Groningen area. Consequently earthquake effects are to be considered in the levee reconstruction program for the Eemshaven-Delfzijl levee. In particular the presence of potentially liquefiable Holocene tidal deposits (i.e. the so-called “wadzand” deposits) underlying parts of the Eemshaven-Delfzijl levee have raised the issue of liquefaction-induced instability.

In order to estimate the liquefaction triggering resistance of these deposits empirical procedures based on measured CPT tip resistance were used (i.e. Boulanger and Idriss 2014) as well as a series of advanced cyclic laboratory tests on “undisturbed” samples (Fugro 2016a). As discussed in Fugro (2016b) although liquefaction triggering resistance from CPT measurements in uniform sand deposits compared reasonably well with cyclic laboratory test results on “undisturbed” samples from uniform sands (differences in results were mainly attributed to effects of sample disturbance resulting to loosening of samples tested in the lab), liquefaction triggering resistance from CPT measurements in laminated deposits appear to underestimate the triggering resistance of these deposits when compared to results from cyclic laboratory tests on laminated “undisturbed” samples. This is most likely due to the significant influence of the clay layers on the CPT tip resistance measured within the thin “sandwiched” sand layers whose thickness is less than 10 to 20 cm in thickness.

Laminated deposits are mostly present between km 27.2 to 28.5 (Section L) and around km 29.5 (Section K) at the Delfzijl side as well as around km 36.0 (Section D) at the Eemshaven side.

In order evaluate the cyclic resistance of laminated deposits the following were considered:

1. CDSS and CTX test results on laminated deposits. Five (5) CDSS and seven (7) CTX cyclic tests were performed on laminated “undisturbed” samples obtained with Piston and Begemann samplers (Fugro 2016a). Additionally, three (3) CDSS and seven (7) CTX were performed on laminated “undisturbed” samples (without static bias) obtained with the Gel Push sampler. The results of these additional tests have been interpreted and are plotted together with the interpreted lab results presented in Fugro 2016b.
2. Numerical simulations of cyclic response of laminated samples performed to evaluate the conversion factor between Cyclic Simple Shear and Cyclic Triaxial tests on laminated samples
3. Numerical simulations of the response of laminated samples under cyclic simple shear loading conditions to develop liquefaction triggering curves for samples with different percentages of clay laminations

This project memorandum presents interpreted laboratory test results on laminated samples and results of numerical evaluations of the cyclic behavior of laminated soils and provides recommendations for the cyclic resistance of laminated deposits.

EVALUATION OF LIQUEFACTION TRIGGERING FROM CYCLIC LABORATORY TESTS

A series of stress controlled Cyclic Direct Simple Shear (CDSS) and Cyclic Triaxial (CTX) tests was performed on “undisturbed” samples (i.e. obtained with Piston and Begemann samplers) from “wadzand” deposits (Fugro 2016a).

Five (5) CDSS tests were performed on samples that included clay laminations and seven (7) CTX tests were performed on laminated/stratified coarse- and fine-grained materials. Interpretations of these test results in the form of liquefaction triggering curves were presented in Fugro (2016b).

Fugro performed an additional site investigation campaign in October 2016 using the Gel Push sampler to collect high quality “undisturbed” samples from the tidal deposits at the same locations where Piston and Begemann samples were collected. Xrays and MSCL scanning was performed on select Gel Push Tubes. Review of Xray and MSCL results indicated less disturbance (i.e. higher quality samples) effects on Gel Push samples compared to Piston and Begemann samples.

Additional cyclic tests were performed on select Gel Push samples. Three (3) CDSS tests and seven (7) CTX tests were performed on laminated Gel Push samples. In addition, six (6) CDSS tests were performed on uniform sand samples. These additional cyclic test results on Gel Push samples together with Xray and MSCL scans of the Gel Push Tubes will be included in an Addendum to the Factual Report, currently under preparation.

A summary of the tests performed on uniform and laminated tidal deposits without bias is presented in Table 1. The reported void ratios on Table 1 are the initial void ratios of the overall sample consisting of either sand only (Unit 8a) or sand/clay laminations (Units 8b and 8c).

Table 1. Summary of Cyclic Tests on Laminated and Uniform Samples (no bias)

Unit	Initial void ratio, e_0	Description	CPT classification zone - I_c	Tests
8a	~ 0.62 – 0.76	mainly sand (non-laminated, not seen in Delfzijl)	CPT classification zone 6 (Robertson) $I_c < \sim 2.05$	CSS03 (B), CSS05 (B), CSS15R (P), CSS08 (GP), CSS22R (GP), CSS23(GP), CSS27(GP), CSS28(GP), CSS25(GP)
8b	~ 0.79 – 0.92 (lower end of the void ratio range for laminated deposits, primarily from Eemshaven boreholes)	laminated, with higher percentages of sands	CPT classification zone 5 (Robertson) $\sim 2.05 < I_c < \sim 2.6$	CSS13 (P), CSS17(P), CSS18 (P), CSS19 (GP), CSS20 (GP), CSS21 (GP) CTX06 (P), CTX07 (P), CTX08 (GP), CTX12 (GP)
8c	~ 0.99 – 1.25 (higher end of the void ratio range for laminated deposits, from Delfzijl boreholes)	laminated, with lower percentages of sands and higher percentages of clay	CPT classification zones 5 and 4 (Robertson) 5 : $\sim 2.05 < I_c < \sim 2.6$ 4 : $2.6 < I_c < 2.95$ (screened out in simplified method)	CTX01 (P), CTX02 (P), CTX03R (P), CTX17(GP), CTX10 (GP), CTX14 (GP), CTX16 (GP), CTX15 (GP)

Unit	Initial void ratio, e_0	Description	CPT classification zone - I_c	Tests
9a	~ 0.63 – 0.75	Grey or dark grey fine sand	CPT classification zone 6 (Robertson) $I_c < \sim 2.05$	CCS01 (P), CCS07R (P), CCS11 (P)
9b, 9c	~ 0.95, 1.18	Grey or dark grey fine sand with thin laminae of dark clay and silt.	CPT classification zones 5 and 4 (Robertson) 5 : $\sim 2.05 < I_c < \sim 2.6$ 4 : $2.6 < I_c < 2.95$	CTX04 (P), CTX05 (P)

Figure 1 presents the Cyclic Stress Ratio (CSR) as a function of the number of cycles to liquefaction from the CDSS and CTX tests performed on Piston, Begemann and Gel Push samples from tidal deposits without static bias. For the CDSS tests without bias, liquefaction was considered to have triggered at 3.0 percent Single Amplitude shear strain. For the CTX tests without bias liquefaction was considered to have triggered at 1.5-2 percent Single Amplitude axial strain. We note that the CSRs of the CTX tests on laminated samples plotted on Figure 1 have been multiplied by a factor of 0.8 to convert to equivalent cyclic simple shear loading conditions based on results of numerical simulations as discussed in the following section.

As discussed in Fugro (2016b) due to the variable nature of the inter-tidal deposits, it is near impossible to identify identical samples with the same void ratio (relative density or percentage clay layers) for cyclic testing at multiple cyclic stress ratios. Therefore, it was not possible to characterize laminated samples in terms of relative density since the direct measurement of minimum/maximum density is not possible on each variable sample. In order to provide a basis for identifying similar samples and to develop reasonable cyclic resistance versus number of cycles relationships, the initial sample void ratio was used as an indicator and is plotted next to each test on Figure 1. These void ratio values provide an indication of absence of thin fine-grained layers within the sample (corresponding to void ratios less than about 0.76, Unit 8a, from uniform samples collected from Eemshaven boreholes) or presence of thin fine grained layers within the sample (void ratios of about 0.85, Unit 8b, from laminated samples primarily collected from Eemshaven boreholes and void ratios higher than 1 from laminated samples primarily collected from Delfzijl boreholes). As shown on this figure the samples tested all have different void ratios.

On Figure 1 liquefaction triggering curves are shown for:

- Relatively Uniform sand, Unit 8a (solid black line) present at Eemshaven explorations (i.e km 38.5, 38.0, 37.5 and 37.2). This unit is practically absent from Delfzijl explorations (i.e. it could only be identified in about 2% of the total CPT penetration length performed at Delfzijl side). The dashed black line is the interpreted liquefaction triggering curve for Unit 8a in Fugro 2016b that was also used in the effective stress dynamic levee stability evaluations (Fugro, 2016c).
- Laminated sand and clay deposits with higher percentages of sands, Unit 8b, (solid blue line) present primarily at Eemshaven explorations and to a lesser degree at Delfzijl explorations (i.e. only 2 of the 12 laminated samples tested from Delfzijl explorations had initial void ratios less than 1). The dashed blue line is the interpreted liquefaction triggering curve for Unit 8b in Fugro 2016b that was also used in the effective stress dynamic levee stability evaluations (Fugro, 2016c).
- Laminated sand and clay deposits with lower percentages of sands, Unit 8c, (solid purple line) present at Delfzijl explorations (i.e. only 10 of the 12 samples tested from Delfzijl explorations had initial void ratios larger than 1)

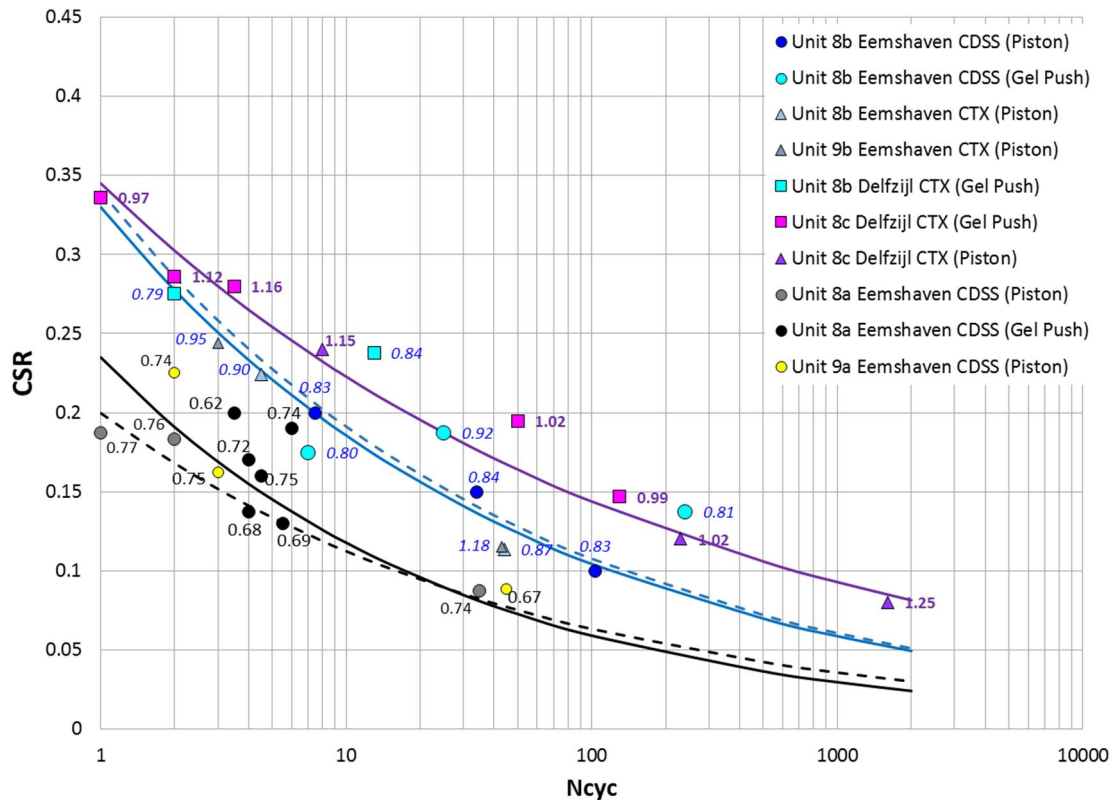


Figure 1. Liquefaction Triggering Resistance of Uniform (Unit 8a, Unit 9a) and Laminated Samples (Unit 8b, Unit 8c, Unit 9b) from Tidal Deposits (no static bias). The initial void ratio (before application of consolidation stress) is plotted next to each test.

NUMERICAL SIMULATIONS OF CYCLIC RESPONSE OF LAMINATED DEPOSITS

Evaluation of Conversion Factor from Cyclic Triaxial to Cyclic Simple Shear Loading

Two types of cyclic testing were used to assess the liquefaction triggering of the tidal deposits: i) CTX and ii) CDSS tests. Although CDSS tests provide more representative loading conditions, the small specimen height (i.e. 3 cm) in combination with the nature of the laminated deposits (i.e. clay lamination thicknesses on the order of 1-2 cm) necessitated the testing of taller specimens for the laminated samples. Therefore CTX tests were performed for most of the laminated samples although a number of CDSS tests were also performed on specimens with clay laminations.

In order to correlate the two cyclic testing types, Seed and Peacock (1971) recommended a conversion factor applied on the CSR_{TX} (i.e. cyclic stress ratio from triaxial testing) ranging from 0.6 to 0.7 for normally consolidated specimens based on data for clean sands. The recommended conversion factor depended on the value of the coefficient of earth pressure at rest, K_0 .

For fine-grained samples, Donahue et al (2007) reported that:

- when studying the liquefaction susceptibility of a normally consolidated fine-grained soil deposit after the 1989 Loma Prieta earthquake, Boulanger et al. (1998) used a conversion factor of 0.7
- Sancio (2003) found a conversion factor of 0.85 when testing shallow, fine-grained soils from Adapazari with a $PI < 12$, at a mean effective stress of 100 kPa.

Donahue et al (2007) used a conversion factor of 0.84 based on results from CDSS and CTX tests on fine-grained samples reconstituted with the Slurry Deposition Method and tested at an effective confining pressure of 50 kPa.

In order to evaluate the conversion factor between CTX and CDSS tests on laminated deposits, numerical simulations were performed with the finite difference code FLAC2D (Itasca 2016).

As a first step, numerical simulations were performed to estimate the conversion factor between CTX and CDSS tests on a uniform sand sample (i.e. Unit 8a). PM4Sand constitutive model was used to model the cyclic behavior of a uniform sand sample under cyclic direct simple shear loading conditions. The model was calibrated to the liquefaction triggering curve for Unit 8a (black line) shown on Figure 1 (Fugro, 2016c).

Having simulated the CDSS test results on a uniform sand sample, numerical simulations of a uniform sand sample under cyclic plane strain compression loading conditions ($K_0=1$) were performed to approximate the CTX test. Figure 2 presents liquefaction triggering results from numerical simulations of a uniform sand sample under cyclic direct simple shear and plane strain compression (CPSC) loading conditions for different CSR. The resulting conversion factors range between 0.64 and 0.72 for a uniform sand sample which are in agreement with the range proposed by Seed and Peacock (1971) for uniform sands.

As a second step, numerical simulations were performed to estimate the conversion factor between CTX and CDSS tests on a laminated sample. First numerical simulations of test CTX07 (i.e. CSR=0.28, initial void ratio $e_0=0.9$) on a laminated sample were performed. Figure 3 shows a photo of Sample CTX07, the X-ray section and the detailed 2D numerical model. The clay laminations were identified in the sample using the X-ray section, leading to the idealized numerical grid shown in the same Figure 3. The calibrated parameters for PM4Sand were used for the sand layers within the sample while the clay layers were modeled with a Mohr-Coulomb model. The deformed shape of the numerical model is compared with the cyclic triaxial sample on Figure 4, showing somewhat similar characteristics. Also, shown on Figure 5 is the development of cyclic strains versus cycles of loading. Both experiment and simulation suggest triggering (1.5% axial strain) at about 4 to 4.5 cycles. The cyclic responses are also compared in terms of stress-strain plots, and as stress paths. Again similar trends are noted in both experiment and simulation despite the idealization of the clay laminations and the differences in loading conditions (plane-strain versus triaxial).

Having simulated the cyclic behavior of a laminated sample under cyclic triaxial conditions reasonably, numerical simulations of the same laminated sample under cyclic simple shear conditions were performed. Figure 6 presents liquefaction triggering results from numerical simulations of a laminated sample under cyclic direct simple shear and plane strain compression loading conditions for different CSR. The resulting conversion factors range between 0.78 and 0.83 for a laminated sample which are higher than the conversion factors of uniform sand deposits, but in line with experimental findings on fine-grained samples discussed above.

Based on the above a conversion factor of 0.8 was applied on the CSRTX for the laminated samples.

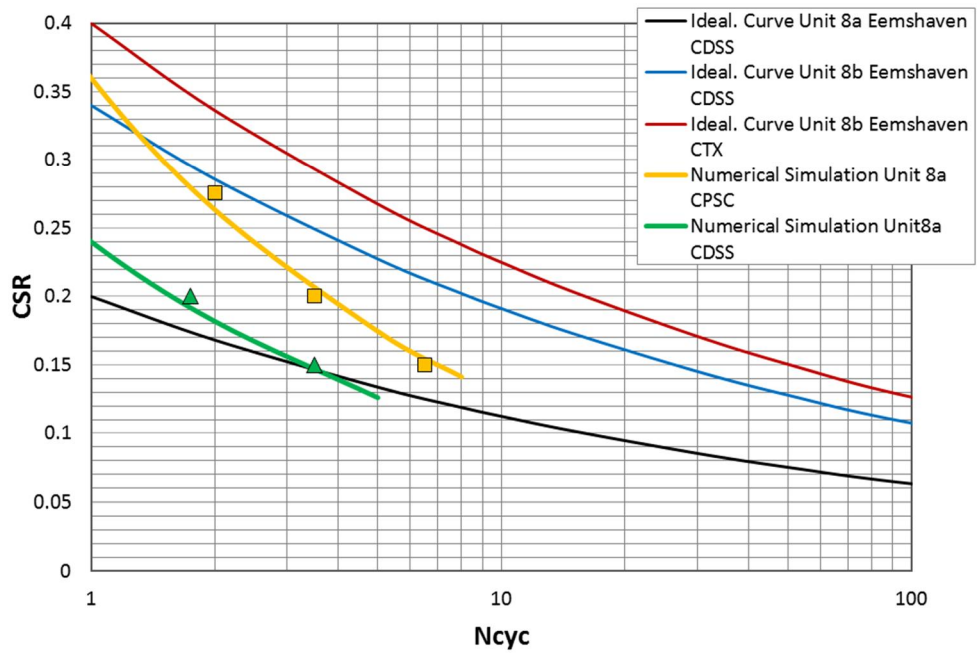


Figure 2. Liquefaction triggering curves obtained from numerical simulations of CDSS and CPSC loading conditions on uniform sand (Unit 8a).

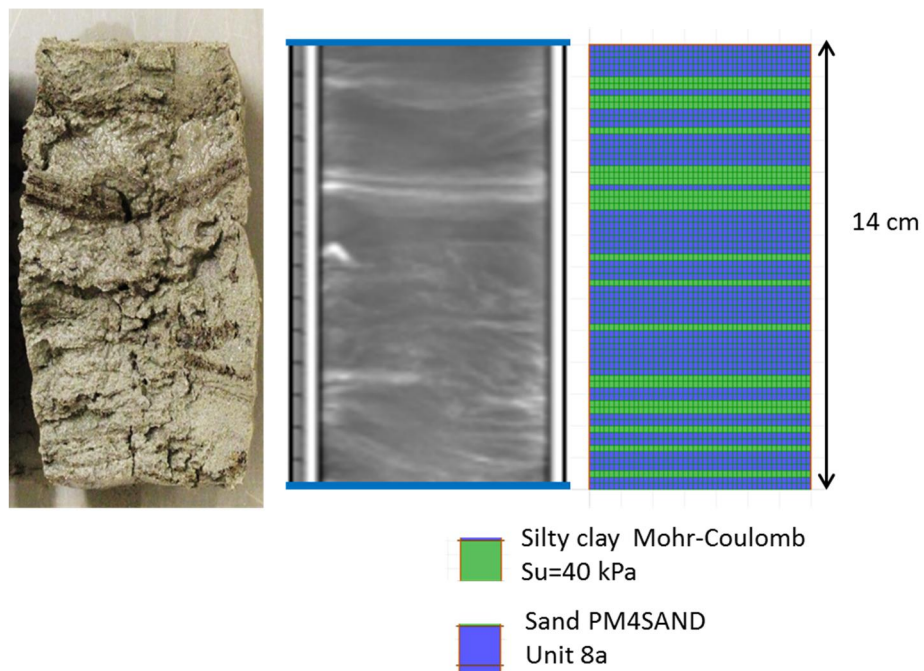


Figure 3. Photo, X-ray section and numerical model of laminated sample CTX07.



Figure 4. Photo (left) and deformed grid (right) of laminate sample CTX07 at the end of cyclic loading.

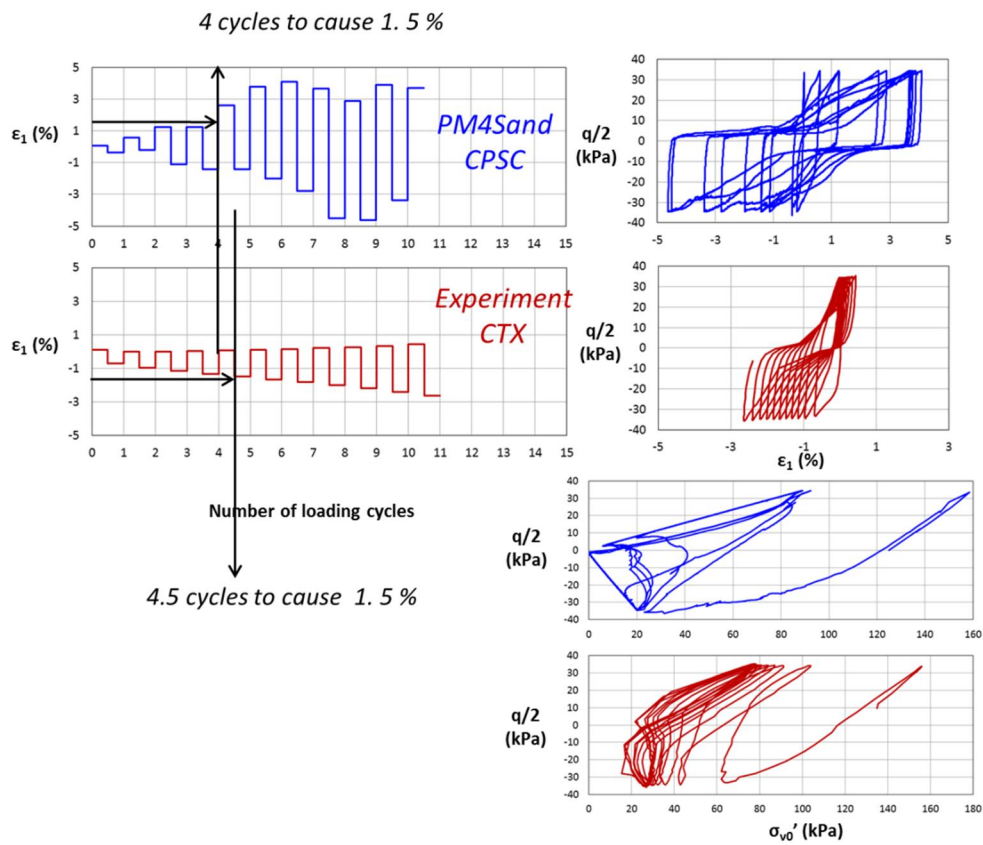


Figure 5. Comparison between numerical and experimental results for laminated sample CTX07.

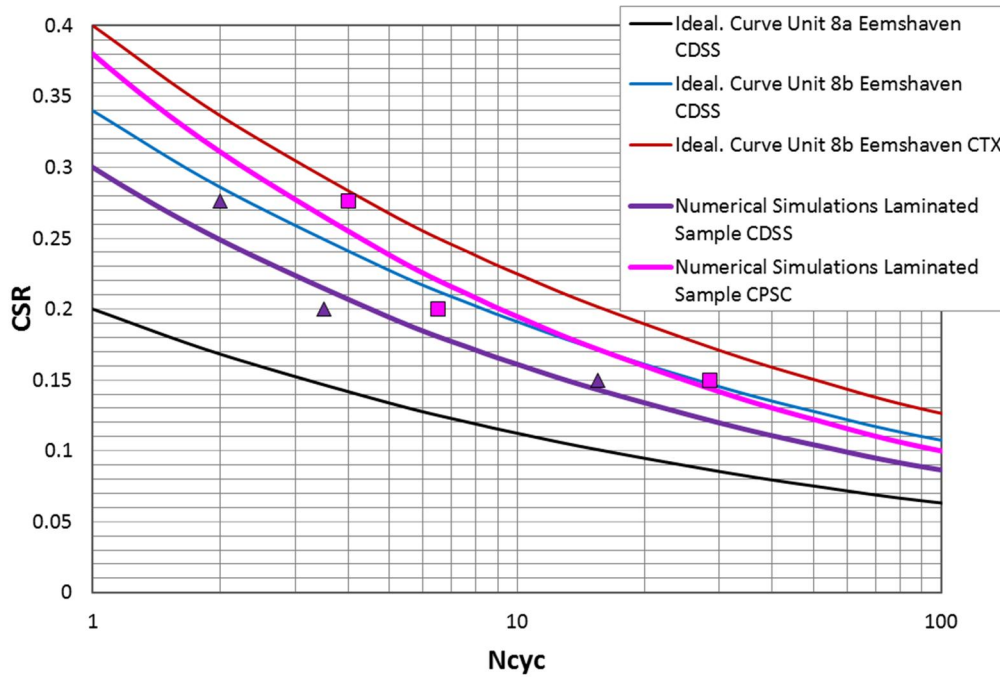


Figure 6. Liquefaction triggering curves obtained from numerical simulations of CDSS and CPSC loading conditions on laminated sample (shown on Figure 3).

Evaluation of Liquefaction Triggering

Numerical simulations of laminated samples under cyclic direct simple shear loading conditions were performed in order to develop estimates of liquefaction triggering resistance for different percentages of clay laminations within the sample.

First numerical simulations of test CDSS18 (i.e. CSR=0.2, initial void ratio $e_0=0.83$) on a laminated sample were performed. Figure 7 shows a photograph of Sample CDSS18. Two clay sub-layers/laminations are identified in the sample. The calibrated parameters for PM4Sand and UBCSAND for Unit 8a were used for the sand layers within the sample while the clay layers were modeled with a Mohr-Coulomb model. Figure 8 presents a comparison between the laboratory test and numerical simulation test results. The percentage of clay laminations (CPL) within this sample was estimated to be on the order of 40% (defined as the total thickness of clay laminations within the sample divided by the sample height). Using the same configuration (CPL=40%), the numerical model was subjected to CSR=0.15 in an attempt to reproduce the test CDSS17 ($e_0=0.84$). The comparison between numerical and experimental results for CDSS17 is shown on Figure 9.

Having simulated reasonably the CDSS test results on a laminated sample, parametric numerical simulations of CDSS tests on laminated samples with different percentages of clay laminations and different distributions of clay laminations within the sample were performed in order to evaluate the liquefaction triggering resistance of laminated sample. Simulations were performed at different CSR values. Analyses were performed using both PM4Sand and UBCSAND models (calibrated to Unit 8a triggering curves) to simulate the sand layer behavior.

Figure 10 presents results of numerical simulations of CDSS tests on laminated samples with clay lamination percentages (CLP) ranging from 10% to 60% (grey lines) plotted together with interpreted lab results shown on Figure 1. Different distributions of clay laminations within the sample were assumed in the numerical simulations of CDSS tests (example schematizations shown on Figure 11a).

The numerical results shown on this figure are from analyses using UBCSand to model the sand layer behavior. As shown on Figure 10:

- numerical simulations of CDSS tests on laminated samples with CLP of 40% (i.e. higher sand percentage within the sample) produce results close to the liquefaction triggering curve from lab results for Unit 8b (blue line)
- numerical simulations of CDSS tests on laminated samples with CLP of 60% (i.e. lower percentages of sands and higher percentages of clay) produce results close to the liquefaction triggering curve from lab results for Unit 8c (purple line)
- results of numerical simulations show that even the presence of a small amount of clay laminations in the sample (i.e. CLP 10%) results in an increase of cyclic resistance compared to the uniform sand sample

It is also noted that results of parametric numerical analyses of different distributions of clay and sand layers within a sample for a given CLP (Figure 11a) indicate that the distribution of the clay layers within the sample does not significantly change the triggering resistance.

Figure 11b presents a comparison of the liquefaction triggering curves derived from numerical simulations of CDSS tests on laminated samples using PM4Sand and UBCSand to model the sand layers. As shown on Figure 11, the two models predict a similar trend.

The black line on Figures 11a and 11b correspond to the triggering resistance of a sand layer without clay laminations.

We note that as discussed in Fugro (2016c) numerical analyses results indicate that void redistribution effects, tend to be reduced as the thickness of sand layers decreases, or as the percentage of clay interlayers increases.

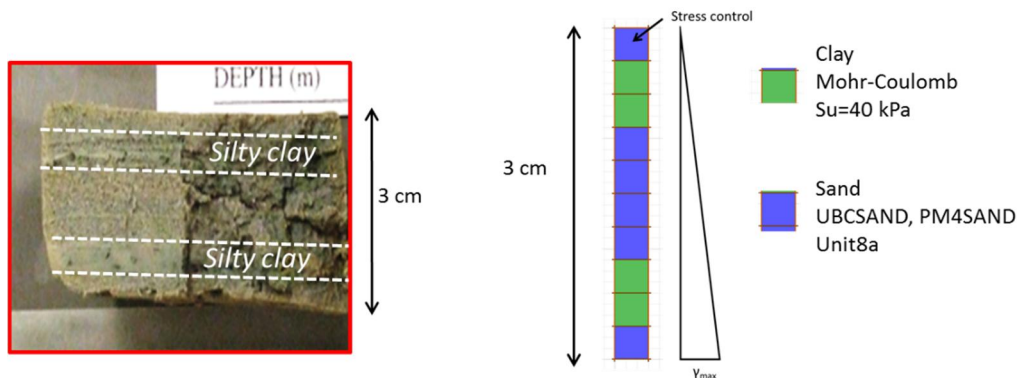


Figure 7. Photo and numerical model of laminated sample CDSS18.

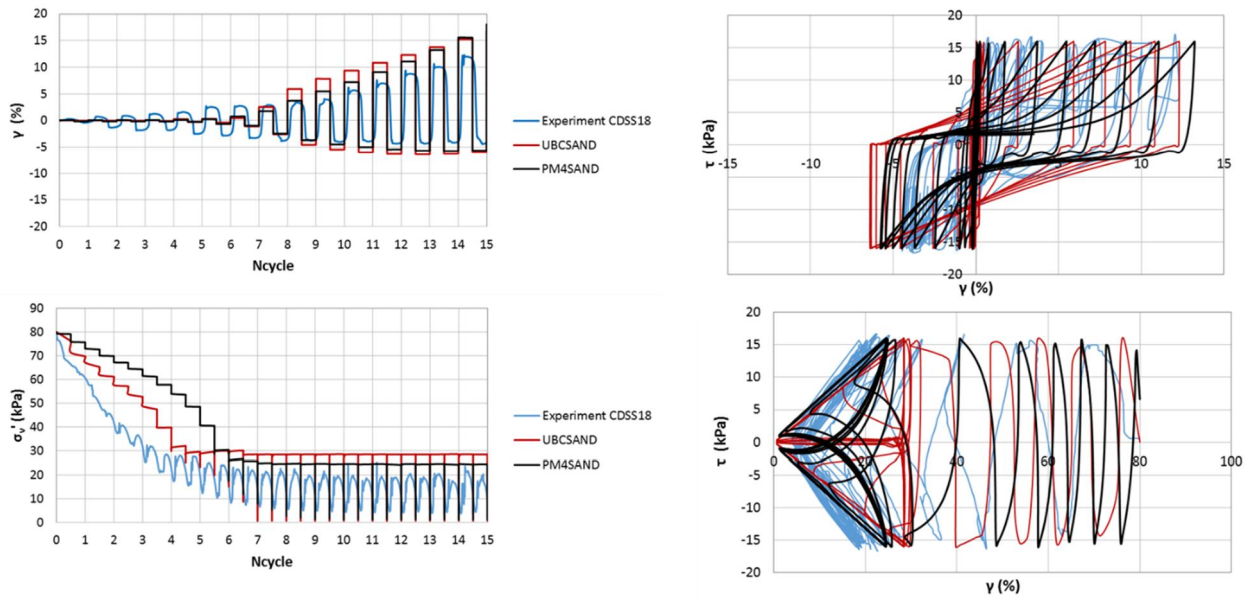


Figure 8. Comparison between numerical and experimental results for laminated sample CDSS18.

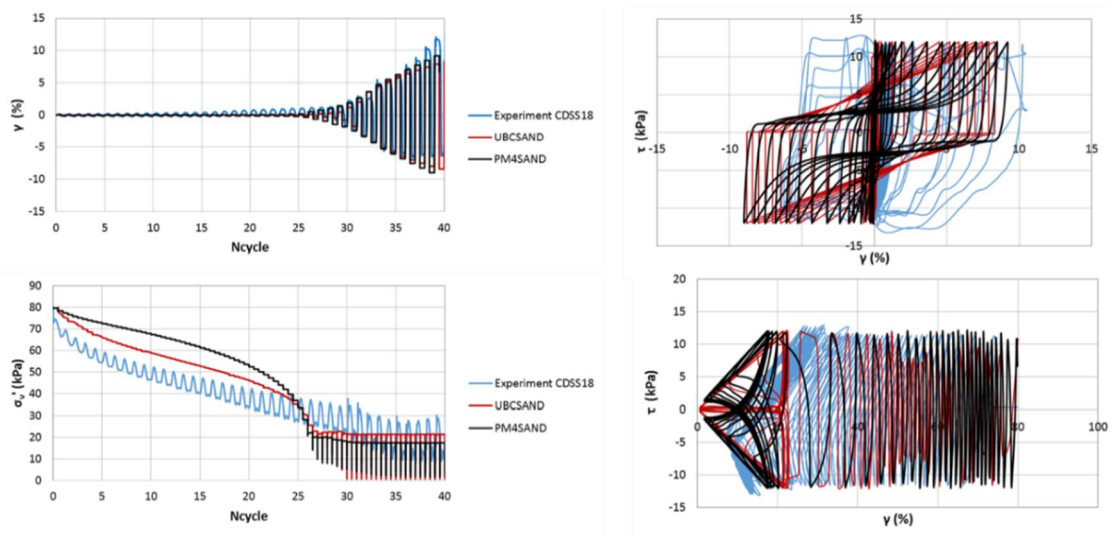


Figure 9. Comparison between numerical and experimental results for laminated sample CDSS17.

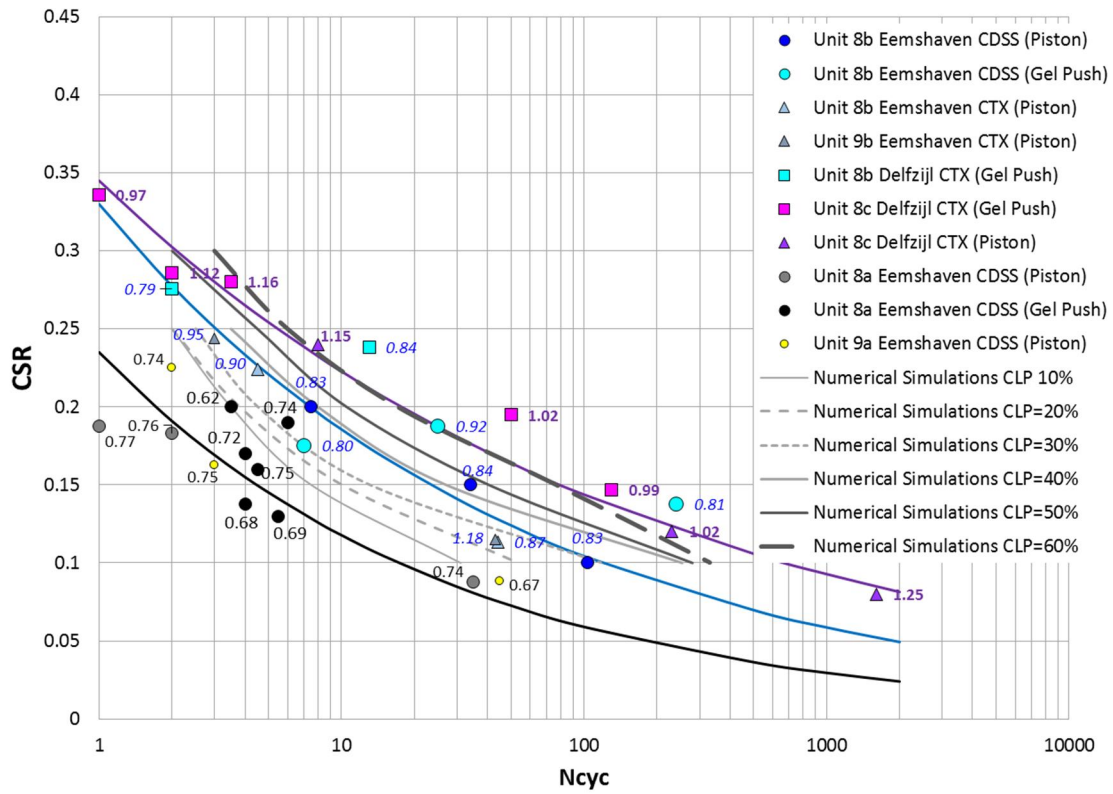


Figure 10. Liquefaction Triggering Resistance Curves from Numerical Simulations of CDSS tests on Laminated Samples with different clay lamination percentages.

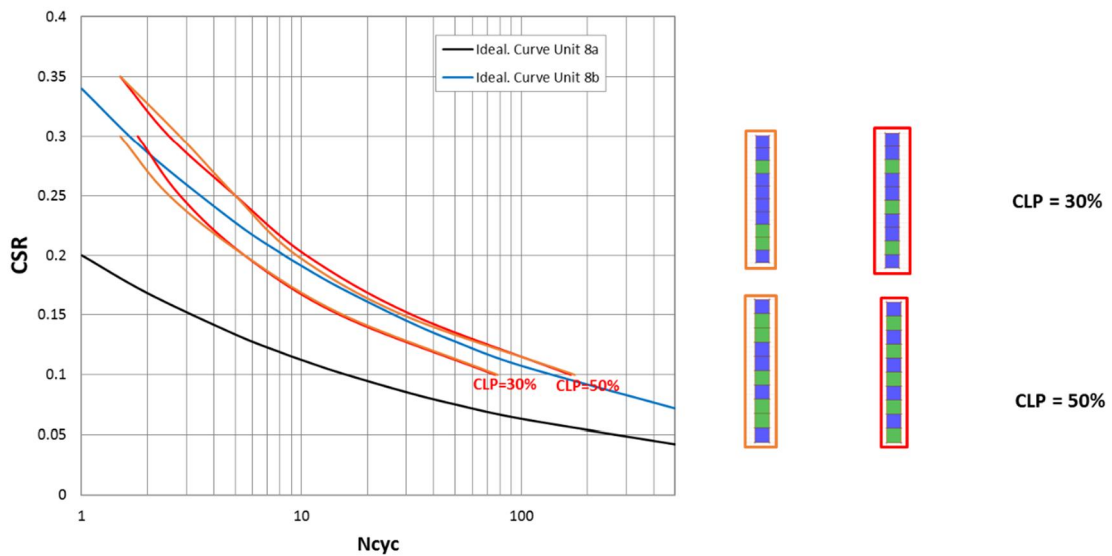


Figure 11a. Numerical simulation results for CLP 30% and 50% assuming different distributions of clay laminations within the sample.

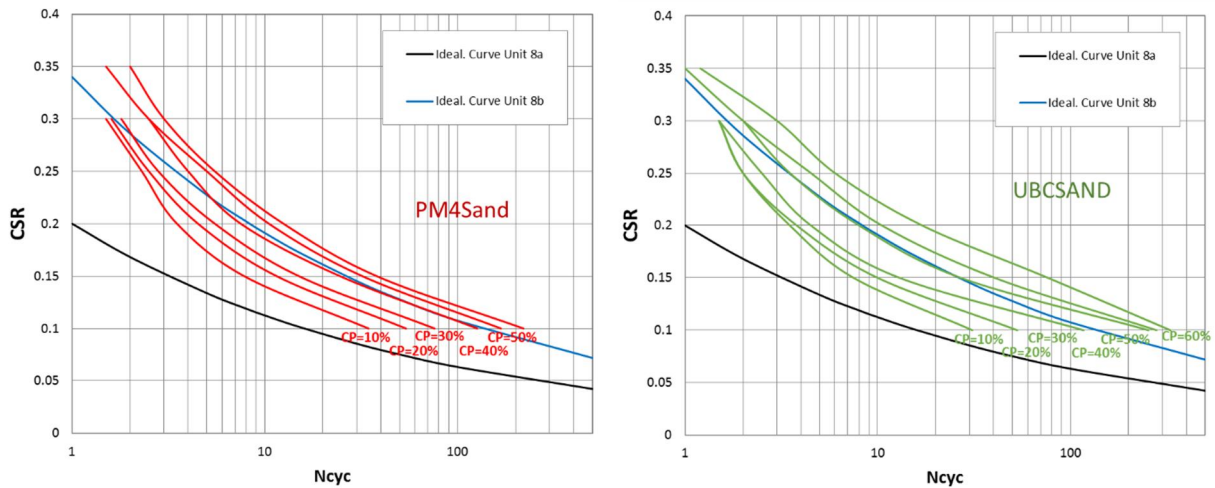


Figure 11b. Liquefaction Triggering Resistance Curves obtained from Numerical Simulations of CDSS tests on Laminated Samples with different clay lamination percentages (left: PM4Sand and right: UBCSAND).

PROPOSED CRR DISTRIBUTION FOR LAMINATED DEPOSITS

Interpreted laboratory test results and numerical simulations were used to develop a proposed distribution of the cyclic resistance (CRR) of laminated deposits at the Delfzijl side of the levee for locations where Unit 8 is present for use in FORM analyses. For these evaluations the number of cycles corresponding to a magnitude M 5 earthquake (i.e. N=4) was estimated using the MSF of Boulanger and Idriss (2014).

As discussed previously the cyclic test results were evaluated considering separate groups of materials including: Unit 8b – Laminated materials with a higher percentage of sands ($0.79 < e_o < 0.92$) and Unit 8c – Laminated materials with a lower percentage of sands ($0.99 < e_o < 1.25$). These laboratory test data were regressed to develop distributions of cyclic resistance for each group of samples. Figure 12 shows the regressions for Unit 8b samples including the mean and 90% confidence interval, while Figure 13 shows the regression for Unit 8c samples.

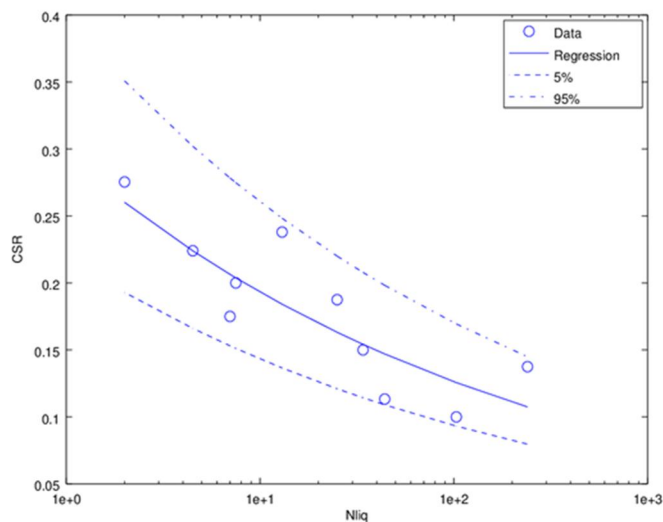


Figure 12. CRR for Unit 8b samples.

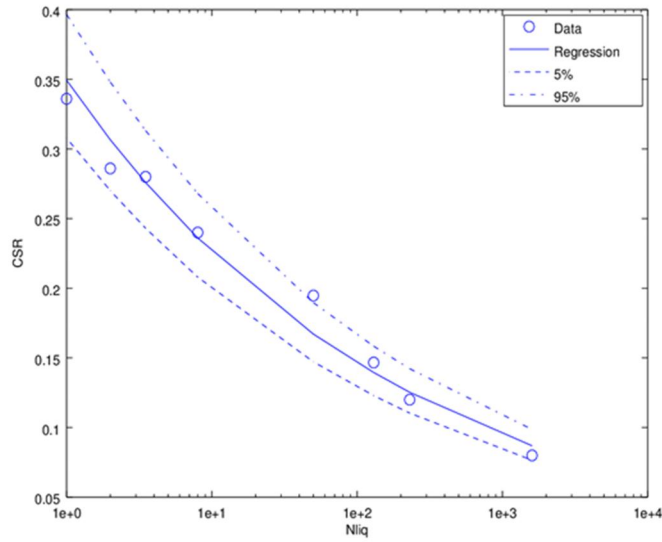


Figure 13. CRR for Unit 8c samples.

The CPT classification data also provide an indicator of the relevant content of sand within the laminated deposits. Qualitative assessments of the available CPT data suggest that in Delfzijl the laminated deposits are composed of about 50% of Unit 8b type material and 50% Unit 8c type material.

For these evaluations the number of cycles corresponding to a magnitude M 5 earthquake (i.e. N=4) was estimated using the MSF of Boulanger and Idriss (2014). Probability density functions corresponding to the cyclic resistance at 4 cycles were calculated for the Unit 8b and Unit 8c materials above and a combined distribution developed assuming equal weights to each of the two distributions. These probability density functions are shown on Figure 14.

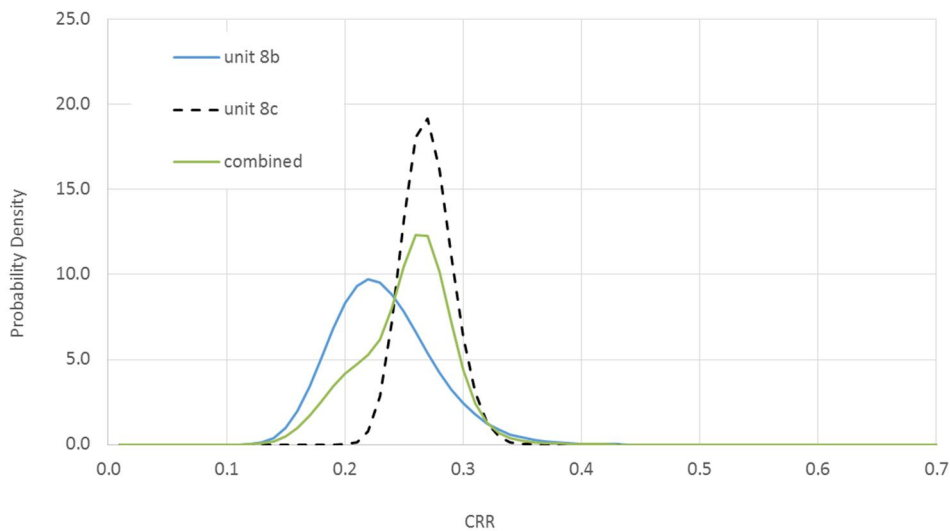


Figure 14. Probability Density Function for Unit 8b, 8c and combined.

The cumulative probability density of the combined distribution is shown relative to the lognormal fit of the distribution on Figure 15.

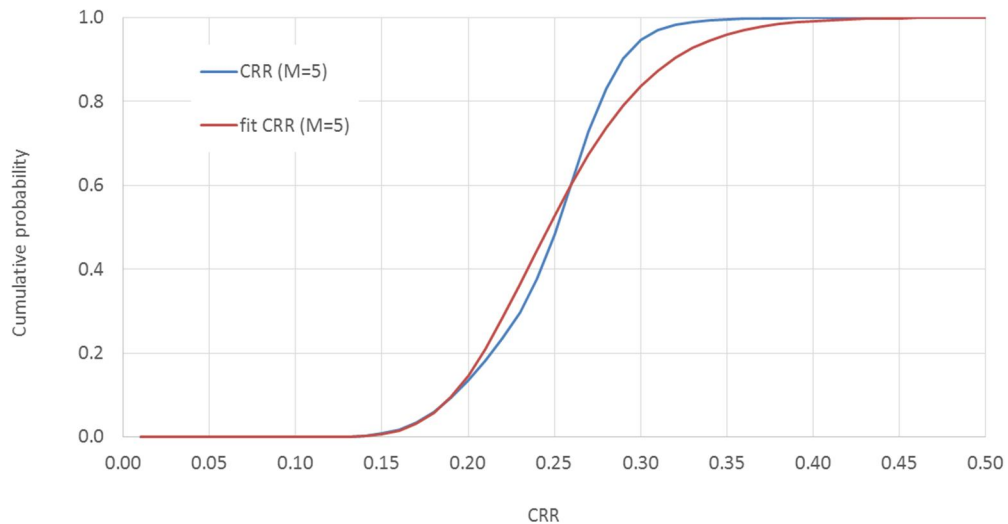


Figure 15. CRR for M=5, Delfzijl. Lognormal with $\mu = -1.4$ and $\sigma = 0.2$.

The CRR distribution for the laminated materials is compared with the typical curves calculated from laboratory tests and numerical modeling on Figure 16. The following observations are made.

- Non-laminated sand layers (i.e. Robertson Zone 6) appear to be present in no more than 2% of the CPT data collected in Delfzijl. Estimated CRR for the laminated materials is interpreted to be mostly above the liquefaction triggering results of non-laminated sand layers (i.e. Unit 8a, black curve on Figure 16).
- A ~60% cumulative probability is assigned to liquefaction triggering results from laminated samples with initial void ratios larger than 1 as shown on Figure 16 (CLP 60%). These samples with lower percentages of sands and higher percentages of clay are considered representative of the Delfzijl conditions.
- The triggering curve used for laminated samples with initial void ratios of about 0.8 (i.e. Unt 8b in Fugro's numerical evaluations, blue curve on Figure 13) is derived primarily from CSS tests on samples from Eemshaven borehole 38.0 where a larger percentage of sand is present within the laminated deposits (CLP=40% based on numerical simulation results) compared to Delfzijl explorations based on both CPT data and borehole sample descriptions. These resistances are interpreted to have a 36% quantile value.
- A 10% cumulative probability corresponds to the triggering curve derived from numerical simulation results of CDSS tests on laminated samples with CLP 10% (grey curve on Figure 13) since even a small percentage of clay laminations leads to an increase of liquefaction triggering resistance as was shown from numerical simulation results. This percentage of clay laminations is considered to be low for the conditions encountered at Delfzijl explorations.
- An approximately 85% cumulative probability is assigned to the resistance level based on numerical simulations of CDSS tests on laminated samples with CLP=70%.

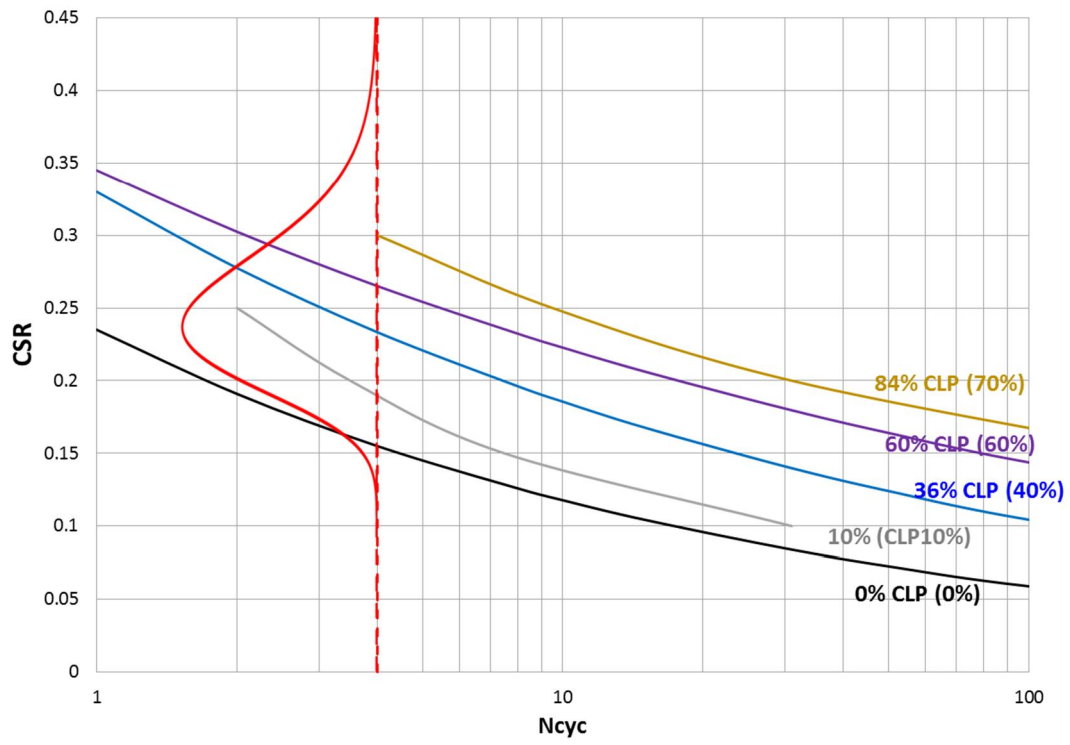


Figure 16. Quantile Values for the typical CRR curves.

REFERENCES

- Boulanger R. W., Meyers M. W., Mejia L. H. & Idriss I. M. (1998) "Behavior of a fine-grained soil during the Loma Prieta earthquake," Canadian Geotechnical Journal, Vol. 35, pp. 146-158.
- Donahue J. L., Bray J. D., and Riemer M. F. (2007) The Liquefaction Susceptibility, Resistance, and Response of Silty and Clayey Soils, U.S.G.S. Award Number: 05HQGR0009, November
- Fugro (2016a) Site investigation and Cyclic Laboratory Testing, Factual data report, Delfzijl / Eemshaven Levee Project in Groningen, the Netherlands, prepared for Nederlandse Aardolie Maatschappij B.V., November
- Fugro (2016b) Interpretive report, Delfzijl / Eemshaven Levee Project in Groningen, the Netherlands, prepared for Nederlandse Aardolie Maatschappij B.V., November
- Fugro (2016c) Evaluation of Dynamic Stability Eemshaven-Delfzijl Levee, the Netherlands, prepared for NAM, December 2016
- Sancio, R. B., Bray, J. D., Riemer, M. F. and Durgunoglu, T. (2003) "An assessment of the liquefaction susceptibility of Adapazari silt," 2003 Pacific Conference on Earthquake Engineering, Christchurch, New Zealand.
- Seed, H. B. and Peacock, W. H. (1971) "Test procedures for measuring soil liquefaction characteristics," Journal of Soil Mechanics and Foundations Division, ASCE, Vol. 97, No 8, pp. 1099-1119.

Appendix E Residual strength

Documented cases have shown that post-earthquake stability may be critical even if stability is ensured during shaking (e.g. Lower San Fernando dam case history).

Sand Layers. As mentioned in Fugro (2016a) post earthquake stability analyses were performed by assigning residual strength (i.e. defined as the ratio of residual undrained shear strength and in situ initial vertical effective stress, S_r/σ_{vc}') as a function of q_{c1Ncs} as proposed by Idriss and Boulanger (2008) for areas where the maximum excess pore pressure during shaking exceeded a specified threshold indicative of liquefaction. Fugro (2016a) considered that void redistribution effects could be significant and used the lower of the two curves plotted in Figure 28.

Since both the Cyclic Resistance Ratio (i.e. CRR) to liquefaction triggering and residual strength are a function of q_{c1Ncs} , this means that in general when CRR increases then the residual strength ratio S_r/σ_{vc}' should also increase and vice versa.

Laminated deposits within Unit 8. As discussed in Fugro (2016a) the presence of clay interlayers does create permeability contrasts that theoretically would allow for the development of void redistribution. However, given the limited thickness of the individual sand layers, the volume of water that could migrate upwards is limited. Moreover, Unit 8 is typically characterized by an overall low hydraulic conductivity, likely due to the limited lateral continuity and thickness of the sand sub-layers. In the absence of the ability for water inflow, the potential for suppression of dilation will be limited, and shear resistance will likely increase as shear strains exceed 5 to 15 percent. Additionally, due to the relatively low percentage of sand sublayers within the unit and the limited thickness of the sand sublayers, even the occurrence of relatively large shear strains (10 or 20%) within the layers will likely not result in large horizontal deformations prior to the development of dilation-induced shear resistance. Parametric numerical evaluations performed in Fugro (2016a) also point to the mitigating effect of thin layers in laminated deposits on the potential for void redistribution.

Despite the above we have conservatively used the residual strength defined above for sand layers also for the laminated soils. Since the CRR for the laminated soils is defined from laboratory test data, the residual strength for the laminated soils was estimated through a back-calculated q_{c1Ncs} . The value was backcalculated from the CRR value used for the laminated deposits in the FE analyses using the Boulanger and Idriss (2014) relationship.

A clear definition of the uncertainty in residual strength estimates is not available. For the purpose of these evaluations we have assumed that the uncertainty increases as the CRR (or q_{c1Ncs}) increases based on the fact that the recommended relationship by Idriss and Boulanger (2008) is extrapolated for larger q_{c1Ncs} values (i.e. dashed black lines in Figure 28 below). We have used a lognormal distribution to model the uncertainty on CRR with $\mu=0$ and $\sigma=0.15$. Figure 28 shows the resulting 95% confidence interval of residual strength ratios using the uncertainty term described above. The uncertainty is intended to cover both the range of data used to develop the empirical relationship as well as factors such as possible effects of mixing during large deformations etc.

An alternative probability distribution for residual strength based on Kramer and Wang (2015) was also considered in the FORM analyses. The Kramer and Wang (2015) probability distribution for residual strength is based on an empirical model consistent with steady-state concepts and behavior observed in laboratory tests and also calibrated on the basis of residual strengths back-calculated from flow-side case histories. The Kramer and Wang (2015) model predicts residual strengths as a function of normalized SPT blowcounts (N_{160}) and as a function of overburden stress. A comparison of the residual strength distributions considered in the FORM analyses is shown on Figure 28. Boulanger and Idriss (2008) relationship between N_{160} and q_{c1Ncs} was used to plot the residual strength proposed by Kramer and Wang (2015) as a function of normalized tip resistance. The residual strength curves plotted on Figure 28 from Kramer and Wang (2015) were derived for 1.5 atm overburden stress.

In order to account for the uncertainty on the conversion between N_{160} and q_{c1Ncs} the standard deviation considered in Kramer and Wang (2015) was increased from 0.37 (green curves) to 0.45 (red curves).

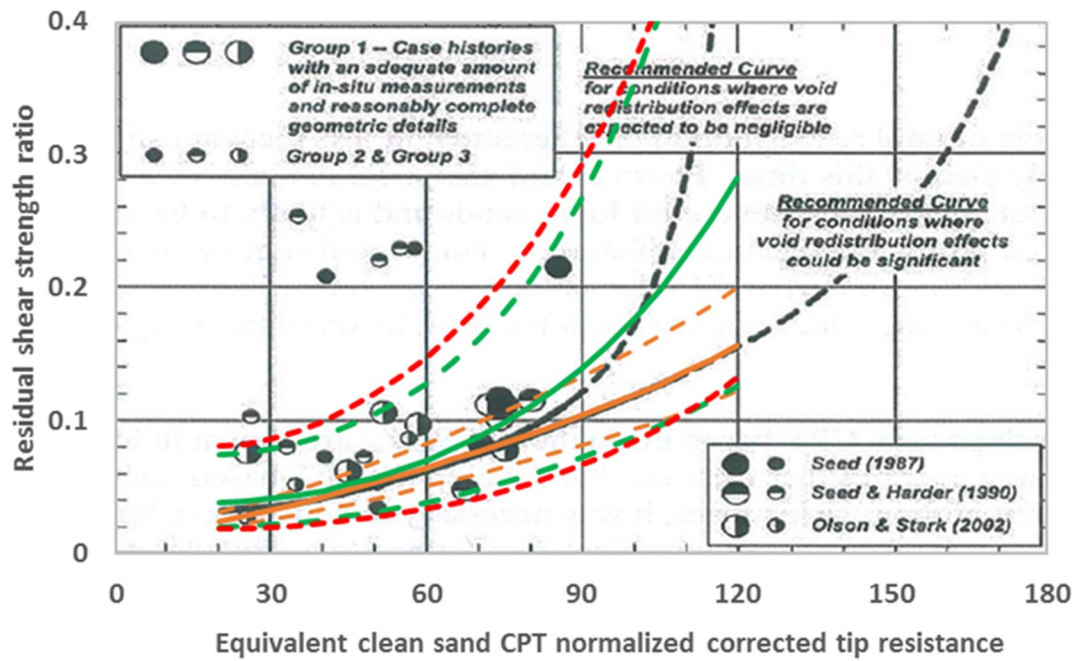


Figure 28. Uncertainty related to residual strength (95%-confidence interval) based on Kramer and Wang (2015) using the standard deviation proposed by the authors (green dashed curves) and an increased standard deviation of 0.45 (red dashed curves) to account for uncertainty in the conversion from $(N1)_{60}$ to q_{c1NCs} , and Idriss and Boulanger (2008) assuming void redistribution and engineering judgment for the estimation of standard deviation (orange curves).

Appendix F Model uncertainty

Two dimensional, effective-stress, dynamic analyses were performed using the finite difference code FLAC (Itasca 2011). Two different constitutive models were used to model the effective stress behavior of coarse-grained layers to account for epistemic uncertainty: UBCSand, developed by Professor Peter Byrne and his team at the University of British Columbia; and PM4Sand developed by Professor Ross Boulanger and Dr Katerina Ziotopoulou at UC Davis. Both constitutive models were calibrated against site-specific cyclic laboratory tests in order to capture soil triggering and strain accumulation behavior for both level (no-bias) and sloping ground (with static-bias) conditions. The reasonable comparison between observed and simulated behavior suggests that the calibrated constitutive models can be tailored to adequately simulate cyclic soil behavior at the element level both in terms of liquefaction triggering and in terms of post-liquefaction shear strain accumulation (Fugro 2016a).

In order to validate the constitutive models used for the liquefiable sands (i.e. determine the degree to which a model is an accurate representation of the real world from the perspective of the intended uses of the model) and evaluate the predictability of the implemented constitutive model at a system level, numerical simulations of real-scale boundary-value problems, such as case histories and centrifuge experiments, were performed and numerical results were compared with recorded measurements in the field and in the centrifuge, respectively. The case studies (case histories or centrifuge tests) used for validation involved liquefaction induced displacements of slopes and embankments founded on liquefiable layers in order to validate the ability of the two models to predict liquefaction induced deformations (Fugro 2016a).

Several “deterministic” sensitivity analyses have been carried out with two different constitutive models. Differences between computed crest settlements with PM4sand and UBCsand were found to be smaller than a factor 1.3 for all motions considered, for a given stratigraphy and return period Figure 29. Differences of about a factor 1.1-1.2 were found for 10 different stratigraphies (for a given motion and return period) and for 2 different return periods (for a given motion and 2 different stratigraphies), see Figure 30 and Figure 31.

As indicated in the expert panel report from December 3rd 2016 (Expert Panel 2016), with well-calibrated and validated constitutive models embedded in reliable numerical tools, dynamic effective stress analyses using multiple input motions can provide an indication of the range of expected levels of performance. They also allow evaluation of the sensitivity of response to various input parameters and modeling assumptions. It is important, however, to recognize potential uncertainties in constitutive models and numerical analyses. For critical projects, parallel analyses would ideally be performed using different constitutive models and different numerical tools. As described above, in Fugro (2016a) the computer code FLAC was used with two different calibrated and validated constitutive models to simulate the behavior of liquefiable sands. Ideally these analyses should be supplemented by parallel check analyses using a different computational tool (e.g., OpenSees with PDMY model or FLIP with cocktail glass model). Due to time constraints additional analyses with a different computational software have not been performed. To account for this we have introduced a model uncertainty term in the limit state function.

Considering the results of the “deterministic” sensitivity analyses, a model uncertainty distribution with $\mu_{ln(m)}=0$ and $\sigma_{ln(m)}=0.42$ would seem reasonable. However, considering the fact that sensitivity analyses have only been carried out with different constitutive models, but not with different software packages, a wider distribution has been assumed. We have assumed that the crest settlements estimated in Fugro (2016a) correspond to the mean value of observed settlements and that there is a 10% probability of exceedance of the predicted crest settlements by a factor of 2. The resulting model uncertainty function is a lognormal distribution with $\mu_{ln(m)}=0$ and $\sigma_{ln(m)}=0.55$ (Figure 32).

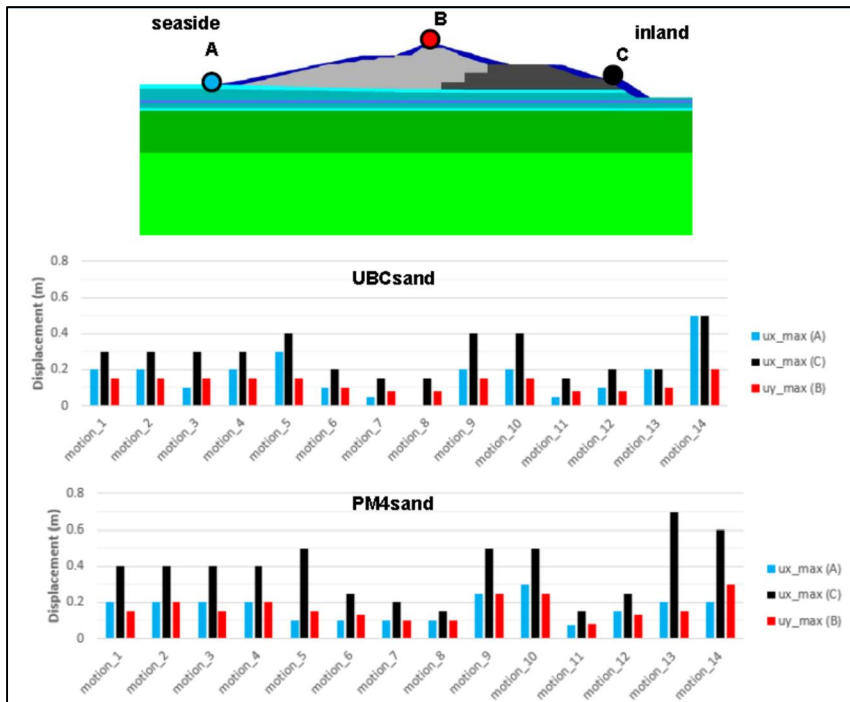


Figure 29. Calculated displacements with UBCsand and PM4sand for 14 different motions (Fugro 2016a: Figure 6-29b, page 42).

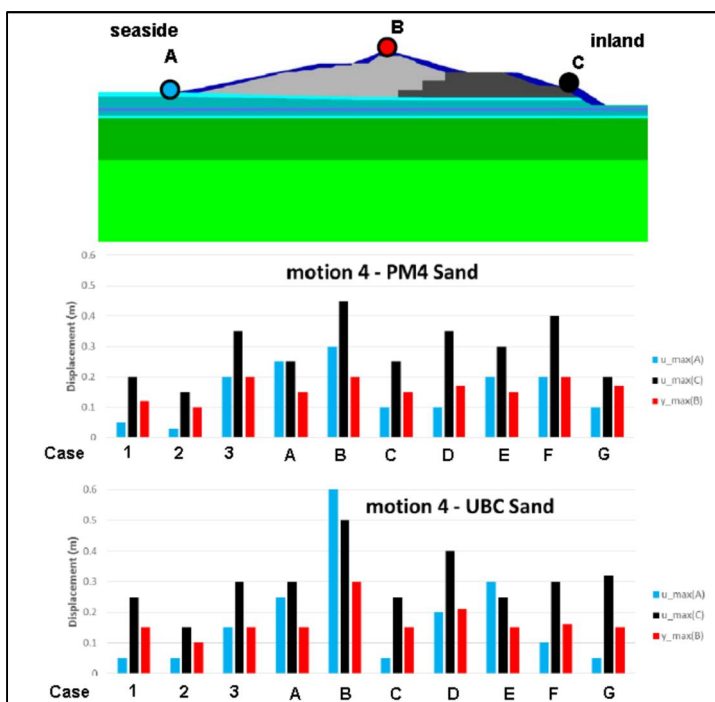


Figure 30. Calculated displacements with UBCsand and PM4sand for 10 different stratigraphies (Fugro 2016a: Figure 6-31b, page 45).

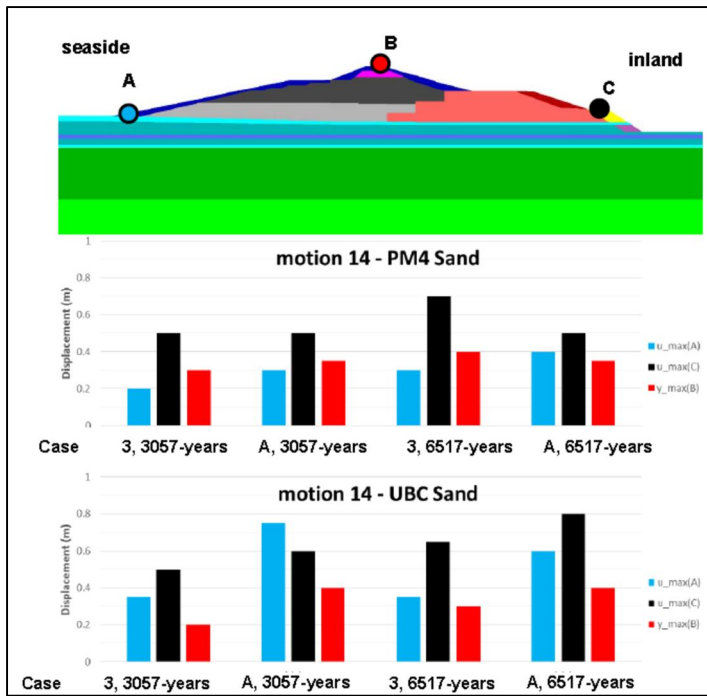


Figure 31. Calculated displacements with UBCsand and PM4sand for 2 different return periods, for 2 different stratigraphies (Fugro 2016a: Figure 6-32b, page 47).

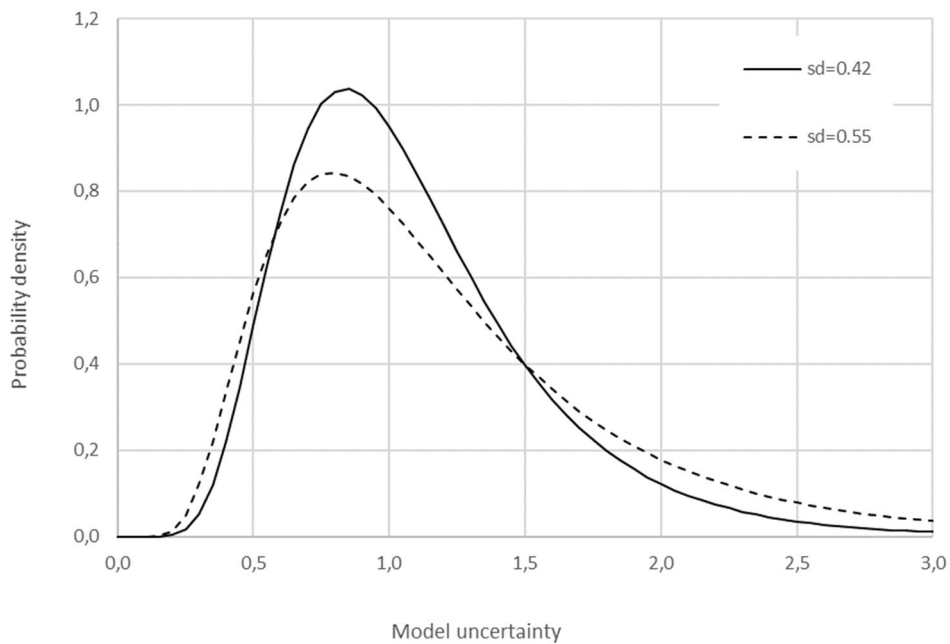


Figure 32. Model uncertainty: lognormal distributions for distribution parameters $\mu_{ln(x)}=0$ and $\sigma_{ln(x)}=0.42$, and $\mu_{ln(x)}=0$ and $\sigma_{ln(x)}=0.55$.

Appendix G Volume effects

Introduction

A laminated deposit consists of a series of alternating sand and clay layers. The resistance of the deposit to liquefaction depends on the composite behavior of these layers. Each lab test gives the resistance to liquefaction of a relatively small volume of laminated material.

Similarly, uniform sand deposits encountered at Eemshaven are characterized by a probability distribution of cyclic resistance based on q_{c1Ncs} values measured in uniform sands at Eemshaven (i.e. Unit 8a, see Fugro 2016c).

It is possible to fit numerous samples into the volume of Unit 8 that plays in a role in a seismic stability analysis. Layers of laminated material as well as sands without clay laminations of variable relative densities are treated as uniform in stability analyses (spatial variability within layers is not modelled explicitly). It is therefore important to specify the distribution that describes the uncertainty related to the composite behavior of such a larger volume of liquefiable material.

The uncertain resistance of such a larger volume (or the resistance of an “equivalent uniform layer”) is denoted by CRR in this Appendix. The uncertain resistance of a small volume (sample size) is denoted by \underline{CRR} . The difference between the distributions of CRR and \underline{CRR} is caused by the effects (“volume effects”) of spatial variability.

Spatial variability could turn out to be favorable, when local weakness are compensated by strengths elsewhere. It could, however, also turn out to be unfavorable, when local weaknesses dominate composite behavior:

1. In case of (only) a “weakest link/series system”-effect, the standard deviation of CRR will be smaller than the standard deviation of \underline{CRR} . The mean value of CRR will also be smaller than the mean value of \underline{CRR} .
2. In case of (only) spatial averaging, the standard deviation of CRR will be smaller than the standard deviation of \underline{CRR} , while the expected values of both variables will be the same (their median values could be different).
3. In case of (only) a “strongest link/parallel system”-effect, the standard deviation of CRR will be smaller than the standard deviation of \underline{CRR} but the mean value of CRR will be greater.

In normal slope stability analyses, some degree of spatial averaging of resistance properties over the slip plane is typically assumed (VanMarcke 1977; Calle & Barends 1990).

An approximate way of modelling the two types of spatial variability described above would be to model a layer as a composite of $n \times m \times p$ smaller volumes with random/uncertain resistances, denoted by $\underline{CRR}_{i,j,k}$, with $i=1..n$ and $j=1..m$ and $k=1..p$. This is shown schematically in Figure below. Each element in Figure has a resistance that can be described by the same distribution, but that can be different for each element. Note that it seems reasonable to assume that correlation distances are much smaller in a vertical direction than in the horizontal plane.

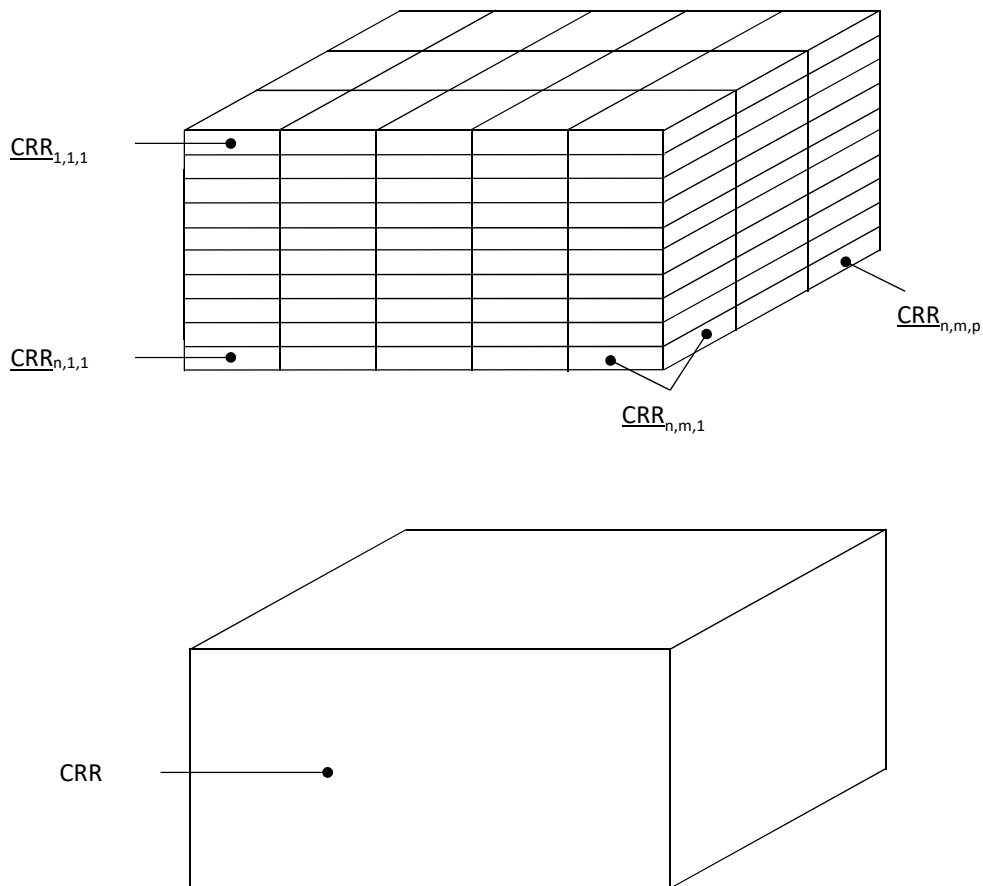


Figure 33. Illustration of a heterogeneous model and an equivalent uniform model.

The heterogeneous model shown in Figure 33 Figure merely serves an illustrative purpose. It would be too time-consuming to use it for deriving a distribution for CRR. Doing so could also easily yield a false sense of accuracy, since such an analysis would involve modelling assumptions that would themselves be highly uncertain (e.g. assumptions concerning the correlation structure).

Sensitivity analyses

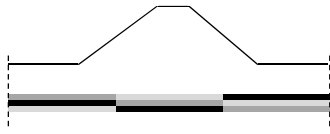
It is possible to get insight into volume effects from simplified numerical simulations. This can be done by comparing the computed crest settlements for a cross-section with uniform properties across a sand layer and a similar cross-section in which the layer has spatially variable properties. The following analyses have been performed (Figure 34):

1. An analysis in which the CRR varies in both a horizontal and vertical direction with 2 random assignments of CRR-values.
2. An analysis in which the CRR within a layer only varies along the vertical (horizontal continuity).

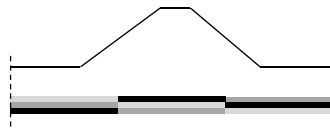
It is stressed that these cases are highly schematic: they do not accurately reflect reality. The spatial variations have not been constructed with a random fields model, as done by Montgomery & Boulanger (Montgomery 2015; Boulanger & Montgomery 2015; Boulanger & Montgomery 2016). Rather, 5%, 50% and 95% quantile values from the CRR-distribution have been assigned randomly within the liquefiable layer.

Analysis 1: Horizontal and vertical variability

Spatially variable model 1

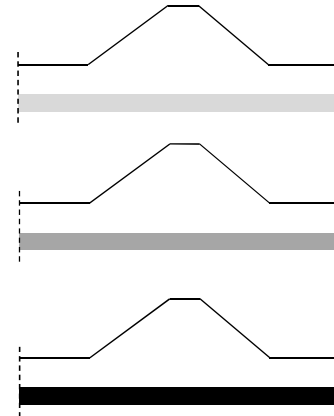


Spatially variable model 2



Laminated deposit

Uniform models



Analysis 2: Horizontal continuity

Vertically variable model

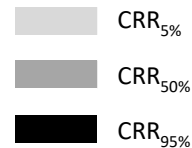
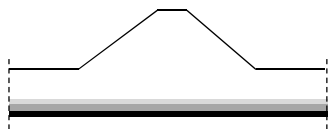


Figure 34. Sensitivity studies to get a feel for the effect of spatial variability within interlayered deposits.

Note that the effect of variability in the third dimension (perpendicular to this sheet of paper) cannot be dealt with in a 2D-model. It seems reasonable, however, to assume that variability in the third dimension reinforces the behavior observed in the 2D-sensitivity analysis.

Numerical models simulating the idealized schematizations shown in Figure 34 were developed for the evaluation of volume effects. Analyses were performed with the finite difference code FLAC. The UBCSand constitutive model was used to simulate the sand behavior. The model parameters were calibrated to cyclic resistances corresponding to 5% (pink line, Figure 35), 50% (blue line, Figure 35) and 95% (cyan line, Figure 35) of the CRR-distribution for uniform sands encountered at Eemshaven since this distribution results in lower (less favorable) cyclic resistance values compared to the distribution used for laminated deposits.

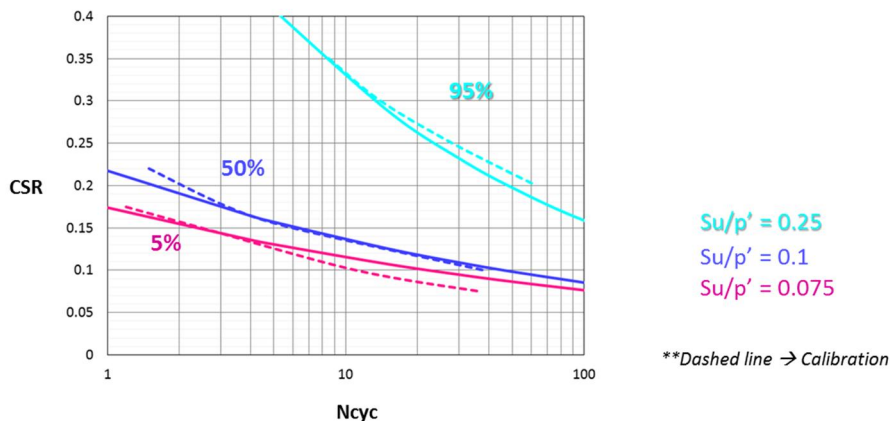


Figure 35. Calibrated constitutive model to different 5%, 50% and 95% percentiles of CRR for Eemshaven.

Analysis 1: Horizontal and vertical variability

The numerical models for the spatially variable case and the uniform case for Unit 8 are shown on Figure 36. Results of numerical evaluations of volume effects are shown in Figure 37 in the form of co-seismic and post-seismic crest settlements for the following cases:

- Model with spatial variability 1 in Unit 8 (upper-left illustration Figure 26)
- Model with spatial variability 2 in Unit 8 (mid-left illustration Figure 26)
- Uniform Unit 8 modeled with the 5% quantile value of CRR
- Uniform Unit 8 modeled with the 50% quantile value of CRR
- Uniform Unit 8 modeled with the 95% quantile value of CRR

As shown in Figure 37, the spatially variable Unit 8 properties result in decreased crest settlements compared to the cases where Unit 8 properties are uniformly modeled using 5% and 50% quantile CRR values. It is worth noting that the both models with spatial variability 1 and 2 give similar results.

Analysis 2: Horizontal continuity / Vertical Variability

The numerical model for the vertically variable case (where horizontal continuity is maintained) is shown in Figure 36 (bottom). As shown in the graph of Figure 37, the vertical variability in the properties of Unit 8 leads to crest settlements similar to the case where Unit 8 properties are uniformly modeled using 50% quantile CRR values.

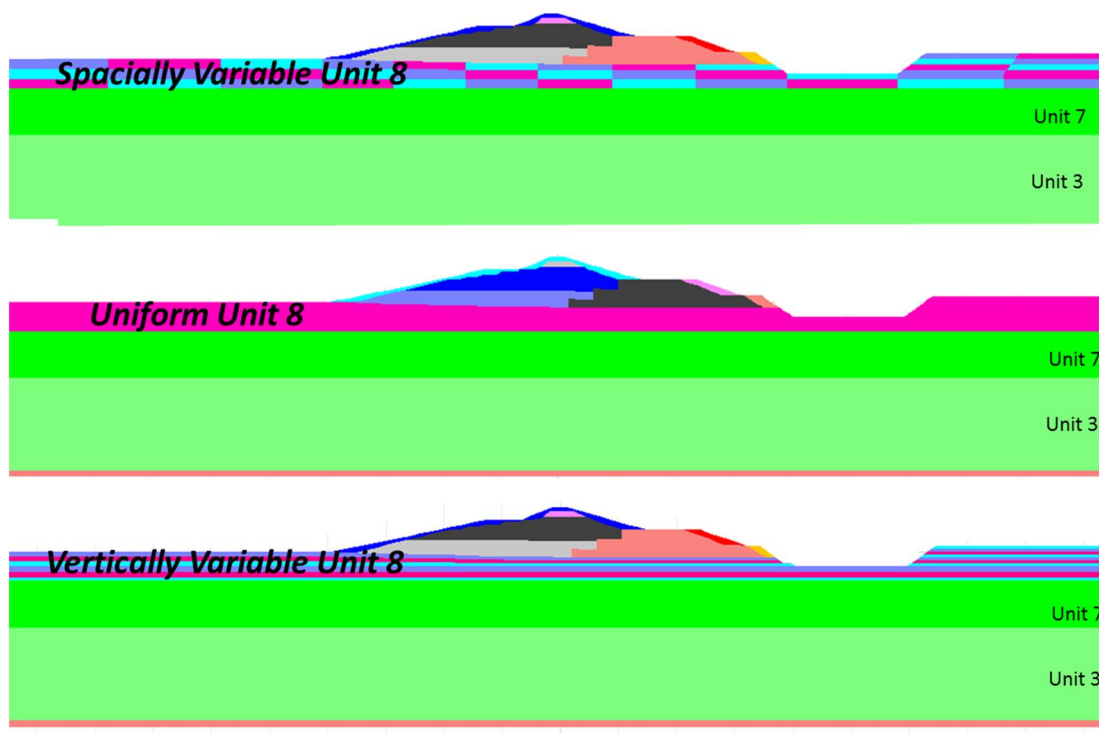


Figure 36. Numerical Models for Assessment of Spatial Variability of Unit 8.

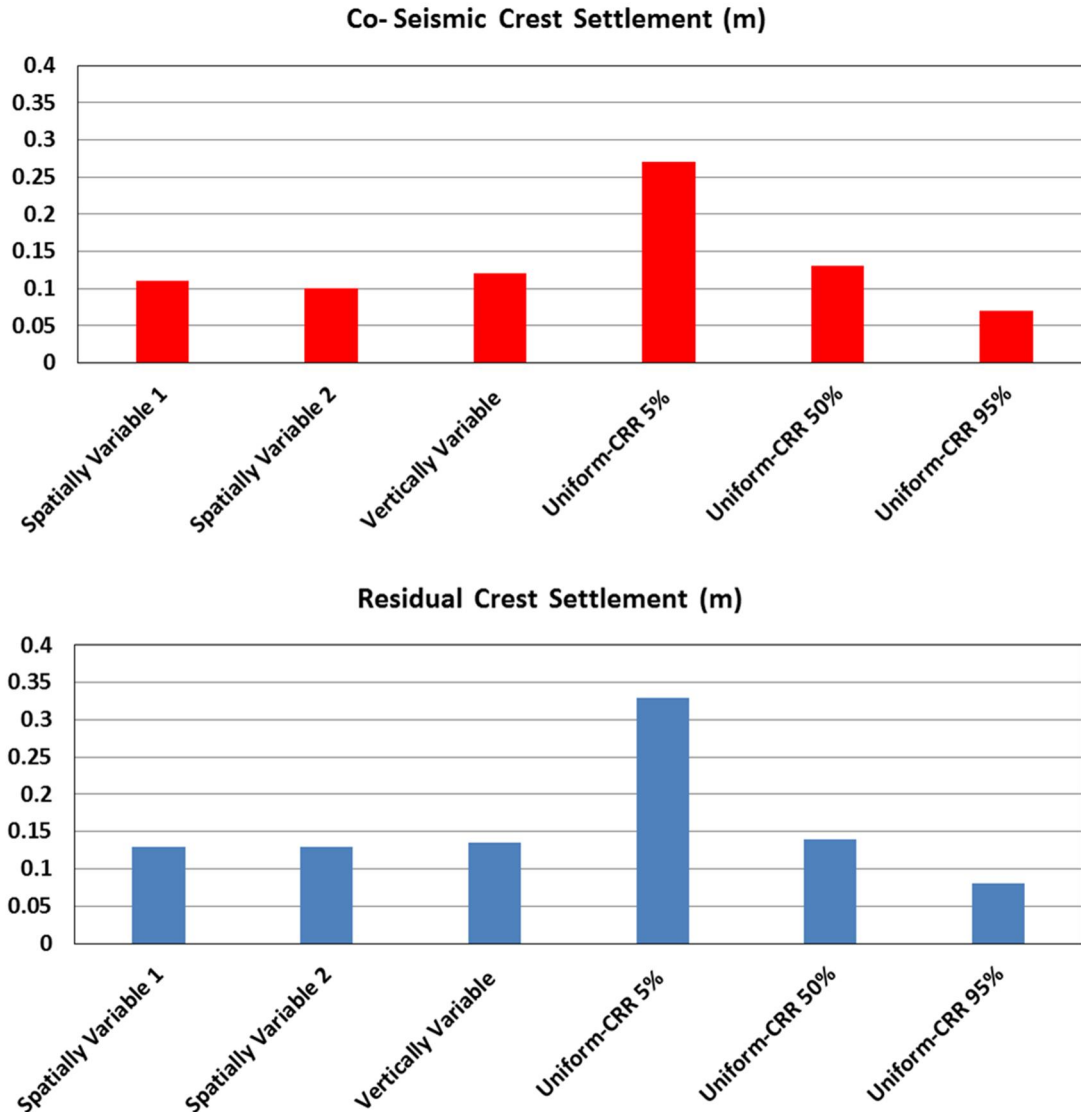


Figure 37. Estimated crest settlements using spatially variable and uniform properties for Unit 8.

Discussion

The results shown in Figure 37 indicate that spatially averaged CRR-values should be used in a uniform model to mimic the results of a model in which the spatial variability of CRR-values within deposits is modelled explicitly (a random fields model). This finding is in line with a comparison between numerical analyses using a random fields model and a uniform model performed for a dam by Boulanger & Montgomery (2016). In this case study, a random fields model with a coefficient of variation of $(N_1)_{60cs}$ of 0,4 and a scale of fluctuation in of 20 m horizontally and 1 m vertically was compared to a uniform model. The case study concerned large deformations, as is the case here. Boulanger & Montgomery (2016) recommend a 33rd percentile value for use in deterministic analyses (conservative) and a range of 30-70% in risk assessments.

The abovementioned sensitivity analyses and more detailed case study all assumed that the uncertainty related to the cyclic resistance ratio or $(N_1)_{60cs}$ can be attributed to fluctuations of point values relative to a spatial average or median value. In case of a regional data set, i.e. a data set that consists of measurements from various locations (or case histories), the local average or median can be uncertain as well. This part of the variance should not be treated as spatially variable in a cross-sectional reliability analysis. Considering this, the uncertainty related to a local average may be expressed as follows (after TAW 2001):

$$\sigma_x = \sigma_x \cdot \{ (1-\omega) + \omega \cdot \Omega^2 \}^{1/2} \tag{35}$$

Where:

- σ_x Standard deviation of the spatial average of stochastic variable X (-)
- ω Part of the total variance that can be attributed to fluctuations of point values relative to the local average (-)
- Ω Variance reduction factor (-); $0 \leq \Omega \leq 1$

Recommended $CRR_{M=5,0}$ -distribution for laminated deposits for use in a uniform model

Based on the results of the sensitivity analyses and the case study by Boulanger & Montgomery (2016), a variance reduction factor Ω of 0 seems reasonable. Note: the average of a lognormally distributed variable is higher than its median value. The difference is negligible however, for the distribution of the CRR for laminated deposits (a factor 1.02). This means that the distribution of the local average is almost identical to the distribution of the local median.

Since the CRR -distribution for laminated deposits is based on a regional data set, i.e. samples taken at various locations, a value of ω of 0.75 is proposed here. This value is in line with Dutch engineering practice for dealing with regional data sets in slope stability assessments (e.g. TAW 1989: page 90; TAW 2001: page 254), see also Calle (2007; 2008) for a statistical basis/interpretation.

The distributions of the point values and the local medians of the cyclic resistance ratio of a laminated deposit are given in Table 12. These distributions are shown in Figure 38.

Table 12. Distributions of cyclic resistance ratios for laminated deposits. Both distributions rest on a regional data set.

Variable	Symbol	Distribution type	Parameter values
Point value of CRR (unsuitable for use in a uniform model)	\underline{CRR}	Lognormal	$\mu_{\ln(CRR)} = -1.4$ $\sigma_{\ln(CRR)} = 0.2$
Local average of CRR	CRR	Lognormal	$\mu_{\ln(CRR)} = -1.39$ $\sigma_{\ln(CRR)} = 0.1$

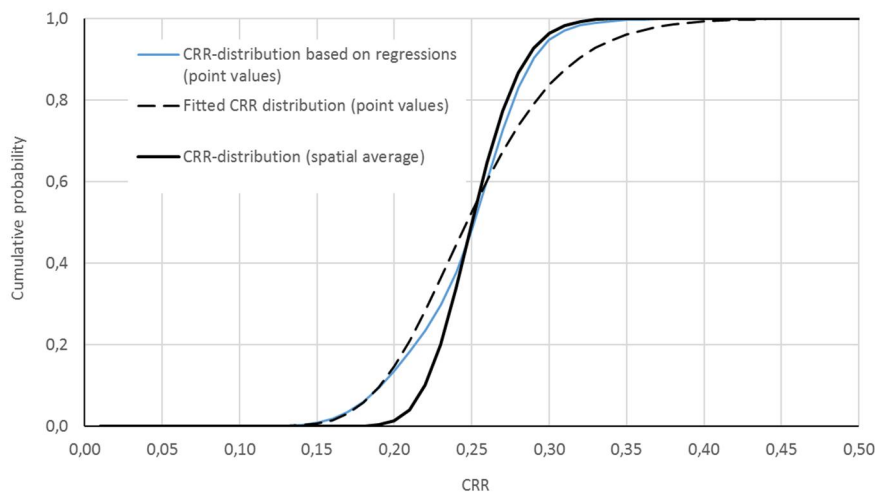


Figure 38. Cyclic resistance ratio for laminated deposits.

Recommended $CRR_{M=7.5}$ -distribution for sand deposits for use in a uniform model

The distribution of point values of q_{c1Ncs} for any given layer rests a local CPT data, i.e. a local data set. Within a local data set, regional variations are small. This implies $\omega \approx 1$ in equation (35) (see also TAW 1989, TAW 2001). Based on the results of the sensitivity analyses and the case study by Boulanger & Montgomery (2016) (that all essentially rest on the assumption $\omega=1$), the use of the median of q_{c1Ncs} from the local data set is recommended (not the mean; the median could be about 10% smaller). This means that the distribution of $CRR_{M=7.5}$ for sand deposits for use in a uniform model follows directly from the median of local q_{c1Ncs} -values and the probabilistic relationship between the cyclic resistance ratio and q_{c1Ncs} of Boulanger and Idriss (2014).

The distributions of the point values and the local medians of the cyclic resistance ratio of a sand deposit are given in Table 13. These distributions are shown in Figure 39.

Table 13. Distributions of cyclic resistance ratios for sand deposits.

Stochastic variable	Symbol	Distribution type	Parameter values
Point value of CRR in the local data set (unsuitable for use in a uniform model)	\underline{CRR}	Lognormal	$\mu_{\ln(\underline{CRR})} = -1.88$ $\sigma_{\ln(\underline{CRR})} = 0.22$
Local median of CRR	CRR	Lognormal	$\mu_{\ln(CRR)} = -1.88$ $\sigma_{\ln(CRR)} = 0.20$
Point value of CRR in the regional data set (unsuitable for use in a uniform model; used in sensitivity analyses because the distribution is relatively wide)	\underline{CRR}	Lognormal	$\mu_{\ln(\underline{CRR})} = -1.80$ $\sigma_{\ln(\underline{CRR})} = 0.30$

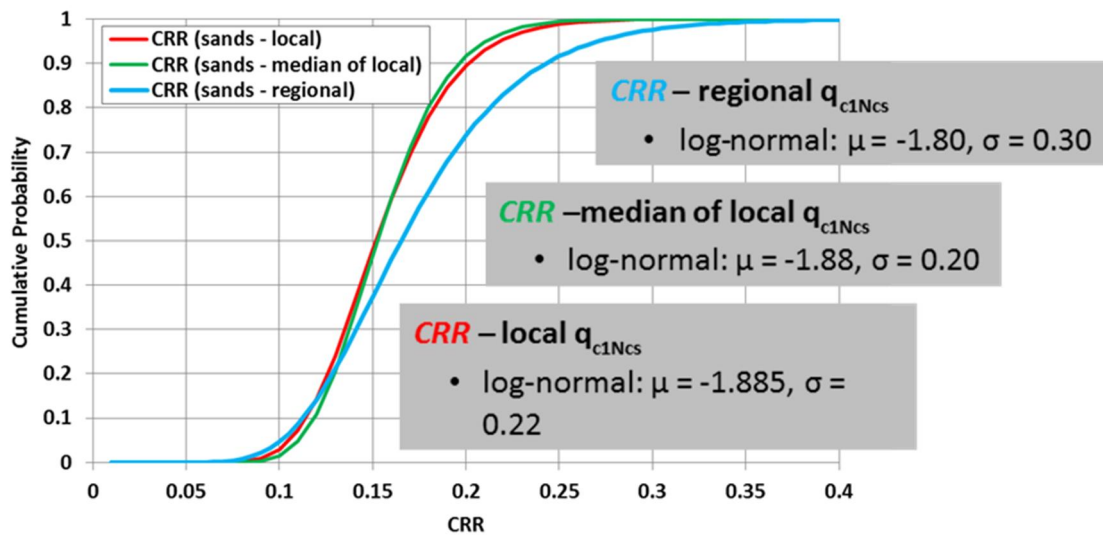


Figure 39. Cyclic resistance ratio for sand deposits.

The left-hand tail of the distribution for point values of q_{c1Ncs} is largely determined by the uncertainty in the Boulanger & Idriss (2014)-relationship, as shown by the FORM influence coefficients (Figure 40). This explains why the left-hand tails of the distributions for point values and the median of q_{c1Ncs} are rather similar. This means that the assumption of $\omega \approx 1$ in equation (35) hardly influences the results of FORM-analyses and semi-probabilistic assessments.

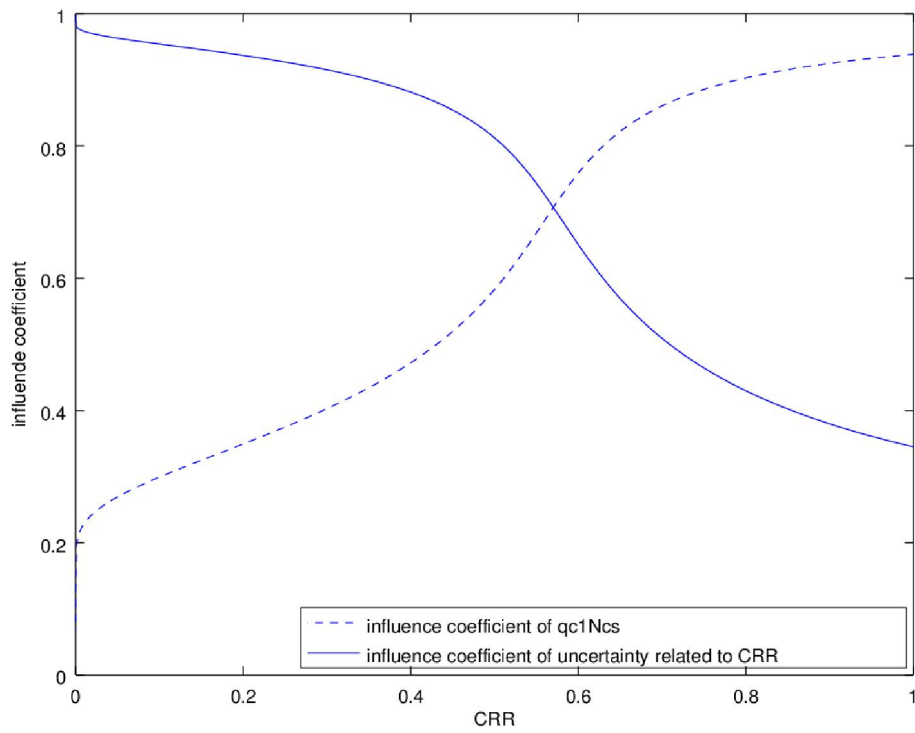


Figure 40. FORM-influence coefficients for the convolution of local point values of q_{c1Ncs} and the uncertainty in the Boulanger & Idriss (2014) relationship.

Appendix H Uncertainty related to motions

Computed displacements depend on the selected ground motion (spectrally matched to the target design spectrum). This is because matched motions have different characteristics such as duration and velocity pulses. This uncertainty cannot easily be modelled by continuous stochastic variables. This can be dealt with in a simpler manner by conditioning computed deformations and failure probabilities on motions, and to consider the subjective probabilities (“degrees of belief”) associated with each motion. This is discussed below.

Theory

Consider a set of $i=1..n$ motions that spans all possible motions. Probabilities of failure could be calculated for each given motion. The probability of failure then equals:

$$P(F) = \sum P(F | M_i) \cdot P(M_i) \quad (36)$$

Where:

$P(F)$ Probability of failure (per year)

$P(F | M_i)$ Probability of failure given motion i (per year), $i=1..n$. A motion is thought of here as a “basic” time series that can be scaled to whatever spectral acceleration. This, however, is an oversimplification. When motions are matched to a particular spectrum, their durations are held constant, even though motions should have shorter durations for higher accelerations in the Groningen area. This is an important reason why the selection of “basic” motions should depend on the target design spectrum. This issue is discussed at the end of this section.

$P(M_i)$ Probability of motion i (-). Note that $\sum P(M_i)=1$. The motions M_i are mutually exclusive, collectively exhaustive.

In a probabilistic assessment, the failure probabilities for the different motions could be obtained from e.g. MC or FORM-analyses. These could then be combined with the probabilities assigned to each motion into a probability of failure, $P(F)$. This failure probability could then be compared to the target failure probability, P_r .

In a semi-probabilistic assessment, the following procedure could be followed (in line with the procedure described in ENW 2012), i.e.:

1. For each motion:
 - a. Vary the target reliability index (or target failure probability) and compute the associated design values, using a functional relationship between reliability indices and design values (see equation (3))
 - b. Select the target reliability index for which a calculation with the design values from step 1a just leads to the critical crest settlement (limit state function equal to zero).
 - c. Calculate the probability of failure associated with the reliability index from step 1b.
 - d. Multiply the probability of failure from step c with the probability of the motion under consideration.
2. Take the sum of the results from step 1. This is an estimate of the probability of failure (see equation (36)).
3. Compare the estimate of the probability of failure from step 2 to the target failure probability.

The procedure described above is theoretically correct but impractical since it involves a large number of evaluations of the limit state function.

Pragmatic way forward

The number of evaluations could be strongly reduced if we were able to identify a motion M_d for which the following holds:

$$P(F) \leq P(F | M_d) \quad (37)$$

Obviously, taking the most conservative motion ($M_d = M_n$), would certainly satisfy the condition given by equation (37). This, however, would also be highly conservative.

To be able to define the design motion in probabilistic terms, we could order the motions on the basis of their conditional failure probabilities, with motion 1 having the smallest failure probability and motion n the highest, i.e.

$$P(F | M_i) \leq P(F | M_w) \quad \text{with} \quad i < w \quad (38)$$

The following procedure is suggested for dealing with the uncertainty related to motions:

1. Select independent motions with appropriate seismological characteristics, including duration.
2. Compute crest settlements for each motion (semi-probabilistically). This is an important step because it is difficult to predetermine which motion gives the greatest deformation.
3. Analyze the results: outliers should be understood.
4. A slightly conservative motion should be treated as representative, which could be interpreted as a motion an “exceedance probability” of 20% (see below).

Note that it might be incorrect to treat the motions being considered as equally likely or to assume that the 11 selected motions span the entire set of possible motions. In some cases, it might be reasonable to assign low subjective probabilities to particular motions or to treat the set of motions as a subset of relatively pessimistic scenarios. This means that M_d need not be a conservative motion within the set of motions being considered.

Even when the differences between the failure probabilities for different motions are substantial, a motion with an “exceedance probability” in of 20% is still likely to be sufficiently conservative, even when the failure probabilities per motion differ substantially. To illustrate this, consider the following purely hypothetical examples.

Case 1

Consider 4 equally probable motions, each with a different (conditional) failure probability. The “overall” failure probability equals $1,875 \cdot P_0$ (Table 14). This is smaller than $P(F | M_3)$, which implies that motion 3 could be used as a basis for a simplified assessment. This is a motion with a cumulative probability of 75%, or an “exceedance probability” of 25%.

Table 14. Hypothetical case 1: four equally likely motions with associated failure probabilities that differ up to a factor 8.

Motion	$P(M_i)$	Cumulative probability	$P(F M_i)$	$P(M_i) \cdot P(F M_i)$
1	1/4	1/4	$1/2 \cdot P_0$	$1/8 \cdot P_0$
2	1/4	2/4	P_0	$1/4 \cdot P_0$
3	1/4	3/4	$2 \cdot P_0$	$1/2 \cdot P_0$
4	1/4	1	$4 \cdot P_0$	P_0
Sum	1	-	-	$1,875 \cdot P_0$

Case 2

Consider 11 equally probable motions, with (conditional) failure probabilities that increase exponentially. The smallest and highest failure probabilities differ by a factor 100. The “overall” failure probability equals $24,48 \cdot P_0$ (see Table 15). Here, the “design motion” has a cumulative probability of 8/11, or an “exceedance probability” of 27%.

Table 15. Hypothetical case 2: four equally likely motions with associated failure probabilities that differ up to a factor 100.

Motion	$P(M_i)$	Cumulative probability	$P(F M_i)$	$P(M_i) \cdot P(F M_i)$
1	1/11	1/11	$1,00 \cdot P_0$	$0,09 \cdot P_0$
2	1/11	2/11	$1,58 \cdot P_0$	$0,14 \cdot P_0$
3	1/11	3/11	$2,51 \cdot P_0$	$0,23 \cdot P_0$
4	1/11	4/11	$3,98 \cdot P_0$	$0,36 \cdot P_0$
5	1/11	5/11	$6,31 \cdot P_0$	$0,57 \cdot P_0$
6	1/11	6/11	$10,00 \cdot P_0$	$0,91 \cdot P_0$

7	1/11	7/11	15,85 · P ₀	1,44 · P ₀
8	1/11	8/11	25,12 · P ₀	2,28 · P ₀
9	1/11	9/11	39,81 · P ₀	3,62 · P ₀
10	1/11	10/11	63,10 · P ₀	5,74 · P ₀
11	1/11	1	100,00 · P ₀	9,09 · P ₀
Sum				24,48 · P ₀

The use of motions with a fixed duration in FORM-analyses

The same (scaled) motion (motion 4) has been used in the FORM-analyses. For the relatively low exceedance probability of the design point value of the spectral acceleration, a motion with a shorter duration than the duration of motion 4 would have been appropriate (e.g. 1.5 seconds rather than 4.2 seconds). The fact that duration has not been adjusted has led to overestimation of the probability of failure (conservatism). This, however, is largely irrelevant for our purposes. More important is that it has also led to overestimation of the relative importance of the uncertainty related to the spectral acceleration of the model base, i.e. overestimation of $\alpha_{SAmodel_base}^2$ (and underestimation of the squared other influence coefficients). This is because it has “fattened the tail of the load distribution”. When deciding on design values, this has to be kept in mind.

Figure 41 plots significant duration (D5-75) and cumulative absolute velocity (CAV) estimates of the 11 motions used for the design basis case for Eemshaven section presented in the LPI-screening report (Deltares 2017) versus post-seismic crest settlements. The estimated significant duration for a 3057-year return period event using Bommer et al. (2015) empirical correlation for Groningen is 3.8 seconds. For the FORM analysis, motion 4 was considered representative of the entire suite of 11 motions. Motion 6 was considered in a sensitivity analysis.

Figure 42 plots significant duration (D5-75) and cumulative absolute velocity (CAV) estimates of the 11 motions used for the design basis case for Delfzijl section presented in the LPI-screening report (Deltares 2017) versus post-seismic crest settlements. The estimated significant duration for a 6537-year return period event using Bommer et al (2015) empirical correlation for Groningen is 3.6 seconds. For the FORM analysis, motion 4 was considered representative of the entire suite of 11 motions. Motion 6 was considered in a sensitivity analysis.

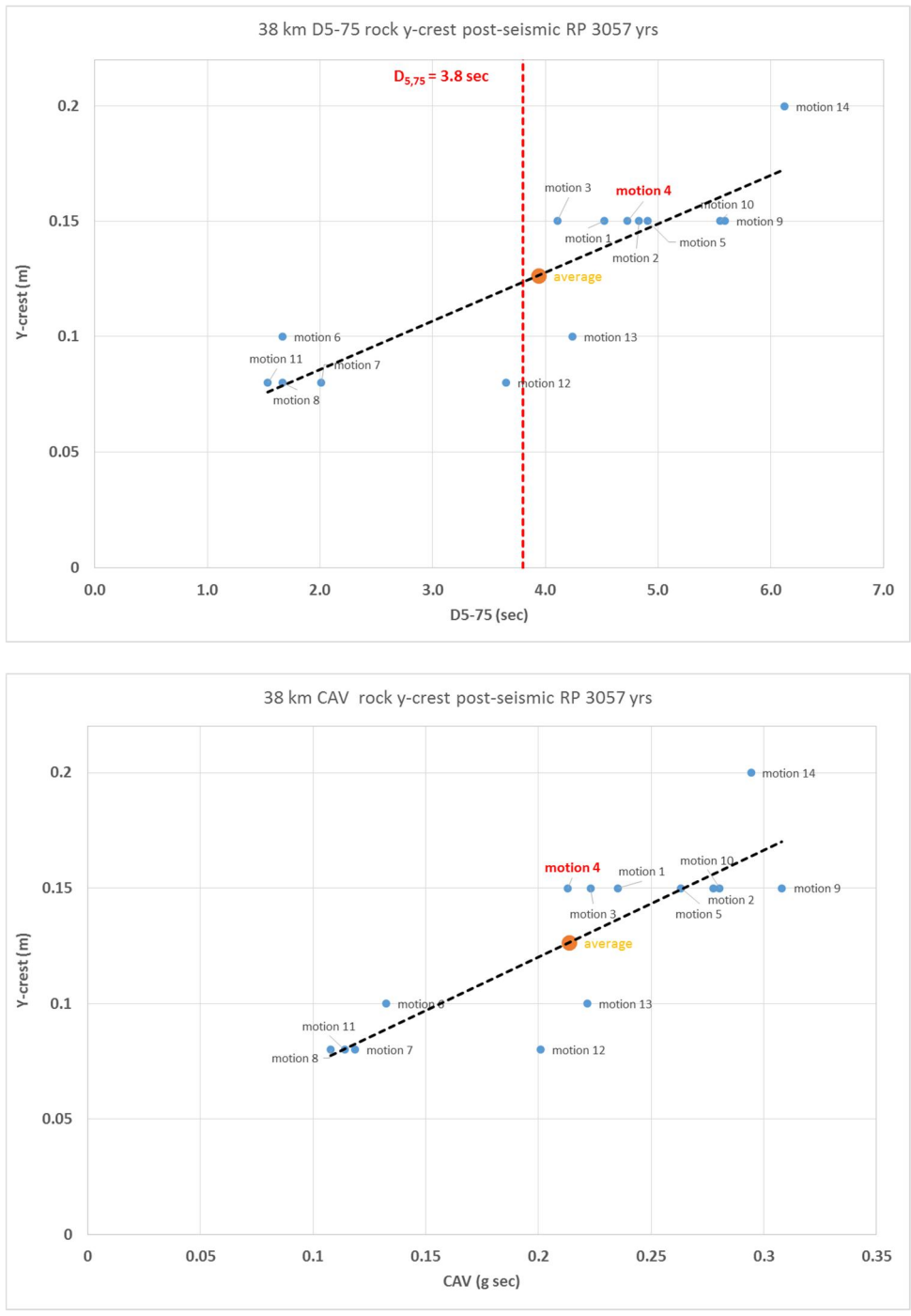


Figure 41. Range of crest settlements versus significant duration (upper illustration) and cumulative absolute velocity (lower illustration) from 14 different ground motions for Eemshaven Design Basis Case (Deltares 2017).



Figure 42. Range of crest settlements versus significant duration (upper illustration) and cumulative absolute velocity (lower illustration) from 14 different ground motions for Delfzijl Design Basis Case (Deltares 2017).

Appendix I Results of FORM-analyses for the 2D finite elements model

An overview of the results of the FORM-analyses are in the tables below. Prior to the FORM-iterations shown in these tables, at least 15 iterations were carried out.

Table 16. Results of FORM-analyses for Eemshaven profile using the median of local q_{c1NCS} data [Base case A : Su/p' according to Kramer & Wang (2015); ground motion 4]

No.	Sa [g] (= e^{x1})	CRR [-] (= e^{x2})	$\epsilon Su/p'$ [-] (= e^{x3})	m [-] (= e^{x4})	Z [m]	$\partial Z/\partial x_1$	$\partial Z/\partial x_2$	$\partial Z/\partial x_3$	$\partial Z/\partial x_4$	μ_Z	σ_Z	Beta	α_{x1}^2	α_{x2}^2	α_{x3}^2	α_{x4}^2	x_{1d}	x_{2d}	x_{3d}	x_{4d}
0	0.450	0.100	0.700	2.000	0.148	-5.310	10.677	3.540	-2.999	30.630	6.120	5.005	0.738	0.122	0.068	0.073	-0.794	-2.224	-0.586	0.742
1	0.450	0.102	0.669	2.020	0.137	-5.418	11.790	3.153	-3.011	31.418	6.252	5.025	0.736	0.142	0.052	0.070	-0.782	-2.254	-0.513	0.732
2	0.452	0.102	0.654	2.032	0.114	-5.484	12.409	3.016	-3.035	31.914	6.345	5.030	0.732	0.153	0.046	0.069	-0.790	-2.268	-0.484	0.728
3	0.452	0.102	0.646	2.039	0.093	-5.543	12.717	2.958	-3.057	32.280	6.417	5.030	0.731	0.157	0.043	0.069	-0.792	-2.274	-0.470	0.725
4	0.452	0.103	0.642	2.044	0.075	-5.589	12.885	2.934	-3.076	32.547	6.470	5.031	0.731	0.159	0.042	0.068	-0.791	-2.276	-0.462	0.724
5	0.453	0.103	0.640	2.048	0.061	-5.623	12.987	2.927	-3.091	32.743	6.508	5.031	0.732	0.159	0.041	0.068	-0.790	-2.277	-0.458	0.723
6	0.453	0.103	0.638	2.050	0.049	-5.649	13.056	2.927	-3.103	32.889	6.537	5.031	0.732	0.160	0.041	0.068	-0.790	-2.277	-0.456	0.722
7	0.453	0.103	0.637	2.052	0.040	-5.668	13.105	2.930	-3.113	33.000	6.560	5.031	0.732	0.160	0.040	0.068	-0.789	-2.277	-0.455	0.722
8	0.453	0.103	0.637	2.053	0.032	-5.683	13.142	2.934	-3.121	33.087	6.577	5.031	0.732	0.160	0.040	0.068	-0.789	-2.277	-0.454	0.722
9	0.453	0.103	0.636	2.055	0.026	-5.695	13.171	2.938	-3.128	33.155	6.590	5.031	0.732	0.160	0.040	0.068	-0.789	-2.277	-0.454	0.722
10	0.454	0.103	0.636	2.055	0.021	-5.704	13.193	2.941	-3.133	33.210	6.601	5.031	0.732	0.160	0.040	0.068	-0.789	-2.277	-0.454	0.722
11	0.454	0.103	0.636	2.056	0.017	-5.712	13.210	2.945	-3.137	33.253	6.610	5.031	0.732	0.160	0.040	0.068	-0.789	-2.277	-0.454	0.722
12	0.454	0.103	0.636	2.057	0.014	-5.718	13.224	2.947	-3.140	33.288	6.616	5.031	0.732	0.160	0.040	0.068	-0.789	-2.277	-0.454	0.722
13	0.454	0.103	0.636	2.057	0.011	-5.722	13.235	2.950	-3.143	33.316	6.622	5.031	0.732	0.160	0.040	0.068	-0.789	-2.277	-0.454	0.722

The design point has been verified using the FEM analysis. The final step of FORM analysis based on the response space results to a crest settlement of 1.45 m, the calculated crest settlement from FEM analysis is 1.50 m. A final FORM iteration using numerical analyses leads to similar influence factors (α_i^2), as shown in the table below.

No.	Sa [g] (= e^{x1})	CRR [-] (= e^{x2})	$\epsilon Su/p'$ [-] (= e^{x3})	m [-] (= e^{x4})	Z [m]	$\partial Z/\partial x_1$	$\partial Z/\partial x_2$	$\partial Z/\partial x_3$	$\partial Z/\partial x_4$	α_{x1}^2	α_{x2}^2	α_{x3}^2	α_{x4}^2
final	0.454	0.103	0.636	2.057	-0.085	-6.171	13.371	3.085	-3.245	0.753	0.144	0.039	0.064

Table 17. Results of FORM-analyses for the Delfzijl profile with spatial averaging [Base case B : Su/p' according to Kramer and Wang (2015); ground motion 4]

No.	Sa [g] (=e ^{x1})	CRR [-] (=e ^{x2})	eSu/p' [-] (=e ^{x3})	m [-] (=e ^{x4})	Z [m]	$\partial Z/\partial x_1$	$\partial Z/\partial x_2$	$\partial Z/\partial x_3$	$\partial Z/\partial x_4$	μ_Z	σ_Z	Beta	α_{x1}^2	α_{x2}^2	α_{x3}^2	α_{x4}^2	x _{1d}	x _{2d}	x _{3d}	x _{4d}
0	1.100	0.220	0.700	3.000	-0.016	-4.160	9.747	1.325	-3.171	24.766	4.505	5.497	0.786	0.047	0.018	0.150	0.058	-1.509	-0.327	1.171
1	1.092	0.220	0.704	3.044	-0.012	-4.157	9.708	1.331	-3.168	24.748	4.502	5.497	0.786	0.047	0.018	0.150	0.059	-1.509	-0.329	1.170
2	1.086	0.220	0.707	3.079	-0.010	-4.155	9.680	1.336	-3.165	24.732	4.499	5.497	0.786	0.046	0.018	0.150	0.059	-1.508	-0.330	1.170
3	1.081	0.221	0.709	3.107	-0.008	-4.152	9.660	1.338	-3.163	24.716	4.496	5.498	0.786	0.046	0.018	0.150	0.059	-1.508	-0.331	1.170
4	1.077	0.221	0.711	3.129	-0.006	-4.150	9.645	1.340	-3.161	24.703	4.493	5.498	0.786	0.046	0.018	0.150	0.060	-1.508	-0.332	1.170
5	1.074	0.221	0.712	3.148	-0.005	-4.148	9.635	1.342	-3.160	24.692	4.491	5.498	0.786	0.046	0.018	0.150	0.060	-1.508	-0.333	1.170
6	1.071	0.221	0.713	3.162	-0.004	-4.147	9.627	1.342	-3.159	24.682	4.490	5.498	0.786	0.046	0.018	0.150	0.060	-1.508	-0.333	1.170
7	1.069	0.221	0.714	3.174	-0.003	-4.145	9.621	1.343	-3.158	24.675	4.488	5.498	0.786	0.046	0.018	0.150	0.060	-1.508	-0.333	1.170
8	1.068	0.221	0.715	3.184	-0.002	-4.144	9.617	1.343	-3.157	24.668	4.487	5.498	0.786	0.046	0.018	0.150	0.059	-1.508	-0.333	1.170
9	1.066	0.221	0.715	3.192	-0.002	-4.143	9.613	1.343	-3.157	24.663	4.486	5.498	0.786	0.046	0.018	0.150	0.059	-1.508	-0.333	1.170
10	1.065	0.221	0.715	3.198	-0.001	-4.143	9.611	1.343	-3.156	24.659	4.485	5.498	0.786	0.046	0.018	0.150	0.059	-1.508	-0.333	1.170
11	1.065	0.221	0.716	3.203	-0.001	-4.142	9.609	1.344	-3.156	24.656	4.485	5.498	0.786	0.046	0.018	0.150	0.059	-1.508	-0.334	1.170
12	1.064	0.221	0.716	3.207	-0.001	-4.142	9.607	1.344	-3.156	24.654	4.484	5.498	0.786	0.046	0.018	0.150	0.059	-1.508	-0.334	1.170
13	1.063	0.221	0.716	3.210	-0.001	-4.141	9.606	1.344	-3.156	24.652	4.484	5.498	0.786	0.046	0.018	0.150	0.059	-1.508	-0.334	1.170

The design point has been verified using the FEM analysis. The final step of FORM analysis based on the response space results to a crest settlement of 0.98 m, the calculated crest settlement from FEM analysis is 0.95 m. A final FORM iteration using numerical analyses leads to similar influence factors (α_i^2), as shown in the table below.

No.	Sa [g] (=e ^{x1})	CRR [-] (=e ^{x2})	eSu/p' [-] (=e ^{x3})	m [-] (=e ^{x4})	Z [m]	$\partial Z/\partial x_1$	$\partial Z/\partial x_2$	$\partial Z/\partial x_3$	$\partial Z/\partial x_4$	α_{x1}^2	α_{x2}^2	α_{x3}^2	α_{x4}^2
final	1.060	0.220	0.720	3.210	-0.049	-3.852	9.630	1.605	-3.207	0.750	0.051	0.029	0.171

Table 18. Results of FORM-analyses for the Eemshaven profile using the median of local q_{c1Ncs} data [Sensitivity case 1 : Su/p' according to Kramer & Wang (2015); motion 6]

No.	Sa [g] (= e^{x1})	CRR [-] (= e^{x2})	$\epsilon Su/p'$ [-] (= e^{x3})	m [-] (= e^{x4})	Z [m]	$\partial Z/\partial x_1$	$\partial Z/\partial x_2$	$\partial Z/\partial x_3$	$\partial Z/\partial x_4$	μ_Z	σ_Z	Beta	α_{x1}^2	α_{x2}^2	α_{x3}^2	α_{x4}^2	x_{1d}	x_{2d}	x_{3d}	x_{4d}
0	0.634	0.104	0.663	2.071	0.054	-6.616	13.604	3.001	-3.098	39.162	7.418	5.279	0.780	0.135	0.033	0.053	-0.435	-2.267	-0.432	0.667
1	0.636	0.104	0.662	2.058	0.050	-6.623	13.620	3.002	-3.103	39.203	7.426	5.279	0.780	0.135	0.033	0.053	-0.436	-2.267	-0.432	0.667
2	0.637	0.104	0.660	2.047	0.046	-6.629	13.634	3.003	-3.107	39.240	7.433	5.279	0.780	0.135	0.033	0.053	-0.436	-2.267	-0.432	0.668
3	0.638	0.104	0.659	2.037	0.042	-6.634	13.647	3.004	-3.111	39.274	7.439	5.279	0.779	0.135	0.033	0.053	-0.436	-2.267	-0.432	0.668
4	0.639	0.104	0.658	2.028	0.038	-6.639	13.658	3.004	-3.115	39.304	7.445	5.280	0.779	0.135	0.033	0.053	-0.436	-2.267	-0.431	0.668
5	0.639	0.104	0.657	2.020	0.035	-6.643	13.668	3.006	-3.118	39.332	7.450	5.280	0.779	0.135	0.033	0.053	-0.436	-2.267	-0.431	0.668
6	0.640	0.104	0.657	2.013	0.032	-6.647	13.676	3.007	-3.121	39.357	7.454	5.280	0.779	0.135	0.033	0.053	-0.436	-2.267	-0.431	0.669
7	0.641	0.104	0.656	2.007	0.029	-6.651	13.684	3.008	-3.124	39.380	7.459	5.280	0.779	0.135	0.033	0.053	-0.436	-2.267	-0.431	0.669
8	0.641	0.104	0.655	2.001	0.027	-6.655	13.692	3.009	-3.127	39.402	7.463	5.280	0.779	0.135	0.033	0.053	-0.436	-2.267	-0.431	0.669
9	0.642	0.104	0.655	1.996	0.025	-6.658	13.698	3.010	-3.129	39.421	7.466	5.280	0.779	0.135	0.033	0.053	-0.436	-2.267	-0.431	0.669
10	0.642	0.104	0.654	1.992	0.023	-6.661	13.704	3.011	-3.131	39.439	7.470	5.280	0.779	0.135	0.033	0.053	-0.436	-2.267	-0.431	0.670
11	0.643	0.104	0.654	1.988	0.021	-6.663	13.710	3.011	-3.133	39.456	7.473	5.280	0.779	0.135	0.033	0.053	-0.436	-2.267	-0.431	0.670
12	0.643	0.104	0.653	1.985	0.019	-6.666	13.715	3.012	-3.135	39.471	7.476	5.280	0.779	0.135	0.033	0.053	-0.436	-2.267	-0.431	0.670
13	0.644	0.104	0.653	1.982	0.017	-6.668	13.720	3.013	-3.137	39.485	7.478	5.280	0.779	0.135	0.033	0.053	-0.436	-2.267	-0.431	0.670

The design point has been verified using the FEM analysis. The final step of FORM analysis based on the response space results to a crest settlement of 1.51 m, the calculated crest settlement from FEM analysis is 1.52 m.

Table 19. Results of FORM-analyses for the Delfzijl profile with spatial averaging [Sensitivity case 2 : S_u/p' according to Kramer and Wang (2015); ground motion 6]

No.	Sa [g] (=e ^{x1})	CRR [-] (=e ^{x2})	$\epsilon S_u/p'$ [-] (=e ^{x3})	m [-] (=e ^{x4})	Z [m]	$\partial Z/\partial x_1$	$\partial Z/\partial x_2$	$\partial Z/\partial x_3$	$\partial Z/\partial x_4$	μ_Z	σ_Z	Beta	α_{x1}^2	α_{x2}^2	α_{x3}^2	α_{x4}^2	x_{1d}	x_{2d}	x_{3d}	x_{4d}
0	1.000	0.214	0.536	1.904	-0.181	-8.018	22.520	4.885	-3.346	45.268	8.517	5.315	0.817	0.070	0.067	0.047	-0.008	-1.541	-0.617	0.632
1	0.999	0.214	0.537	1.900	-0.147	-7.942	22.322	4.836	-3.310	44.835	8.436	5.315	0.817	0.070	0.067	0.047	-0.009	-1.541	-0.617	0.631
2	0.997	0.214	0.537	1.895	-0.119	-7.880	22.157	4.797	-3.280	44.482	8.370	5.315	0.817	0.070	0.067	0.046	-0.009	-1.541	-0.617	0.630
3	0.996	0.214	0.538	1.892	-0.097	-7.830	22.021	4.766	-3.257	44.195	8.316	5.314	0.817	0.070	0.067	0.046	-0.009	-1.541	-0.617	0.630
4	0.995	0.214	0.538	1.889	-0.078	-7.789	21.909	4.741	-3.237	43.961	8.273	5.314	0.817	0.070	0.066	0.046	-0.009	-1.541	-0.617	0.629
5	0.994	0.214	0.538	1.886	-0.063	-7.756	21.817	4.720	-3.222	43.771	8.237	5.314	0.817	0.070	0.066	0.046	-0.009	-1.541	-0.617	0.629
6	0.994	0.214	0.539	1.884	-0.051	-7.729	21.741	4.704	-3.209	43.617	8.208	5.314	0.817	0.070	0.066	0.046	-0.009	-1.541	-0.617	0.628
7	0.993	0.214	0.539	1.882	-0.042	-7.707	21.680	4.690	-3.199	43.491	8.185	5.314	0.817	0.070	0.066	0.046	-0.009	-1.541	-0.617	0.628
8	0.993	0.214	0.539	1.881	-0.034	-7.689	21.630	4.679	-3.191	43.389	8.166	5.314	0.817	0.070	0.066	0.046	-0.009	-1.541	-0.617	0.628
9	0.993	0.214	0.539	1.879	-0.027	-7.674	21.590	4.670	-3.184	43.307	8.150	5.314	0.817	0.070	0.066	0.046	-0.009	-1.541	-0.617	0.628
10	0.992	0.214	0.539	1.878	-0.022	-7.663	21.557	4.663	-3.178	43.239	8.137	5.314	0.817	0.070	0.066	0.046	-0.009	-1.541	-0.617	0.628
11	0.992	0.214	0.539	1.877	-0.018	-7.653	21.530	4.657	-3.174	43.185	8.127	5.314	0.817	0.070	0.067	0.046	-0.009	-1.541	-0.617	0.628
12	0.992	0.214	0.539	1.876	-0.015	-7.645	21.508	4.653	-3.170	43.141	8.119	5.314	0.817	0.070	0.067	0.046	-0.009	-1.541	-0.617	0.628
13	0.992	0.214	0.540	1.876	-0.012	-7.639	21.490	4.649	-3.167	43.105	8.112	5.314	0.817	0.070	0.067	0.046	-0.009	-1.541	-0.617	0.628

The design point has been verified using the FEM analysis. The final step of FORM analysis based on the response space results to a crest settlement of 1.60 m, the calculated crest settlement from FEM analysis is 1.70 m.

Table 20. Results of FORM-analyses for the Eemshaven profile without spatial averaging [Sensitivity case 3 : S_u/p' according to Idriss and Boulanger 2008; ground motion 4]

No.	Sa [g] (=e ^{x1})	CRR [-] (=e ^{x2})	$\epsilon S_u/p'$ [-] (=e ^{x3})	m [-] (=e ^{x4})	Z [m]	$\partial Z/\partial x_1$	$\partial Z/\partial x_2$	$\partial Z/\partial x_3$	$\partial Z/\partial x_4$	μ_Z	σ_Z	Beta	α_{x1}^2	α_{x2}^2	α_{x3}^2	α_{x4}^2	x_{1d}	x_{2d}	x_{3d}	x_{4d}
0	0.500	0.100	0.900	2.000	-0.198	-7.376	9.128	7.361	-3.363	39.631	8.091	4.898	0.815	0.115	0.019	0.052	-0.673	-2.297	-0.100	0.616
1	0.502	0.100	0.901	1.969	-0.160	-7.267	9.024	7.284	-3.324	39.067	7.976	4.898	0.814	0.115	0.019	0.053	-0.676	-2.299	-0.101	0.617
2	0.503	0.100	0.902	1.946	-0.130	-7.182	8.936	7.222	-3.292	38.625	7.886	4.898	0.813	0.116	0.019	0.053	-0.678	-2.299	-0.101	0.618
3	0.504	0.100	0.902	1.927	-0.105	-7.116	8.863	7.172	-3.266	38.276	7.816	4.897	0.813	0.116	0.019	0.053	-0.680	-2.300	-0.101	0.619
4	0.505	0.100	0.902	1.913	-0.085	-7.064	8.803	7.131	-3.245	38.001	7.760	4.897	0.812	0.116	0.019	0.053	-0.681	-2.300	-0.101	0.619
5	0.505	0.100	0.903	1.902	-0.069	-7.023	8.755	7.098	-3.228	37.782	7.715	4.897	0.812	0.116	0.019	0.053	-0.681	-2.300	-0.101	0.620
6	0.505	0.100	0.903	1.893	-0.056	-6.991	8.716	7.071	-3.214	37.608	7.680	4.897	0.812	0.116	0.019	0.053	-0.681	-2.300	-0.101	0.620
7	0.505	0.100	0.903	1.886	-0.045	-6.965	8.685	7.049	-3.203	37.469	7.652	4.897	0.812	0.116	0.019	0.053	-0.682	-2.300	-0.101	0.620
8	0.505	0.100	0.903	1.881	-0.037	-6.944	8.660	7.031	-3.194	37.359	7.629	4.897	0.812	0.116	0.019	0.053	-0.682	-2.300	-0.102	0.620
9	0.505	0.100	0.903	1.876	-0.030	-6.928	8.639	7.016	-3.186	37.270	7.611	4.897	0.812	0.116	0.019	0.053	-0.682	-2.300	-0.102	0.620
10	0.506	0.100	0.903	1.873	-0.024	-6.914	8.623	7.004	-3.181	37.199	7.597	4.897	0.812	0.116	0.019	0.053	-0.682	-2.300	-0.102	0.620
11	0.506	0.100	0.903	1.870	-0.020	-6.904	8.610	6.994	-3.176	37.142	7.585	4.897	0.812	0.116	0.019	0.053	-0.682	-2.300	-0.102	0.620
12	0.506	0.100	0.903	1.868	-0.016	-6.895	8.599	6.986	-3.172	37.096	7.576	4.897	0.812	0.116	0.019	0.053	-0.682	-2.300	-0.102	0.620
13	0.506	0.100	0.903	1.866	-0.013	-6.888	8.591	6.980	-3.169	37.059	7.569	4.897	0.812	0.116	0.019	0.053	-0.682	-2.300	-0.102	0.620

The design point has been verified using the FEM analysis. The final step of FORM analysis based on the response space results to a crest settlement of 1.62 m, while the calculated crest settlement from FEM analysis is 1.60 m. A final FORM iteration using numerical analysis results concludes to similar influence factors (α_i^2) as shown in the table below.

No.	Sa [g] (=e ^{x1})	CRR [-] (=e ^{x2})	$\epsilon S_u/p'$ [-] (=e ^{x3})	m [-] (=e ^{x4})	Z [m]	$\partial Z/\partial x_1$	$\partial Z/\partial x_2$	$\partial Z/\partial x_3$	$\partial Z/\partial x_4$	α_{x1}^2	α_{x2}^2	α_{x3}^2	α_{x4}^2
final	0.506	0.100	0.900	1.870	0.008	-6.545	8.415	5.610	-3.147	0.806	0.122	0.014	0.058

Table 21. Results of FORM-analyses for the Delfzijl profile without spatial averaging [Sensitivity case 4 : S_u/p' according to Idriss and Boulanger 2008; ground motion 4]

No.	Sa [g] (=e ^{x1})	CRR [-] (=e ^{x2})	$\epsilon S_u/p'$ [-] (=e ^{x3})	m [-] (=e ^{x4})	Z [m]	$\partial Z/\partial x_1$	$\partial Z/\partial x_2$	$\partial Z/\partial x_3$	$\partial Z/\partial x_4$	μ_Z	σ_Z	Beta	α_{x1}^2	α_{x2}^2	α_{x3}^2	α_{x4}^2	x_{1d}	x_{2d}	x_{3d}	x_{4d}
0	0.800	0.190	0.900	2.300	-0.145	-5.843	8.997	5.367	-3.393	31.285	6.232	5.020	0.810	0.083	0.017	0.090	-0.282	-1.690	-0.097	0.827
1	0.791	0.189	0.901	2.297	-0.127	-5.847	8.933	5.447	-3.374	31.264	6.230	5.019	0.812	0.082	0.017	0.089	-0.279	-1.688	-0.099	0.822
2	0.784	0.188	0.902	2.293	-0.110	-5.842	8.881	5.497	-3.355	31.211	6.221	5.017	0.813	0.082	0.018	0.088	-0.277	-1.687	-0.100	0.819
3	0.778	0.188	0.903	2.288	-0.094	-5.833	8.837	5.528	-3.338	31.142	6.208	5.016	0.814	0.081	0.018	0.087	-0.276	-1.686	-0.101	0.816
4	0.774	0.187	0.903	2.282	-0.079	-5.822	8.801	5.546	-3.322	31.067	6.194	5.016	0.814	0.081	0.018	0.087	-0.275	-1.685	-0.101	0.814
5	0.771	0.187	0.903	2.277	-0.067	-5.810	8.771	5.557	-3.309	30.993	6.180	5.015	0.815	0.081	0.018	0.087	-0.275	-1.685	-0.101	0.812
6	0.769	0.186	0.903	2.272	-0.056	-5.798	8.746	5.562	-3.297	30.924	6.167	5.015	0.815	0.080	0.018	0.086	-0.274	-1.684	-0.102	0.811
7	0.767	0.186	0.903	2.268	-0.047	-5.787	8.725	5.565	-3.287	30.861	6.154	5.014	0.815	0.080	0.018	0.086	-0.274	-1.684	-0.102	0.810
8	0.766	0.186	0.903	2.264	-0.039	-5.777	8.708	5.565	-3.279	30.805	6.144	5.014	0.815	0.080	0.018	0.086	-0.274	-1.684	-0.102	0.809
9	0.765	0.186	0.903	2.261	-0.032	-5.769	8.694	5.565	-3.272	30.756	6.134	5.014	0.815	0.080	0.019	0.086	-0.274	-1.684	-0.102	0.809
10	0.764	0.186	0.903	2.258	-0.027	-5.761	8.683	5.564	-3.266	30.714	6.126	5.014	0.815	0.080	0.019	0.086	-0.274	-1.684	-0.102	0.809
11	0.763	0.186	0.903	2.255	-0.022	-5.755	8.674	5.562	-3.261	30.678	6.119	5.014	0.815	0.080	0.019	0.086	-0.275	-1.684	-0.103	0.808
12	0.762	0.186	0.903	2.253	-0.019	-5.749	8.666	5.561	-3.257	30.648	6.113	5.014	0.815	0.080	0.019	0.086	-0.275	-1.684	-0.103	0.808
13	0.762	0.186	0.903	2.251	-0.015	-5.744	8.660	5.560	-3.253	30.622	6.108	5.013	0.815	0.080	0.019	0.086	-0.275	-1.684	-0.103	0.808

The design point has been verified using the FEM analysis. The final step of FORM analysis based on the response space results to a crest settlement of 1.34 m, while the calculated crest settlement from FEM analysis is 1.30 m. A final FORM iteration using numerical analysis results concludes to similar influence factors (α_i^2) as shown in the table below.

No.	Sa [g] (=e ^{x1})	CRR [-] (=e ^{x2})	$\epsilon S_u/p'$ [-] (=e ^{x3})	m [-] (=e ^{x4})	Z [m]	$\partial Z/\partial x_1$	$\partial Z/\partial x_2$	$\partial Z/\partial x_3$	$\partial Z/\partial x_4$	α_{x1}^2	α_{x2}^2	α_{x3}^2	α_{x4}^2
final	0.762	0.186	0.903	2.250	0.075	-5.625	7.875	5.625	-3.076	0.828	0.070	0.020	0.081

Appendix J Sensitivity analyses on design sea water level

In Fugro (2016c) dynamic levee stability evaluations the water table level for earthquake loading (i.e. corresponding to a 1-year flood event) was used in the analyses together with the application of earthquake loading. The water level corresponding to the 1-year flood event is at El. +3.75m NAP at seaside for both Eemshaven and Delfzijl.

Since water pressure acts as a stabilizing force on the seaside levee slope, the use of the higher water levels associated with the 1-year flood event may be an unconservative assumption in terms of levee crest settlements. To address this issue, additional numerical analyses were performed assuming mean high water level (i.e. El. +1.93m NAP for both Eemshaven Delfzijl) and mean low tides water level (i.e. El. -0.7m NAP for Eemshaven and El. -1.85m NAP for Delfzijl) to evaluate its influence on dynamically induced crest settlements. The water levels are shown schematically on Figure 43.

Results of the sensitivity analyses on the water level are shown on Figure 44 for Eemshaven and Figure 45 for Delfzijl. The figures plot contours of post seismic crest settlement for the 1-year flood event (upper illustration), mean high water level (illustration in the middle) and mean low tides water level (lower illustration). As shown on these figures the crest settlements are not significantly affected for the water levels considered.

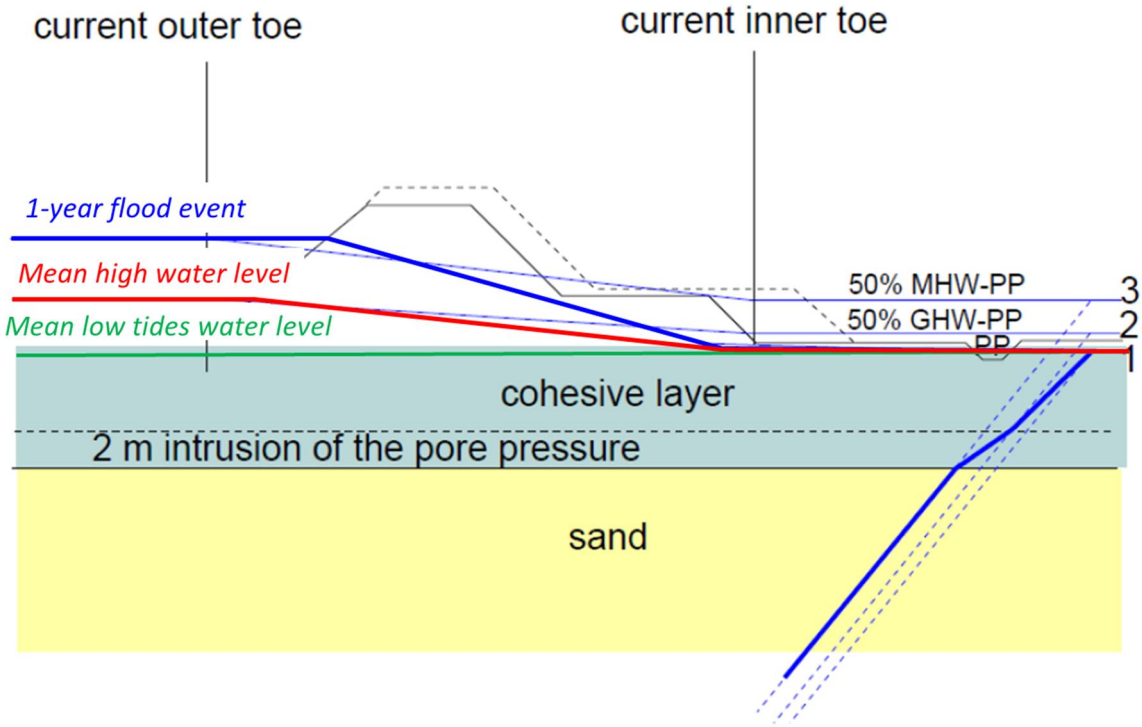


Figure 43. Schematization of 1-year flood event (blue line), mean high (red line) and mean low tides (green line) water levels.

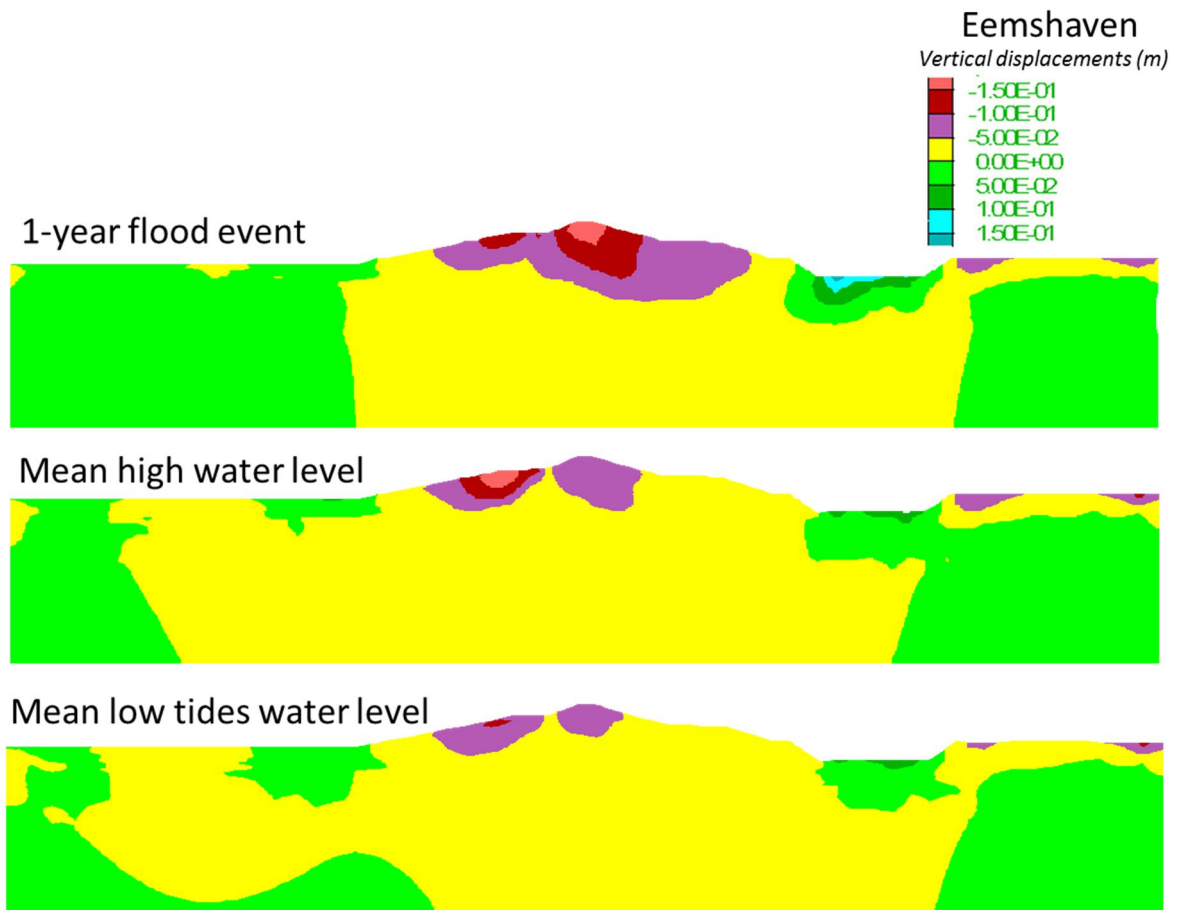


Figure 44. Contours of residual vertical displacements in Eemshaven for 1-year flood event (blue line in Figure 43), mean high (red line in Figure 43) and mean low tides (green line in Figure 43) water level conditions.

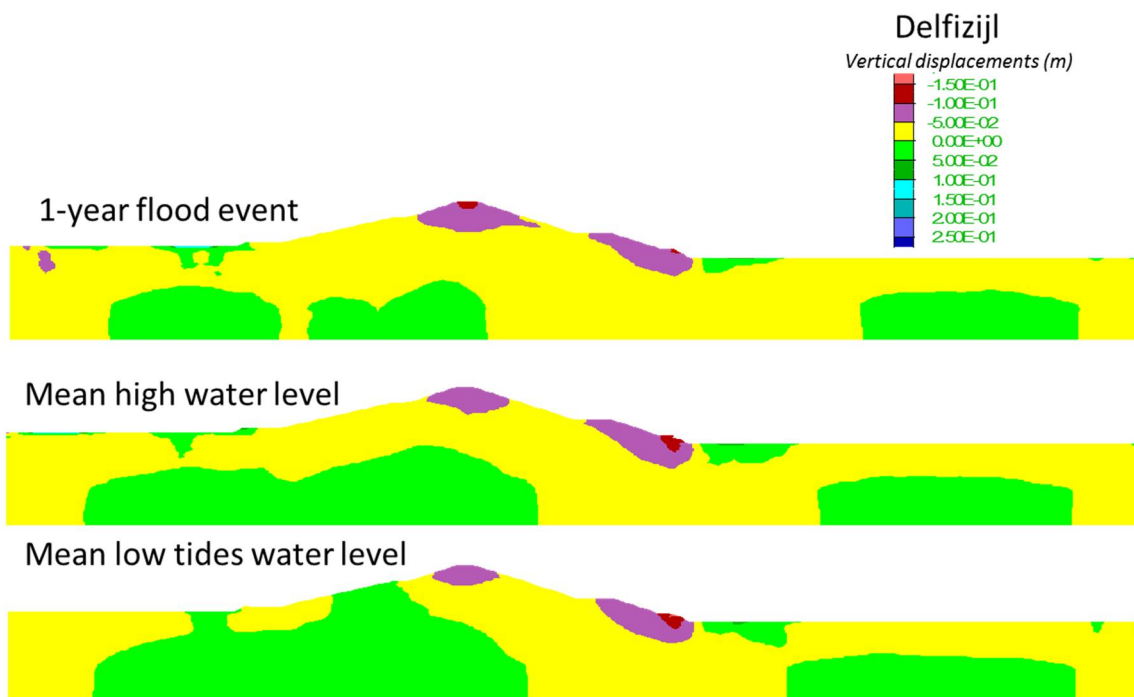


Figure 45. Contours of residual vertical displacements in Delfzijl for 1-year flood event (blue line in Figure 43), mean high (red line in Figure 43) and mean low tides (green line in Figure 43) water level conditions.